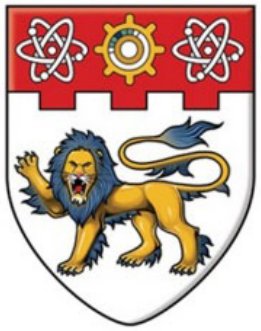

NANYANG TECHNOLOGICAL UNIVERSITY

# MOLECULAR AND NANO-STRUCTURED CATALYST DESIGN TOWARD DYE SENSITIZED SOLAR FUEL PRODUCTION

**HAN JIANYU**

**SCHOOL OF CHEMICAL AND BIOMEDICAL ENGINEERING**

**2015**

# MOLECULAR AND NANO-STRUCTURED CATALYST DESIGN TOWARD DYE SENSITIZED SOLAR FUEL PRODUCTION

**HAN JIANYU**

School of Chemical and Biomedical Engineering

A thesis submitted to the Nanyang Technological University In partial fulfilment of the requirement for the degree of Doctor of Philosophy

**2015**

# ACKNOELEDEGEMENTS

Firstly, I would like to express my sincere gratitude to my supervisor Prof. Xu Rong for the continuous supporting of my Ph.D. study and related research. Her academic rigor and dedicated attitude have great effect on me and continue inspiring me to try my best on my research. I sincerely appreciate her guidance, encouragement, generosity and patience.

Besides my supervisor, I also would like to thank my lab mates, Dr. Zhou Tianhua, Dr. Zhang Wei, Dr. Wang Yabo, Dr. Hong Jindui, Dr. Wang Danping, Dr. Chen Chunping, Dr. Amin Yoosefi Booshehri, Dr. Pan Yunxiang, Dr. Zou Yinjun, Dr. Xu you, Mr. Goh Chun Kiat Simon and Mr. Yin Shenming. They manufactured a harmonious academic environment and did me a lot favor in the research work. I was enjoying working with all of them.

Also, my thanks go to the technical staffs and professional officers in our school and in the project of SinBeRise. Thank their assistance on chemical purchase and instrument training and using.

Last but not the least, I would like to thank my family. My grandmother, my father and my mother devote all their love to me and provide me a comfort and warm environment. Finally, special thanks go to my wife Wu Yafeng and my lovely daughter Han Yunxi for enlightening my life. Thank you for your accompanying.

# TABLE OF CONTENT

## LIST OF FIGURES

## LIST OF TABLES

## LIST OF SCHEMES

## LIST OF ABBREVIATIONS

| | |
|---|---|
| BET | Brunauer-Emmett-Teller |
| BJH | Barrett-Joyner-Halenda |
| BPY | 2,2'-bipyridine |
| CB | conduction band |
| CV | cyclic voltammetry |
| DMF | dimethylformamide |
| EA | elemental analysis |
| EIS | electrochemical impedance spectroscopy |
| EY | Erythrosin yellowish |
| FL | fluorescein |
| FTIR | Fourier transform infrared spectroscopy |
| GC | gas chromatography |
| ICP | inductively coupled plasma |
| LSV | linear sweep voltammetry |
| MCNT | multi-walled carbon nanotube |
| ME | mercaptoethanol |
| MLCT | metal to ligand charge transfer |
| MOF | metal-organic framework |
| NHE | normal hydrogen electrode |
| NMR | nuclear magnetic resonance |
| PCET | proton coupled electron transfer |
| POM | polyoxometalates |
| QE | quantum efficiency |
| RDE | rotating disk electrode |
| SCE | saturated calomel electrode |
| TEOA | triethanolamine |
| TGA | thermal gravimetric analysis |
| TOF | turnover frequency |

| | |
|---|---|
| TON | turnover number |
| UV-vis | ultraviolet-visible spectroscopy |
| VB | valence band |
| XANES | X-ray absorption near edge structure |
| XPS | X-ray photoelectron spectroscopy |
| XRD | X-ray diffraction |

# ABSTRACT

Harnessing the solar light and subsequent storage the solar energy in the form solar fuel hold the promise to address the future energy supply. Photocatalytic water splitting and photocatalytic carbon dioxide reduction are the most attractive but challenging technologies for solar to fuel conversion. The main difficulty of these two reactions lies in the lack of low cost, stable and efficient catalysts. In this thesis, the research work is dedicated to the design and development of efficient catalysts that can withstand the cruel reduction and oxidation conditions in photocatalytic water splitting systems.

Firstly, inspired by nature, two complexes formed between Ni(II) and β-mecaptoethylamine with a mixed S and N donor environment are investigated. A metal free dye, Erythrosin yellowish was used as photosensitize for light harvesting. Both complexes are found to be active and inexpensive catalysts for photocatalytic hydrogen evolution by water reduction. An excellent quantum efficiency of 30.9% was obtained at 480 nm. A reaction mechanism involving intramolecular proton transfer from N atom to Ni centre was proposed. This work provides us with useful clues to further explore noble-metal free complexes with a relevant environment to natural enzymes toward development of earth-abundant photocatalyst systems for solar hydrogen production.

Secondly, cobalt oxide nanoparticles have been successfully embedded into the zeotypic giant cavities of MIL-101, a well-known metal organic framework (MOF) with excellent stability, by a facile impregnation and heat treatment method. The incorporated nanoparticles of 2-3 nm display an excellent dispersion and narrow size distribution. The apertures of the MOF, which is smaller than the size of cobalt oxide nanoparticles, prevent the nanoparticles from aggregation and leaching. A $Ru(bpy)_3^{2+}$-$Na_2S_2O_8$ system was evolved to conduct the photocatalytic water oxidation reaction in borate buffer using above material. This hybrid material induces great enhancement in photocatalytic water oxidation activity of cobalt oxide with a high turnover frequency (TOF) of 0.012 $s^{-1}$ per cobalt atom, which is more than 9 fold

compared with that of the unsupported $Co_3O_4$ nanoparticles. Moreover, MIL-101 plays the role of promoting the charge transfer as evidenced by the Nyquist plots. This study suggests that MIL-101 as a chemically stable MOF is a promising support for encapsulation of catalyst nanoparticles for photocatalytic applications.

Finally, a cobalt based polyoxometalate (POM) catalyst, CoPOM, was successfully immobilized in the cavities of MIL-101 by an impregnation method. The CoPOM anions are bounded to MIL-101 tightly by electronic static interaction with excellent dispersion. This host-guest material system constructed with earth abundant elements only show high performances for photocatalytic water oxidation when sanitized by $Ru(bpy)_3^{2+}$. The combination also shows enhanced activity and stability compared with the free CoPOM. In addition, it is likely that the cavities of MIL-101 play an important role in protecting the active CoPOM anions from decomposition. Moreover, the highly porous structure offers an environment for the stacking of homogeneous catalytic anions per MOF particulate to achieve higher TOF. The immobilized catalysts can be recovered from the reaction solution, which is significant for potential practical application.

In summary, this thesis work is focused on the development of economical, stable and efficient catalysts for both photocatalytic water reduction and oxidation sensitized by organic dyes. Biomimetic complexes with various coordination environments have been investigated as the catalysts for photocatalytic water reduction, which provide insight into designing of more efficient water reduction catalysts. This is followed by two systems evolving MIL-101 as the substrate to immobilize both homogeneous and heterogeneous catalysts for water oxidation. It was found the incorporation of catalysts in the cavities of MIL-101 not only can enhance their activities for water oxidation but also can improve their stabilities.

# CHAPTER 1 INTRODUCTION

## 1.1 Background and motivations

Nowadays the reserve fossil fuels including petroleum, coal and natural gas are being exhausted at an accelerated rate. The world's reliance on fossil fuels causes not only environmental problems but also geopolitical issues[1]. As a result, searching for substituting clean and renewable energy sources is an urgent task in order to relieve the energy and environmental crisis. Among all the renewable energy resources we know to date, solar energy represents the most promising one. The amount of solar radiation intercepted by Earth is more than sufficient to meet current and projected energy uses well beyond 2100[2]. Solar energy can be harnessed as thermal energy for heating[3] or be converted to electricity by photovoltaics[4,5]. In addition, solar energy can also be transformed to chemical energy and stored in the form of chemical bonds in certain compounds. These compounds obtained by artificial photosynthesis are called solar fuels[6]. In natural photosynthesis, plants absorb the solar energy to oxidize water to generate oxygen. The resultant electrons are at sufficiently negative redox potential to reduce carbon dioxide for hydrocarbons production[7]. Inspired by nature, researchers intend to develop artificial photosynthesis following the biological blueprint. Typically, two artificial photosynthetic reactions are evolved for solar fuel production: (1) the overall water splitting reaction (2) the carbon dioxide reduction reactions. The solar fuels generated from above reactions are hydrogen and hydrocarbons.

In early 1970, the concept of "Hydrogen Economy" was proposed by the University of Michigan[8]. Hydrogen fuel is believed to be the ultimate replacement for fossil hydrocarbons. Hydrogen is attractive because the product of its combustion or oxidation is only water when it is burned to produce heat or reacted with oxgyen in fuel cell to produce electricity. Moreover, hydrogen possesses high energy density by weight. Each mole of $H_2$ can store 273 kJ of energy in the form of chemical bond as

shown in Equation 1. However, currently hydrogen is mainly produced from sources of fossil origin, which deviates from the renewable goal. A breakthrough in photocatalytic water splitting reaction was reported by Honda and Fujishima in 1972 using $TiO_2$ as the photocatalyst, which prompted the scientific community that it was possible to produce hydrogen in a sustainable and clean way by using solar energy[9]. Since then, intensive efforts have been made to study basic principles of photocatalysis and design efficient photocatalysts. Expectedly, it is promising to step into the "Hydrogen Economy" in 21st century if the quantum efficiency for water splitting can be enhanced to be higher than 10% for practical applications.

$$H_2O \longrightarrow H_2 + \frac{1}{2}O_2 \; ; \quad \Delta G = +237 \text{ kJ/mol} \qquad (1)$$

In contrast, in natural photosynthesis, plants facilitate light-driven carbohydrate formation by oxidizing water to provide electrons and protons needed for $CO_2$ reduction[7]. The water oxidation reaction is essential for solar to fuel conversion since water is the only inexpensive and rich source to provide protons and electrons in a tetra scale[10]. However, water oxidation is challenging since it requires to overcome the high activation energy (Equitation 2) for removal of four electrons coupled with four protons to form one oxygen molecule. As a consequence, development of efficient water oxidation catalyst (WOC) is urgent for solar fuel production.

$$2H_2O \longrightarrow O_2 + 4H^+ + 4e^- \; ; \quad \Delta G = +475 \text{ kJ/mol} \qquad (2)$$

## 1.2 Objectives and scope

Since the pioneering finding by Fujishima and Honda, both the water reduction half-reaction and water oxidation half-reaction have been extensively studied. In spite of the paid efforts, most of the obtained results to date are still far away form practical applications. Noble metals are commonly employed as active sites to react with water to produce hydrogen or oxygen. Some noble metal free catalysts showed low activity or poor durability. It is still challenging to achieve low cost, stable, visible light harvesting and efficient catalysts for both water reduction and water oxidation. The objectives and scope of this thesis are summarized as following to meet such

challenges:

(1) To develop an efficient bio-mimetic water reduction catalyst with earth abundant elements. In nature, hydrogenases constructed from Fe and Ni with a variety of coordination types are efficient catalysts for proton reduction, which inspired us to develop bio-mimetic Ni complexes with a variety coordinative environment for photo catalytic water reduction. This work is presented in Chapter 3.

(2) To immobilize water oxidation catalyst on the substrate for enhanced photocatalytic activity. Immobilization of metal oxides such as $Co_3O_4$ in cavities of proper substrates (like metal-organic frameworks) can reduce their size thus generating more active sites to improve their activity for photocatalytic water oxidation. This work is presented in Chapter 4.

(3) To deposit homogeneous molecular catalyst on the substrate for enhanced stability and activity. The stability of homogeneous molecular catalyst is a main concern for their large scale application. They are not easily recoverable after the reaction from the homogeneous solution. The MIL-101, a robust MOF, was employed to encapsulate the macular catalyst to stabilize and recover the catalyst. This work is presented in Chapter 5.

In summary, this thesis work is focused on developing of transition metal based, stable and efficient catalysts for both photocatalytic water reduction and water oxidation.

## 1.3 Major contributions of the thesis

Contributions of this thesis to the field of photocatalysis for solar fuel generation are summarized as following:

(1) The biomimetic complexes constructed from earth abundant elements are active and inexpensive catalysts for $H_2$ generation by water reduction. Excellent quantum efficiency was obtained for the complexes with the N and S mixed donor. It provides useful clues for development of noble-metal free complexes with various coordinative environment that mimics natural enzymes toward solar fuel production.

(2) Cobalt oxide nanoparticles of 2-3 nm can be successfully embedded into the cavities of MIL-101 with excellent dispersion and narrow size distribution by a facile impregnation and calcination method. The incorporated cobalt oxides are highly active for water oxidation and stable. The MIL-101 facilitates charge transfer in the photocatalytic process. This method can be extended to develop other metal oxides and metal sulfides immobilized MOFs for a wider range of applications.

(3) A highly efficient homogeneous molecular water oxidation catalyst $[Co(H_2O)_2(PW_9O_{34})_2]^{10-}$ (CoPOM) was immobilized on MIL-101 by electrostatic interaction. The coordination between MIL-101 and CoPOM can not only stabilize CoPOM but also enhance its activity for water oxidation. Moreover, the heterogenization of molecular CoPOM makes it easily recycled from the solution after reaction.

# CHAPTER 2 LITERATURE REVIEW

## 2.1 Fundamental principles of photocatalytic water splitting

There are three main processes during the photocatalytic reactions as shown in Figure 2-1. Initially the photosensitizers absorb photons to generate electron/hole pairs. The band structure of semiconductors is composed of valence band (VB) and conduction band (CB). The energy difference between the minimum of CB and maximum of VB is called band gap. When the energy of the incident light is higher than band gap, electrons located in the VB will be excited to CB, leaving positively charged holes in the VB. Secondly, the photo-generated electrons and holes will migrate to the surface of the catalyst. Finally, water reduction and/or water oxidation happens by reacting with these charge carriers.

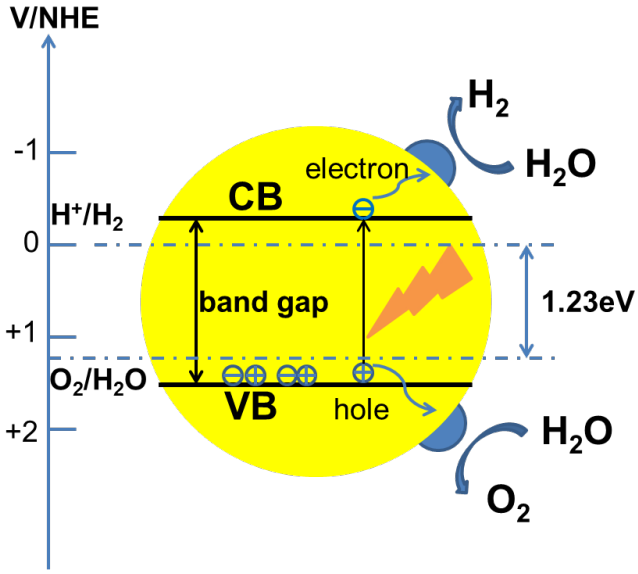


**Figure 2-1** Fundamental principles of water splitting using semiconductor photocatalysts.

Several points should be noted during the whole process. Firstly, the band structure of semiconductors should match well with the redox potentials of water, which means the CB should be more negative than the redox potential of $H^+/H_2$ (0 V vs. NHE), while the VB has to be more positive than the redox potential of $O_2/H_2O$ (1.23 V vs. NHE). As an uphill reaction, the water splitting reaction has Gibbs free energy change

of 1.23 eV. Therefore, the band gap should be greater than 1.23 eV, while less than 3.0 eV to achieve visible light absorption. Secondly, the recombination of electrons and holes often takes place during the charge migration process. Crystalline defects, which act as charge recombination centers will enhance this recombination. Long migrating paths will cause enhanced recombination because of rising transmitting time. Thus decreasing the defects by calcination and shrinking the size of the catalysts are effective approaches to enhance the activity. Thirdly, surface properties such as active sites and surface areas play important roles in the water redox step. Cocatalysts loaded on the surface will often promote the charge separation hence lowering surface recombination.

## 2.2 Water reduction

Though several breakthroughs have been achieved in the recent decades, realization of photocatalytic overall water splitting is still a tough task. Since water splitting consists of water reduction and water oxidation, while water oxidation reaction involving a complicated four-electron transferring process. This half reaction requires accumulation of charge coupled with removal of four protons to form one oxygen molecule, which is considered as the obstacle to achieve photocatalytic overall water splitting[11]. But this obstacle does not hinder us from studying each half reaction separately. Investigating half reactions employing sacrificial reagents is meaningful to evaluate catalytic performances including thermodynamic and kinetic aspects. Furthermore, adding sacrificial reagents could be significant for practical hydrogen production if low cost reducing reagents are developed[12-15]. When the reactions are carried out in aqueous solutions with electron donors, such as metal sulfides and triethanolamine (TEOA), photo-generated holes are scavenged by these donors instead by water, which enrich electron levels in CB and enhance hydrogen production. On the other hand, oxygen evolution from water splitting will be promoted by adding electron scavengers.

Generally, photocatalytic reactions according to the type of photosensitizers can be classified into semiconductor based systems and dye sensitized systems.

### 2.2.1 Semiconductor based systems for water reduction

Conventional metal oxides semiconductors are constructed of $d^0$ metal[16-23] ($Ti^{4+}$, $Zr^{4+}$, $Nb^{5+}$, $Ta^{5+}$, $W^{6+}$, $Mo^{6+}$), $d^{10}$ metal[24-28] ($In^{3+}$, $Ga^{3+}$, $Ge^{4+}$, $Sn^{4+}$, $Sb^{5+}$), and $f^0$ metal[29] ($Ce^{4+}$)[29]. Among all the metal oxides, $TiO_2$ is the most well known semiconductor. However, just like many other metals oxides constructed by $d^0$ or $d^{10}$ metal ions, $TiO_2$ can only absorb UV light due to its wide band gap. Because valence bands of these photocatalysts are composed of O 2p orbitals, of which the potential is about 3.0 eV vs. NHE, while their conduction bands consisting of d orbitals of metals are more negative than 0 eV vs. NHE. To fully utilize the solar light, it is necessary to modify these materials for visible light harvesting. Based on the research results in the past decades, several common approaches have been concluded: (1) band gap engineering by ions doping, (2) developing solid solution to control band structure, (3) creating novel single phase visible light responsive catalysts.

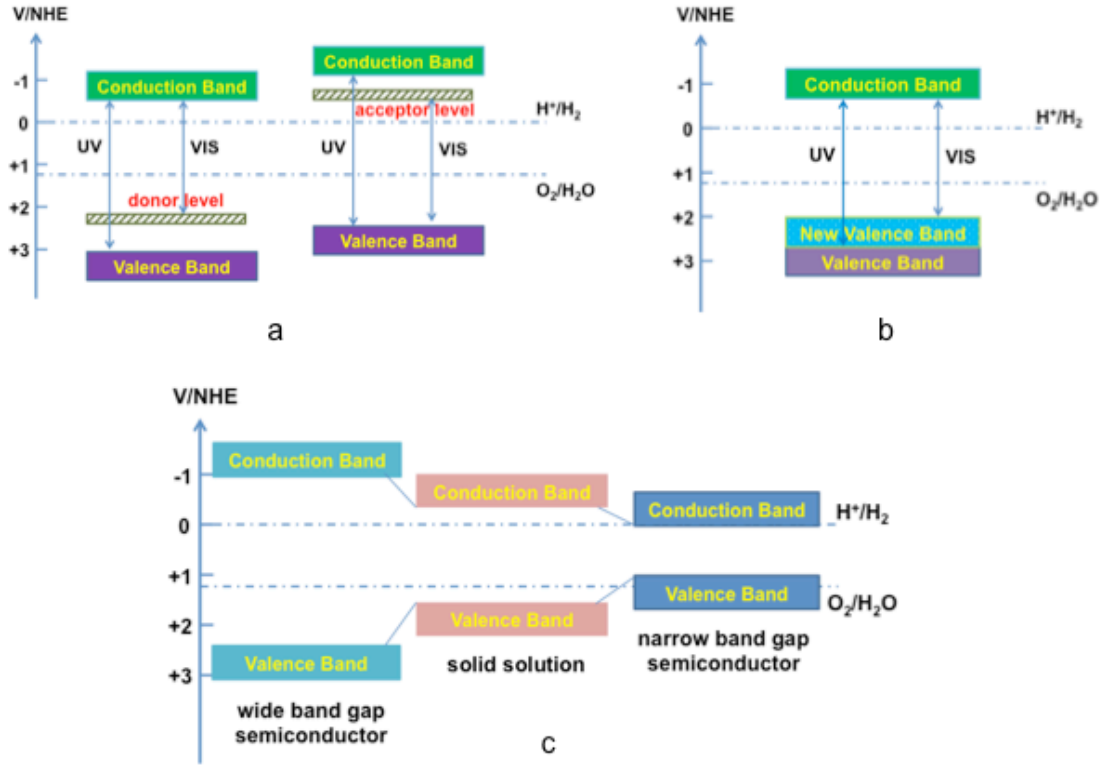


**Figure 2-2** (a) Donor level and acceptor level formed by ions doping, (b) Formation of new valence band by nonmetal doping, (c) Band gap engineering by formation of solid state solution.

Doping transition metal into crystal sites of metal oxides is one of the most effective methods to develop visible responsive photocatalysts by creating impurity levels in the forbidden band as shown in Figure 2-2a. Since Borgarello et al. found that $Cr^{5+}$ doped $TiO_2$ could produce hydrogen under visible light in 1982[30,31], many transitions metals including Ni, V, Cr, Mo, Fe, Sn , Mn have been successfully doped into $TiO_2$ for visible light harvesting[31-36]. Unlike metal ion doping, nonmetal ion doping narrows the band gap by shifting the valence band upward instead of forming impurity levels in the forbidden band as shown in Figure 2-2b. Nonmetal ions such as S and N have 3p and 2p orbitals respectively, which have more negative potentials than 2p orbitals of O. Therefore, N and S are often doped into metal oxides to narrow the band gap by shifting the valence band upward. Many methods including sputtering and implantation techniques[37], high temperature sintering under nitrogen containing atmosphere[38], sol–gel processes[39] and hydrothermal treatment[40], spray pyrolysis[41] and supercritical methods[42] have been employed to dope N and S at $TiO_2$. Solid solution is another method to align the band gap as shown in Figure 2-2c. These solid solutions are usually formed by a wide band gap and a narrow band gap semiconductor. Band structures including the band gap and the band positions can be adjusted by varying the ratio of both components. Metal oxides with similar crystal structures can form solid solution through solid state reactions[43].

Valence band of metal sulfides consisting of S 3p orbitals is more negative than that of metal oxides. Thus metals sulfides are promising candidates for visible light driven photocatalysis. The main drawback is photocorrosion. CdS with a band gap of 2.4 eV achieved impressive efficiency and quantum yield for hydrogen production under visible light when loaded with cocatalysts such as NiS and Pt[44-47]. Metal sulfides with similar crystals structure can also form solid state solution to enhance the activity. Solid solutions formed by ZnS and other sulfides involving CdS, $AgInS_2$ and $CuInS_2$ displayed excellent performances for hydrogen production[48-52].

Metal (oxy)nitrides developed by Domen's group possesses light absorption up to 500-600 nm. Oxynitrides constructed by $Ti^{4+}$, $Nb^{5+}$, $Ta^{5+}$ with $d^0$ configuration can

evolve $H_2$ or $O_2$ in sacrificial reagents respectively[53-55]. It is still hard for these materials to split water into $H_2$ and $O_2$ separately if no sacrificial reagent is present. However, this obstacle can be overcome by forming solid-state solutions. Since 2005, Domen and his coworkers have systematically studied the GaN-ZnO solid-state solutions[56-61]. Both of GaN and ZnO have a band gap larger than 3.0 eV. However, when they form the solid state solutions denoted as GaN:ZnO, the p-d repulsion between N 2p and Zn 3d orbitals shift the valence band upward without changing the conduction band[62]. As a result, the band position is suitable to split water into hydrogen and oxygen under visible light without any sacrificial reagent. When loaded with $Rh_{2-x}Cr_xO_3$ as the cocatalysts, the quantum efficiency of this solid solution can reach ~2.5% at 420-440nm[57]. And it is also reported that the GaN:ZnO is photo stable. It can maintain its 50% activity even after half a year[63]. Besides this GaN:ZnO solid solution, Domen and his coworkers develop another solid solution denoted as $(Zn_{1+x}Ge)(N_2O_x)$[64,65], which is also favorable for overall water splitting under visible light. Carbon nitride is another metal free nitrides that can function as water reduction catalyst under visible light.

### 2.2.2 Dye sensitized systems for water reduction.

Dye sensitized systems are also effective to achieve visible light harvesting. Many types of metal complex dyes and metal free dyes have been demonstrated to be powerful for visible light driven water splitting. The dye sensitized systems depending on the catalysts used can be classified into dye sensitized semiconductor systems and dye sensitized metal complex systems. The basic principles of dye sensitized semiconductor based photocatalytic hydrogen evolution are shown in Figure 2-3. However, the mechanism of dye sensitized complexes-based water splitting by photocatalysis is much more complicated.

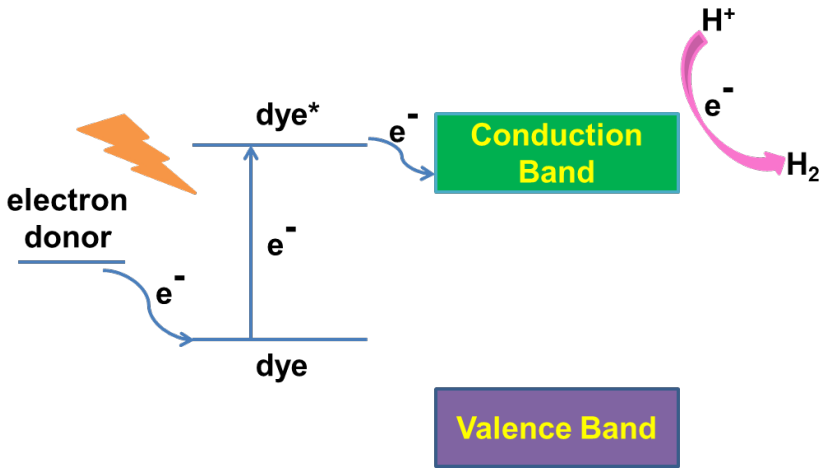


**Figure 2-3** Based principles of $H_2$ evolution using dye sensitized semiconductors.

In study of dye sensitized metal complexes for water reduction reactions, the main choices for light absorber are noble metal complexes with a charge transfer excited state. These complexes are constructed of noble metals including variants of Ru(II) tris(bipyridine) ($Ru(bpy)_3^{2+}$)[66,67] and bis(terpyridine) ($Ru(terpy)_2^{2+}$)[68] complexes, Ir(III) phenylpyridine ($Ir(ppy)_3^{3+}$)[69] complexes and Pt(II) bipyridine or terpyridine acetylide complexes[70,71]. A triplet-excited state exists by metal to ligand charge transfer (MLCT) for all above complexes when excited by visible light. The long lifetime of this triplet state facilitates these excited complexes to have sufficient time to transfer the charges to the catalyst. Despite the intensive and valuable studies, drawbacks of these photosensitizers are instability for long time irradiation and the use of noble metal, which render them not to be suitable for practical applications. Therefore, metal-free dyes are explored for visible light harvesting. In 1985, Shimidzu's group reported detailed studies on xanthene dyes working as sensitizers[72]. This series of heavy halogenated dyes including Rose Bengal, Erythrosine, Eosine and so on as shown in Scheme 2-1 displayed high efficiency for visible light harvesting. However, they undergo dehalogenation under long irradiation. The half dehalogenated Rhodamine B and the totally dehalogenated Fluorescein showed quite good stability but low activity. The indispensable heavy halogenated attribute to intersystem crossing for existence, which is absolute necessary for the long-lived triplet excited state. Both the noble

metal complexes and metal free organic dyes are investigated as photosensitizers for photocatalytic water reduction reaction.

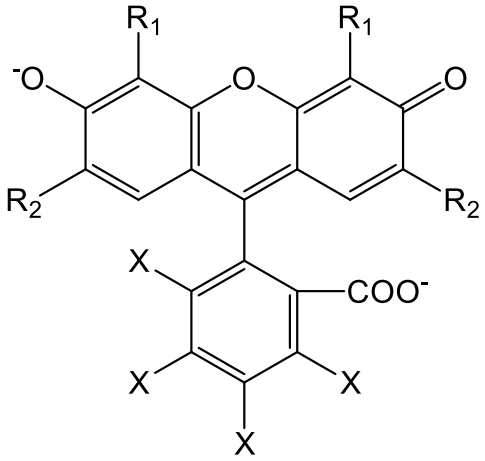


Eosin Y: $R_1$=$R_2$=Br, X=H
Eosin B: $R_1$=Br, $R_2$=$NO_2$, X=H
Erythrosin Y: $R_1$=H, $R_2$=I, X=H
Erythrosin B: $R_1$=$R_2$=I, X=H
Rose Bengal: $R_1$=H, $R_2$=I, X=Cl
Fluorescein: $R_1$=$R_2$=H, X=H

**Scheme 2-1** Chemical structure illustration of xanthene dyes.

In early 1981, Krishnan and Sutin found the first $Ru(bpy)_3^{2+}$ sensitized metal complex system for water reduction using cobalt bipyridine complexes as the catalysts[73]. Before that, numerous cobalt complexes have been widely applied for electocatalytic water reduction[74]. It is curious that if the driving force could be substituted by solar light. Eisenberg and Fisher reported two cobalt macrocyclic complexes for electocatalytic water reduction and carbon dioxide reduction in 1980[74]. Then these two complexes were demonstrated to be effective for photocatalytic water and carbon dioxide reduction simultaneously under visible light when $Ru(bpy)_3^{2+}$ was used as the photosensitizer[75]. Cobaloxime-based complexes are another series catalysts for hydrogen production when sensitized by $Ru(bpy)_3^{2+}$. The first example was reported by Lehn et al in 1983[76]. However, the instability and air sensitivity limit their application. Then a more stable $BF^{2-}$ annulated cobaloxime was reported by Espenson in 1986[77]. Sun and his coworkers then investigated $BF_2$-annulated tis(dimethylglyoximate) for water reduction sensitized by Eosine Y and Rose bengal[78]. Recently, Eisenberg's group reported H-bridged Co(III)- bis(dimethylglyoximate) complexes bearing a axial pyridine ligand. These catalysts showed outstanding performances for hydrogen production in $CH_3CN$ and water mixed solution no matter sensitized by platinum chromophore or Eosine Y[79].

Apart from cobalt, nickel and iron are also promising earth abundant elements for constructing water reduction catalysts. It is known that hydrogenases for proton reduction are constructed by nickel and iron[80]. Inspired by this, many biomimetic nickel and iron-based complexes have been explored for hydrogen evolution[81-83]. DuBois and coworkers systematically studied the $[Ni(P_2^{Ar}N_2^{Ar})_2](BF_4)_2$ for electrocatalytic hydrogen production, which contained two non-coordinating active sites of each ligand[84-86]. The same catalysts then were used for photocatalytic hydrogen production by McLaughlin and coworkers sensitized by $Ru(bpy)_3^{2+}$ and Eosine Y[87]. Hydrogenase-liked iron complexes were reported by Sun et al., which was active for hydrogen production when using $Ru(bpy)_3^{2+}$ as the sensitizer and ascorbic acid as the sacrificial reagent[88]. Beller' group reported that the $[Ir(bpy)(ppy)_2]PF_6$ sensitized iron carbonyl complexes were also effective catalysts for hydrogen production[89]. Recently a long-lived nickel thiolate complexes reported by Eisenberg obtained TONs as high as 5500 after 40 hours when fluorescein was used as photosensitizer[90]. Our group also reported a self-assembled nickel thiolate complex, which displayed impressive activity for hydrogen production. And an quantum efficiency (QE) of 24.5% was achieved at 460 nm when sensitized by Erythrosin B[91]. These biomimetic metal complexes are made of nontoxic, low cost and earth abundant elements. They are expected to represent the economical and environmentally benign systems.

In spite of the above achievements, there are limited reports on metal complexes with mixed donor for dye sensitized water reduction. Moreover, the currently obtained QE is still far away practical applications. In addition, the mechanism of the dye sensitized metal complexes for water reduction is also not clear yet. Development of more complexes with various types of donor environment will help study the effect coordinated ligand thus providing us clues for designing of more efficient water reduction catalysts.

### 2.2.3 Summary

From the above literature review, it can be concluded that it is quite a difficult task to align the band positions for visible light absorption while retaining sufficient driving force for water reduction. The advantage of dye-sensitized systems lies in the separation of light absorber and catalyst just as that done in nature, which makes it much easier to amend both components to achieve high efficiency. The inspiration from nature prompts us to develop biomimetic complexes for catalytic water reduction.

## 2.3 Water oxidation

As mentioned above, the water oxidation reaction is considered to be the bottleneck for solar fuel production since it requires the transferring of four electrons to form one O-O bond. This calls for water oxidation catalysts (WOCs) capable of overcoming thermodynamic potential of water oxidation to accumulate four oxidizing equivalents. And it should also avoid the formation of high-energy intermediates that can damage the WOCs. Thus, the proton coupled electron transfer (PCET) is essential to neutralize the charge when the mulitelectron-transfer catalysis occurred[92,93]. The PCET allow for removal one electron coupled with a proton preventing the accumulation of charge to form high-energy intermediates. Therefore, a successful WOC should be stable to oxidize, hydrolytic and thermal degradation, efficient to catalyze water oxidation with high turnover frequency, and amendable to adapt different conditions[94]. Numbers of heterogeneous and homogeneous WOCs have been investigated for the purpose to meet these challenges.

### 2.3.1 Heterogeneous WOCs

Transition metal oxides have been intensively investigated as WOCs. They are stable enough to withstand the harsh conditions for water oxidation. In early 1970s, colloidal noble metal oxide particles were evaluated as highly efficient WOCs especially the iridium oxides[95,96] and ruthenium oxides[97,98]. One recent example used SBA-15 confined $RuO_2$ nanoparticles as catalyst for chemical and photochemical

water oxidation. Under the optimized conditions, a high TOF of 0.027 $s^{-1}$ with an $O_2$ yield of 95 % was achieved in photocatalytic water oxidation reaction using $Ru(bpy)_3^{2+}$ as photosensitizer[99]. Another intriguing observation is that succinic stabilized $IrO_2$ capable of function as both photosensitizer and catalyst. The photocatalytic process involves a visible excitation between Ir-d ($t_{2g}$) and Ir-d ($e_g$) bands[100]. Although the noble metal based metal oxides have been demonstrated to be efficient WOCs, these metals are among the scarcest element on earth, which limited their prospect for large-scale application.

As a result, great efforts have been made to develop first-row transition metal WOCs. In light of that WOC of photosystem II in nature is composed of four manganese atoms, many cubane manganese clusters have been investigated as WOCs[101-103]. However, they are found to be precursors of active manganese oxides[104,105]. Some other manganese complexes are even reported to decompose to form manganese oxide without addition of oxidant[106,107]. One challenge is hard to identify the structure of the generated manganese oxide since they have more than 30 types of crystal structure with different valencies[108]. Dimukes and Greenblat studied the relationship between structure and activity[109]. They concluded that most manganese oxides are efficient WOCs while α-$MnO_2$ and β-$MnO_2$ are inactive. Unfortunately, these active manganese oxides can only work at alkaline conditions. Their performance for catalytic water oxidation will significantly drop at neutral pH. Recently, particular interest is dedicated to study the calcium manganese oxides[110,111] since the calcium has been demonstrated an essential component of WOCs in photosystem II[112]. Several examples containing the $CaMn_3O_4$ cubane core have shown enhanced activity compared with those only containing bare manganese cubane core[110,113]. The obtained results to date indicate that the biomimetic manganese oxides are efficient WOCs. Higher activity can be obtained by simple substitution of inactive metal center. These investigations also provide useful insights for the development more biomimetic metal oxides for catalytic water oxidation.

Apart from manganese oxides, another most studied heterogeneous first-row transition metal WOCs are catalysts containing cobalt. The most well-known one

should be the cobalt phosphate (Co-Pi) discovered by Nocera[114]. It is self-assembled in aqueous phosphate buffer solution containing cobalt (II) salts when external potential is applied. The analysis of its structure by XAS and EXAFS found that it possessed cobalt cubane-type structural motif mimicking the tetranuclear manganese cluster in the natural photosynthetic systems[115,116]. The in situ formed Co-Pi film exhibited a TOF of $2\times10^{-3}$ $s^{-1}$ with an overpotential of 410 mV in neutral water. Its ability of undergo self-assembly and self-healing together with its high efficiency make it one of the most potential candidate for practical application[117].

Another cobalt-based WOC containing the cubane motif is the spinel $Co_3O_4$. In early 1988, Harriman has found that spinel $Co_3O_4$ was an efficient WOC for electrochemical water oxidation[118]. Recently, Singh studied the electrochemical catalytic performance of spinel $Co_3O_4$ and La-doped $Co_3O_4$ for water oxidation[119]. The application of $Co_3O_4$ in photocatalysis was discovered very recently with an initial work by Jiao and Frei[120]. Since then, many works have been done to investigate the spinel $Co_3O_4$ as WOCs in photocatalysis using $[Ru(bpy)_3]^{2+}$ as the photosensitizer as summarized in Table 2-1.

**Table 2-1** Summary of $Co_3O_4$ based photocatalytic water oxidation reaction.

| **Sample** | **TOF ($s^{-1}$ per Co)$\times10^3$** | **Notes** | **Ref.** |
|---|---|---|---|
| **$Co_3O_4$/SBA-15** | 0.34[a] | Nanorods in channel of SBA-15 | 2012[121] |
| **$Co_3O_4$/KIT-6** | 0.41[a] | Three-dimensional structure in pores of KIT-6 | 2012[121] |
| **$Co_3O_4/Al_2O_3$** | 0.46[a] | Nanoparticles on the surface | 2012[121] |
| **$Co_3O_4$ (6nm)** | 0.25[a] | Free nanoparticles | 2012[121] |
| **Mg-$Co_3O_4$** | 0.24[b] | Mg doped mesoporous $Co_3O_4$ | 2013[122] |
| **$Co_3O_4$/SBA-15** | 0.64[c] | $Co_3O_4$ immobilized on SBA-15 | 2013[123] |
| **Mn-$Co_3O_4$** | 0.87[d] | Mn doped $Co_3O_4$ | 2014[124] |
| **Ni-$Co_3O_4$** | 0.45[d] | Ni doped $Co_3O_4$ | 2014[124] |

| | | | |
|---|---|---|---|
| **$Co_3O_4$/C/SiO2** | 0.92[e] | $Co_3O_4$ loaded on mesoporous carbon. | 2014[125] |

a. 75 mg catalyst, 1.67 mM $[Ru(bpy)_3]Cl_2$, 13.5 mM $Na_2S_2O_8$, , $Na_2SiF^{6-}$, $NaHCO_3$ buffer, pH = 5.8, 300 W Xe lamp, λ>400 nm.

b. 10 mg catalyst, 1.5 mM $[Ru(bpy)_3]Cl_2$, 13.5 mM $Na_2S_2O_8$, , $Na_2SiF_6$−$NaHCO_3$ buffer, pH = 5.8, 300 W Xe lamp, λ>400 nm.

c. 200 mg catalyst, 1.5 mM $[Ru(bpy)_3]Cl_2$, 13.5 mM $Na_2S_2O_8$, $Na_2SiF_6$−$NaHCO_3$ buffer, pH = 5.8, 240 mW emission line (476nm) of an Ar ion laser.

d. 18 mg catalyst, 1.5 mM $[Ru(bpy)_3]Cl_2$, 13.5 mM $Na_2S_2O_8$, $Na_2SiF_6$−$NaHCO_3$ buffer, pH = 5.8, 300 W Xe lamp, λ>400 nm.

e. 10 mg catalyst, 1.0 mM $[Ru(bpy)_3]Cl_2$, 5.0 mM $Na_2S_2O_8$, $Na_2SiF_6$−$NaHCO_3$ buffer, pH = 9, 300 W Xe lamp, λ>400 nm.

According to the obtained results, we can conclude as following:

(1) The spinel $Co_3O_4$ nanoparticles with smaller size are significantly more active as WOCs.

(2) The three-dimensional porous KIT-6 loaded $Co_3O_4$ showed higher activity than the two-dimensional structure loaded one. It indicates that the three-dimensional porous structure provide better accessibility to catalytic sites.

(3) The immobilized $Co_3O_4$ nanoparticles showed higher activity and better recyclability than free ones demonstrating that the supports can hinder the nanoparticles from aggregations.

(4) The Mg-$Co_3O_4$ shows an induction for photocatalytic water oxidation since the catalyst undergo surface restructuring, where leaching of Mg creates defects. It implies that the initial structure is less important for long-term water oxidation.

(5) The doping of Mn suggests that higher activity is achievable by doping of Mn in certain lattice.

These studies provide us many useful clues for further improving the photocatalytic performance of $Co_3O_4$ such as immobilizing the $Co_3O_4$ on certain supports. Many efforts are made to reduce the nanoparticle size and prevent the nanoparticles from

aggregation. Moreover, the environment and structure surrounding the $Co_3O_4$ are essential as they also affect the catalytic performance. Therefore, searching for new methods of modifying $Co_3O_4$ nanoparticles such as immobilizing the $Co_3O_4$ on certain supports are necessary to make it a more efficient WOC.

### 2.3.2 Homogeneous WOCs

Since the early findings of Ruthenium based complexes as WOCs[126,127], great amount of mononuclear and multinuclear WOCs constructed of ruthenium and iridium have been investigated[128-131]. However, most ruthenium and iridium based WOCs are applied in electrocatalysis and are suffered from degradation[132]. Nevertheless, these findings result in great interest in design of molecular WOCs based on earth abundant first-row transition metals including manganese, iron and cobalt.

As a metal chosen by nature in photosystem II, manganese has attracted many interests from scientists. Manganese has a wide range of oxidation states, which make it promising in mulitelectron catalysis. However, theses high-valent states also bring the problem of instability demanding for ligand stabilization to prevent them from degradation. It requires that these ligands must be robust and stable enough against oxidation degradation. Thus, only a few stable manganese-based WOCs for photocatalysis are discovered[133]. Even though, the derivatives produced by the degradation of manganese complexes are suspected to be the real catalyst for water oxidation.

Recently, iron is recognized as suitable elements for preparing WOCs since it is abundant on earth, low toxic and natural available[134,135]. Like manganese, the access of high oxidation states makes iron prospective in mulitelectron catalysis while also requires robust ligand to stabilize the architecture of high-valent iron species[136]. Therefore, it is challenging to design an iron-based complex with feasible structure and enough robustness for catalytic water oxidation reactions. The first example was reported in 2010 using $Ce^{4+}$ as oxidant[137]. Later, light driving water oxidation using

iron based WOCs was reported in 2013[138]. However, it was found that the $Fe_2O_3$ derived from the complexes were found to be the true catalysts for water oxidation.

In early 1980s, the simple cobalt salts have been realized to be active in catalytic water oxidation[139]. However, the interest in preparation of molecular cobalt-based WOCs was negligible until the finds of heterogeneous Co-Pi catalyst by Nocera. Since then, scientists are dedicated to develop efficient molecular cobalt-based WOCs. Unfortunately, the progress is hindered by the instability $Co^{2+}$ center. Though cobalt-based WOCs applied in electrocatalysis have been explored for several years, the first example capable of catalyzing water oxidation using the visible light as driving force was reported by the group of Lau in 2012[140]. Then, Sakai's group discovered that a series of cobalt-porphyrin complexes are active in photocatalytic waster oxidation using $[Ru(bpy)_3]^{2+}$ as the photosensitizer[141]. Later, the group of Pizzolato demonstrated that the cobalt salophen is an efficient catalyst for both electrochemical and photochemical water oxidation[142]. Recently, Ding and Ma reported a single-site cobalt salen complex which showed high activity toward photocatalytic water oxidation.[143] Lately, they found that the $CoO_x$ derived from the above complex was responsible for the activity.

The first-row transition metal based metal complexes are found to be active in catalytic water oxidation. Unfortunately, majority of them are not robust enough to withstand the highly oxidizing conditions. The coordinated organic ligands are degraded after long time reaction. Thus, development of carbon free molecular catalysts based on first-row transition metals may be an alternative. Polyoxometalates (POMs) are a series polyatomic ions, consisting of early transition metals (eg., V, Nb, W, Mo) bridged by oxygen atoms. Metals in POMs are usually in their highest oxidation state with $d^0$ electronic configuration, which make them to be oxidative inert. The POMs serving as WOCs can undergo fast and reversible mulitelectron-transfer redox transformations without significant structural alteration. Their oxygen-enriched surfaces can also provide robust all-inorganic systems to encapsulate and protect active WOCs. Another advantage of POMs working as WOCs is that their structure is amendable for further mechanistic and computational

study. The photocatalytic water oxidation using of POM was WOCs are summarized in Table 2-2.

**Table 2-2** Summary of photocatalytic water oxidation using of POM was WOCs.

| POM | TOF($s^{-1}$) | Reaction conditions | Ref. |
|---|---|---|---|
| **$Rb_8K_2[\{Ru_4O_4(OH)_2(H_2O)_4\}(\gamma\text{-}SiW_{10}O_{36})_2]$** | 0.08 | Xe lamp (420-520nm), 5.0μM catalyst, 1.0mM $[Ru(bpy)_3]^{2+}$, 5.0mM $Na_2S_2O_8$, 20mM sodium phosphate buffer(pH=7.2). | [144]2009 |
| **$Cs_9[(\gamma\text{-}PW_{10}O_{36})_2Ru_4O_5(OH)(H_2O)_4]$** | 0.13 | Xe lamp (420-520nm), 5.0μM catalyst, 1.0mM $[Ru(bpy)_3]^{2+}$, 5.0mM $Na_2S_2O_8$, 20mM sodium phosphate buffer(pH=7.2). | [145]2010 |
| **$Cs_{10}[Ru_4O_4(OH)_2(H_2O)_4(\gamma\text{-}SiW_{10}O_{36})_2]$** | 0.008 | 50 W LED lamp (λ>550nm), 60μM catalyst, 0.1mM $[Ru\{(\mu\text{-}dpp)Ru(bpy)_2\}_3]^{8+}$, 10mM $Na_2S_2O_8$, 10mM phosphate buffer(pH=7.2). | [146]2010 |
| **$Na_{10}[Co_4(H_2O)_2(\alpha\text{-}PW_9O_{34})_2]$** | - | Xe lamp (420-520nm), 5.0μM catalyst, 1.0mM $[Ru(bpy)_3]^{2+}$, 5.0mM $Na_2S_2O_8$, 20mM sodium phosphate buffer(pH=7.2). | [147]2011 |
| **$K_{10.2}Na_{0.8}[\{Co_4(\mu\text{-}OH)(H_2O)_3\}(SiW_{19}O_{70})]$** | 0.1 | Xe lamp (420-520nm), 10μM catalyst, 1.0mM $[Ru(bpy)_3]^{2+}$, 5.0mM $Na_2S_2O_8$, 25mM sodium borate buffer(pH=9.0). | [148]2012 |
| **$K_{10}H_2[Ni_5(OH)_6(H_2O)_3(Si_2W_{18}O_{66})]$** | - | LED lamp (455nm), 1.0mM $[Ru(bpy)_3]^{2+}$, 5.0mM $Na_2S_2O_8$, 25mM sodium borate buffer(pH=8.0). | [149]2012 |
| **$Cs_{10}[Ru_4(\mu\text{-}O)_4(\mu\text{-}OH)_2(H_2O)_4(\gamma\text{-}SiW_{10}O_{36})_2]$** | 280 | Laser, 0.5μM catalyst, 0.1mM $[Ru(bpy)_3]^{2+}$, 5.0mM $Na_2S_2O_8$, 80mM sodium phosphate buffer(pH=7.0). | [150]2012 |
| **$\alpha\text{-}K_6Na[\{Ru_3O_3(H_2O)Cl_2\}(SiW_9O_{34})]$** | 0.7 | LED lamp (470 nm), 50 μM catalyst, 1.0mM $[Ru(bpy)_3]^{2+}$, 5.0mM $Na_2S_2O_8$, 20mM $Na_2SiF_6$ buffer(pH=5.8). | [151]2012 |
| **$K_{11}Na_1[Co_4(H_2O)_2(SiW_9$** | 0.4 | LED lamp (470 nm), 42 μM catalyst, | [151]2012 |

| | | | |
|---|---|---|---|
| **$O_{34})_2$]** | | 1.0mM $[Ru(bpy)_3]^{2+}$, 5.0mM $Na_2S_2O_8$, 20mM $Na_2SiF_6$ buffer(pH=5.8). | |
| **$(NH_4)_3[CoMo_6O_{24}H_6]$** | 0.11 | 300 W Xe lamp (420-490nm), 20μM catalyst, 0.4mM $[Ru(bpy)_3]^{2+}$, 3.0mM $Na_2S_2O_8$, 100mM sodium borate buffer buffer(pH=8.0). | [152]2012 |
| **$(NH_4)_6[Co_2Mo_{10}O_{38}H_4]$** | 0.16 | 300 W Xe lamp (420-490nm), 20μM catalyst, 0.4mM $[Ru(bpy)_3]^{2+}$, 3.0mM $Na_2S_2O_8$, 100mM borate buffer (pH=8.0). | [152]2012 |
| **$K_7[Co^{III}Co^{II}(H_2O)W_{11}O_{39}]$** | 0.5 | 16 mW LED lamp (λ>420nm), 15μM catalyst, 1.0mM $[Ru(bpy)_3]^{2+}$, 5.0mM $Na_2S_2O_8$, 80mM borate buffer(pH=9). | [153]2013 |
| **$Na_{10}[Co_4(H_2O)_2(α\text{-}VW_9O_{34})_2]$** | - | 17mW LED lamp (455 nm), 2.0 μM catalyst, 1.0mM $[Ru(bpy)_3]^{2+}$, 5.0mM $Na_2S_2O_8$, 80mM borate buffer(pH=9.0). | [154]2014 |
| **$Na_{30}K_2[\{Co_4(OH)_3(PO_4)\}_4(SiW_9O_{34})_4]$** | 0.053 | 300 W Xe lamp (420-800nm), various catalyst, 1.0mM $[Ru(bpy)_3]^{2+}$, 5.0mM $Na_2S_2O_8$, 80mM borate buffer (pH=9.0). | [155]2014 |
| **$Na_{30}K_2[\{Co_4(OH)_3(PO_4)\}_4(GeW_9O_{34})_4]$** | 0.105 | 300 W Xe lamp (420-800nm), various catalyst, 1.0mM $[Ru(bpy)_3]^{2+}$, 5.0mM $Na_2S_2O_8$, 80mM borate buffer(pH=9.0). | [155]2014 |
| **$Na_{28}[\{Co_4(OH)_3(PO_4)\}_4(PW_9O_{34})_4]$** | - | 300 W Xe lamp (420-800nm), various catalyst, 1.0mM $[Ru(bpy)_3]^{2+}$, 5.0mM $Na_2S_2O_8$, 80mM borate buffer (pH=9.0). | [155]2014 |
| **$Na_{28}[\{Co_4(OH)_3(PO_4)\}_4(AsW_9O_{34})_4]$** | - | 300 W Xe lamp (420-800nm), various catalyst, 1.0mM $[Ru(bpy)_3]^{2+}$, 5.0mM $Na_2S_2O_8$, 80mM borate buffer (pH=9.0). | [155]2014 |

An initiative discovery of POM as efficient WOC was reported simultaneously by

two independent group[156,157]. They found that $[\{Ru_4O_4(OH)_2(H_2O)_4\}(\gamma\text{-}SiW_{10}O_{36})_2]^{10-}$ (RuSiPOM) comprising a tetraruthenate can carry out water oxidation reaction at neutral condition (pH=7) using $[Ru(bpy)_3]^{3+}$ as oxidant or at acidic condition (pH=0.6) using $Ce^{4+}$ as the oxidant. Hill's group then investigated its performance for photocatalytic water oxidation[144]. A TOF of 0.08 $s^{-1}$ and a quantum efficiency of 0.045 were then obtained for the RuSiPOM using $[Ru(bpy)_3]^{2+}$ as the photosensitizer. The first POM-based WOCs $[Co_4(H_2O)_2(\alpha\text{-}PW_9O_{34})_2]^{10-}$ (CoPOM) comprised of earth abundant elements was found by Hill in 2010[158]. It was reported that 0.12 μM of CoPOM showed a TOF > 5 $s^{-1}$. Light driving water oxidation with CoPOM was also achieved later by Hill and his coworkers[147]. Since then, many POMs containing cobalt capable of catalyzing water oxidation have been reported as summarized in Table 2.

Despite the aforementioned achievements, the POM-based WOCs also suffer from the drawbacks of instability. The carbon-free POMs are stable to oxidative degradation and heat as indicated above. However, the hydrolytic stability is a main concern since many POMs will decompose to form metal oxide under certain pH. To find the solutions, Bonchio and Hill immobilize the RuSiPOM on multiwalled carbon nanotubes[159] (MWCNT) and graphene[160] respectively. Both of them found that the RuSiPOM interfacing with the supports showed enhanced activities and improved stabilities. Xie and coworkers studied the effect of carbon nitride to CoPOM by immobilizing the latter to the former[161]. As anticipated, the combination of CoPOM and carbon nitride resulted in higher electrocatalytic activity due to the synergistic effect between them. In addition, the immobilization of soluble POMs on substrates also makes them to be recovered from the solution more easily, which is essential for practical application. Thus, it can be concluded that immobilization of POMs on some substrates have been demonstrated an efficient method to stabilize POMs and enhance their activity for water oxidation.

### 2.3.4 Summary

Both heterogeneous and homogeneous WOCs are reviewed. The catalytic activities of heterogeneous WOCs are strongly affected by their crystal phase, particle size and

morphology. Compared with the heterogeneous ones, the homogeneous WOCs are less stable. Nevertheless, studying the homogeneous WOCs help understand the intrinsic mechanism of the water oxidation and provide more useful clues for designing of more efficient catalysts. And it was found that substrates do affect the stability and catalytic performance of both heterogeneous and homogeneous WOCs. Thus, searching for suitable substrates to immobilize the WOCs is an ideal method for improving their activities and stabilities.

## 2.4 Overall water splitting

The Z-scheme water splitting inspired by natural photosynthesis in green plants was introduced by Bard in 1979. The photosystems I and II harvest photons of different wavelengths. Charges move between photosystem I and photosystem II through shuttle redox mediators, oxidizing water to oxygen under visible light. In artificial Z-scheme systems, it is similar that two different photocatalysts named as water oxidation catalysts (WOC) and water reduction catalysts (WRC) are combined by shuttle redox mediators. The basic principle of Z-scheme water splitting is illustrated in Figure 2-6. In a $H_2$ evolution system, water is reduced to hydrogen by reacting with excited electrons at WRCs while the hole is scavenged by the electron donor. Thus electron donor (D) transform to its oxidized form (A). At the WOCs side, water is oxidized to form oxygen and the electron acceptor (A) will reduced at the same time. Thus a cycle of redox pairs of D and A are formed and water is splitting into hydrogen and oxygen during the same time.

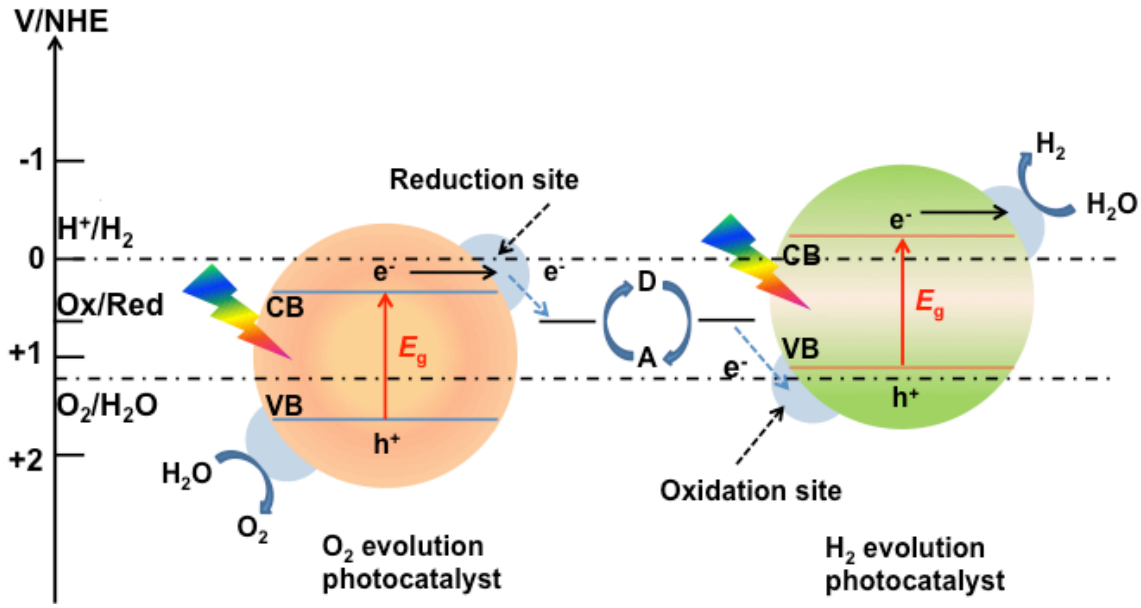


**Figure 2-4** Schematic illustration of z-scheme water splitting.

In the past decades, numbers of systems have been explored for Z-scheme water splitting. Kudo and coworkers reported a system in 2004, in which 1% Rh doped $SrTiO_3$. A quantum yield of 0.3% was obtained at 440 nm when $BiVO_4$, Then in 2009, Sayama found the $Cs^+$ treated $PtO_x$. Three times higher activity was achieved compared with the system using untreated PtO*x*/$WO_3$ worked as WRC and $Bi_2Mo_2O_6$, $WO_3$, or $BiVO_4$ functioned as $WOC_4$ was used as WOC under visible light and $Fe^{2+}/Fe^{3+}$ were employed as redox mediators. Before that, Abe et al. reported a system consisting of Pt loaded $SrTiO_3$ doped with Cr and Ta and $PtO_x$-loaded $WO_3$ with $I^-/IO^{3-}$ as mediators. $_x$-$WO_3$ obtains 10 times higher activity for oxygen evolution in the presence $I^{3-}$. This finding was applied in Z-scheme water splitting using a mixture of Pt/$SrTiO_3$:Cr/Ta and $Cs^+$-treated PtO*x*/$WO_3$ under visible light$_3$. It is also possible to apply a photocatalyst treated with different methods to both sides of the system. Kudo reported such a system containing Na and V codoped $SrTiO_3$ as an oxygen evolution catalyst and Rh doped $SrTiO_3$ as hydrogen evolution catalyst when Ru was loaded on both sides as cocatalysts. In particularly, besides $Fe^{3+}/Fe^{2+}$ and $IO^{3-}/I^-$ couples,

$[Co(bpy)_3]^{3+/2+}$, $[Co(phen)_3]^{3+/2+}$ and even reduced graphene oxide were found effective redox mediators in the $Ru/SrTiO_3$:Rh and $BiVO_4$ systems. Kudo and coworkers also reported that this system even can work just by inter particle electron transfer without adding any mediator.

Other than metal oxides, metal (oxy)nitrides are also applied in Z-scheme water splitting. Compared with metal oxides, metal (oxy)nitrides may be more suitable materials to be applied in Z-scheme systems because of their proper band position. In 2005, Abe et al. reported a Z-scheme system containing a Pt-loaded TaON as a HER. A higher quantum yield of 0.5% was obtained compared with above-mentioned examples. Perovskite oxynitrides of $ATaO_3$ having absorption edges at 520, 600, and 660 nm respectively, were examined as a $H_2$ evolution photocatalyst in Z-scheme water splitting for the purpose of better utilizing of visible light. However an even lower quantum yield of 0.1% was obtained because of defects on their surface. Domen et al. discovered that the defects on the surface of the oxynitides could be suppressed by $ZrO_2$. A six times higher quantum yield of 6.2% was obtained by combining Pt-loaded $ZrO_2$ $ZrO_2$/TaON with PtO*x*/$WO_3$ and an $IO^{3-}/I^-$ shuttle redox mediator.

## 2.5 Summary of literature review

Compared with the semiconductor based photocatalytic systems, the dye-sensitized systems take the advantages of separation of light absorber and catalyst just as that done in nature. Thus, we can optimize both components for better utilization of solar energy and higher catalytic efficiencies. It is inspiring to learn from nature to design some low cost biomimetic complexes. The work presented in Chapter 3 was dedicated to studying the complexes with various coordination environments, which can help us understand the intrinsic mechanism and provide us clues for design of more efficient biomimetic catalysts.

Both the homogeneous and heterogeneous WOCs suffered from the problem of instability for prolonged photocatalytic reactions. It has been demonstrated that

immobilization of WOCs on proper substrates helps improve stability and activities. In Chapters 4 and 5, we report the use of the one metal-organic framework as the substrate to investigate its effect on activities and stabilities of both homogeneous and heterogeneous WOCs.

# CHAPTER 3 DYESENSITIZED NICKEL COMPLEXES WITH MIXED DONORS FOR HYDROGEN PRODUCTION

(This chapter is adapted from " J. Y. Han, W. Zhang, T. H. Zhou, X. Wang, R. Xu, Nickel-complexes with a mixed-donor ligand for photocatalytic hydrogen evolution from aqueous solutions under visible light, RSC Advances, **2012**, 2, 8293-8296." Reproduced from ref.162 with permission of The Royal Society of Chemistry)[162]

## 3.1 Introductions

As indicated above, biomimetic metal complexes made of earth abundant Ni, Co and Fe are prospect catalysts for hydrogen production under visible light when sensitized with dyes. In a previous work of our group, a nickel-thiolate complex self-assembled in aqueous solution of TEOA also was discovered to show high efficiency[91]. This complex formed between Ni(II) and 2-mercatoethanol (Ni-ME) obtained a quantum efficiency of 25% at 460 nm when sensitized with Erythrosin Y. In light of the knowledge that some enzymes have been shown to contain Ni in the active sites with a variety of coordination types, model complexes involving mixed donors are worthwhile studying. In this work, a simple ligand with N and S donors, β-mecaptoethylamine (L), was chosen to form a mononuclear complex $NiL_2$, which could be further transformed to trinuclear complex $Ni(NiL_2)_2$ reacting with Ni(II) (Figure 3-1). The facile preparation method of $NiL_2$ crystal was described by Jicha and Busch half a century ago[163]. Both complexes were found as active catalysts for hydrogen evolution in aqueous solutions when sensitized by Erythrosin yellowish (EY).

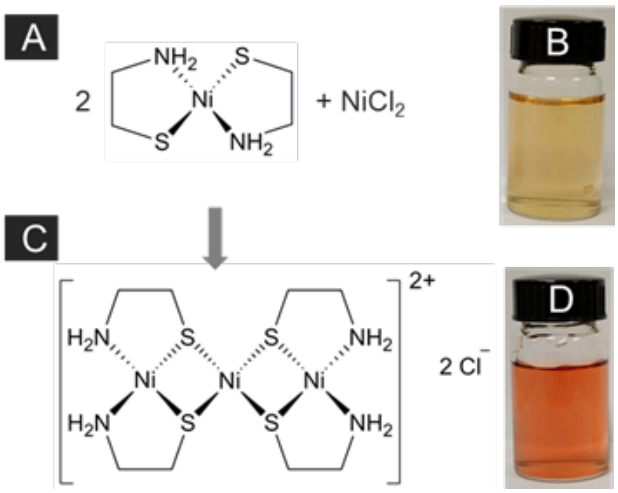


**Figure 3-1** Molecular structure of the complexes, (A) $NiL_2$ and (C) $Ni(NiL_2)_2Cl_2$, and photos of aqueous solutions of (B) $NiL_2$ (60 $^oC$, 1.6 mM ) and (D) $Ni(NiL_2)_2Cl_2$ (room temperature, 0.8 mM).

## 3.2 Experimental methods

### 3.2.1 Preparation of materials

Sodium hydroxide, 2-mercaptoethylamine hydrochloride, nickel chloride hexahydrate, Erythrosin yellowish (ErY) and Triethanolamine (TEOA) were purchased from Alfa Aesar. These reagents were analytical grade and used without further purifications. All the other starting materials were of reagent grade quality and were obtained from commercial sources without further purification.The preparation of Ni(II) complexes was according to the previous report by Jicha and Busch with slight modifications[163].

**$Ni(NH_2CH_2CH_2S)_2$ [$NiL_2$]**. First, 10.5 mmol of 2-mercaptoethylamine hydrochloride and 20 mmol of sodium hydroxide were dissolved in 20 mL of deionized water. This clear ligand solution was added dropwise to a 20 mL aqueous solution containing 5 mmol of nickel chloride hexahydrate at 60 $^oC$ under stirring. The color of the solution turned red at the beginning of ligand addition. After the complete addition, the red color faded and green crystals were precipitated from the solution. The stirring was continued for another 15 min after which the mixture was allowed to cool to room temperature. The green crystal was collected by filtration and

washed with deionized water and ethanol before being dried in vacuum at 50 $^{o}$C. Yield: 92% (0.97 g). Composition calculated for $C_4H_{12}N_2NiS_2$: C, 22.77; H, 5.73; N, 13.28; S, 30.40. Found: C, 22.75; H, 5.92; N, 13.18; S, 30.52.

**$[Ni(Ni(NH_2CH_2CH_2S)_2)_2]Cl_2$ $[Ni(NiL_2)_2Cl_2]$**. Briefly, 13.2 mmol of 2-mercaptoethylamine hydrochloride was dissolved in 12.5 mL of ethanol. Then, a second solution was prepared by dissolving 26.4 mmol of sodium hydroxide in 50 mL of aqueous ethanol (volume ratio of water/ethanol = 2:3). The second solution was added into the first one followed by removal of sodium chloride formed during the neutralization by filtration. Then the ligand solution was added dropwise to a 15 mL aqueous solution containing 9.9 mmol of nickel chloride hexahydrate at 60 $^{o}$C under stirring. The solution turned to red in color and the dark green crystals were precipitated from the red solution immediately. After complete addition of the ligand, the final solution was allowed to stand in the ice bath for 2 h for better crystallization. The crystal formed was separated by filtration and washed with cold ethanol. The final product was dried in vacuum at 50 $^{o}$C for 1 d. Yield: 77% (1.39 g). Composition calculated for $C_8H_{24}C_{l2}N_4Ni_3S_4$: C, 17.42; H, 4.39; N, 10.16; S, 23.25. Found: C, 17.39; H, 4.38; N, 10.11; S, 23.56.

### 3.2.2 Materials characterization

Powder X-ray diffraction (XRD) patterns of $NiL_2$ and $Ni(NiL_2)_2Cl_2$ crystals were recorded on a X-ray diffractometer (Bruker AXS D8, Cu $K_\alpha$, $\lambda$ = 1.5406 Å, 40 kV and 20 mA) in the range of 10 $^{o}$–60 $^{o}$. The simulated XRD patterns were calculated using single-crystal X-ray diffraction data, which was obtained from Cambridge Crystallographic Data Centre (CCDC) and processed by Mercury v1.4 program provided by CCDC. Fourier transform infrared (FTIR) spectra were obtained on a Digilab FTS 3100 FTIR with a 4 $cm^{-1}$ resolution and in the range of 400-4000 $cm^{-1}$ using a standard KBr disk technique. Elemental analysis for C, H, N, and S was performed on a Vario EL III Element analyzer. The UV-visible absorption spectra were obtained on an UV-visible spectrophotometer (UV-2450, Shimadzu). Cyclic voltammetry experiments were performed on CHI 660D electrochemical station under

a three-electrode cell system consisting of a glassy carbon working electrode, a Pt wire counter electrode and a saturated calomel reference electrode. $NiL_2$ complex was dissolved in water by heating the solution to 60 $^oC$ at a concentration of 1.6 mM. The concentration of $Ni(NiL_2)_2Cl_2$ was 0.8 mM. All measurements were carried out in aqueous solutions after purging of Argon thoroughly. The scan started at reduction with a rate of 50 mV/s for all measurements. All redox potentials were reported versus SCE.

### 3.2.3 Photocatalytic water splitting measurement

Visible light driven hydrogen evolution reactions were conducted in a closed gas circulation and evacuation system fitted with a top window Pyrex cell. A circulating cooling water system was used to maintain the reactor at room temperature. In a typical reaction, 0.16 mmol of $NiL_2$ complex and 0.32 mmol of Erythrosin yellowish (ErY) were added to 100 mL of 15 vol% triethanolamine (TEOA) solution under vigorous stirring. The pH value of the TEOA solution was prior adjusted to 8.5 using concentrated aqueous $HNO_3$ solution. The light source was a 300 W Xenon lamp with a long-pass cut-off filter ($\lambda > 420$ nm). The produced hydrogen was detected using an online gas chromatography. Different long-pass filters ($\lambda > 420$, 455, 475, 500 and 520 nm) and band-pass filters (centered at 420, 440, 460, 480, 500, 520, 550 nm) were equipped when conducting reactions under photons of different wavelengths and collecting quantum efficiency (QE) results, respectively. The reaction solutions were irradiated under $\lambda > 420$ nm for 1 h before switching to band-pass filters during QE measurement. The amount of hydrogen produced in the subsequent 2 h was used to calculate QE using the equation 10. The number of photons from irradiation was measured using a silicon photodiode (13 DAS 005, MELLES GRIOT) connected to a broadband power/energy meter (13 PEM 001, MELLES GRIOT).

## 3.3 Results and discussion

The configuration around Ni(II) atom is square planar and the crystal structure is made up of *trans* $NiL_2$ according to single crystal X-ray diffraction study, although

*trans-cis* isomerization could occur in the solution[164]. The obtained green solid was characterized by XRD, FTIR, UV-vis and CHNS elemental analyses. All the analytic results consistently showed the formation of $NiL_2$ complex (Figure 3-2). Although

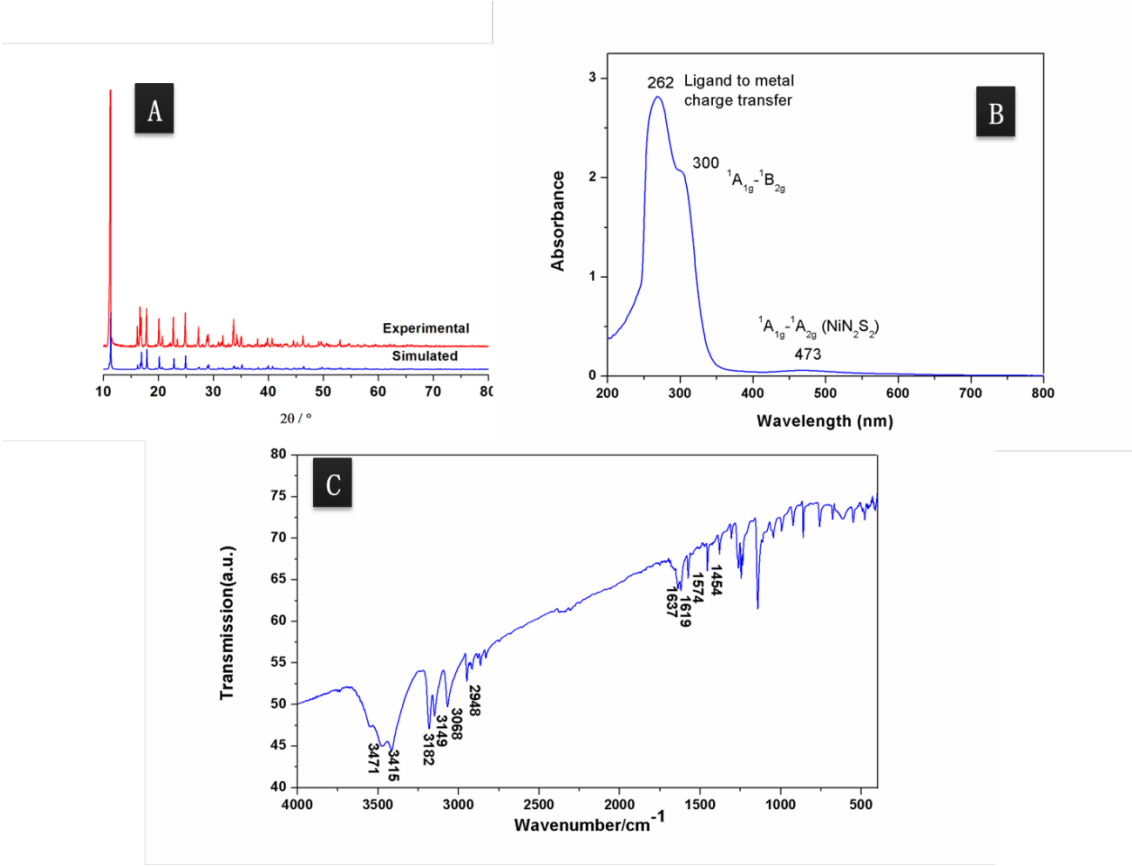


**Figure 3-2** (A) Simulated and experimental XRD patterns of mononuclear $NiL_2$ complex powder. (B) UV-vis spectrum of $NiL_2$ complex dissolved in water (0.8 mM, 60 $^oC$). (C) FTIR spectrum of $NiL_2$ complex.

$NiL_2$ is only slightly soluble in aqueous solution, upon raising the temperature to around 60 $^oC$, the solid can be completely dissolved at a concentration of 1.6 mM (the optimized concentration for photoreaction) or higher and the solution exhibits a light orange color (Figure 3-1B). The UV-vis spectrum (Figure 3-2B) shows the characteristic ligand-to-metal charge transfer (262 nm), $^1A_{1g} - {}^1B_{2g}$ transition (300 nm) and $^1A_{1g} - {}^1A_{2g}$ transition (473 nm) of $NiN_2S_2$ chromophore[165]. In aqueous solution, two $NiL_2$ complexes can further act as ligands to coordinate to the third Ni(II) ion *via* both thiolate sulfur donors to form a trinuclear cluster which is positively charged and soluble in water, $Ni(NiL_2)_2^{2+}$ (Figure 3-1C and 3-1D)[163]. In addition, the broad and

asymmetric bands indicate an overlap of transitions contributed by both terminal $NiN_2S_2$ and central $NiS_4$[165,166]. Although the properties of these two complexes have been studied to a certain extent, their catalytic activities in photocatalytic water splitting reactions have not been explored so far.

The photocatalytic hydrogen evolution reactions were carried out with $NiL_2$ and $Ni(NiL_2)_2^{2+}$ catalysts dispersed and dissolved in aqueous solutions, respectively. Erythrosin yellowish (ErY) and triethanolamine (TEOA) were used as the PS and sacrificial reagent, respectively. The time course of hydrogen evolution is shown in Figure 3-3. It can be seen that both the mono- and trinuclear complexes are active catalysts under visible light irradiation for hydrogen generation. Under the optimized

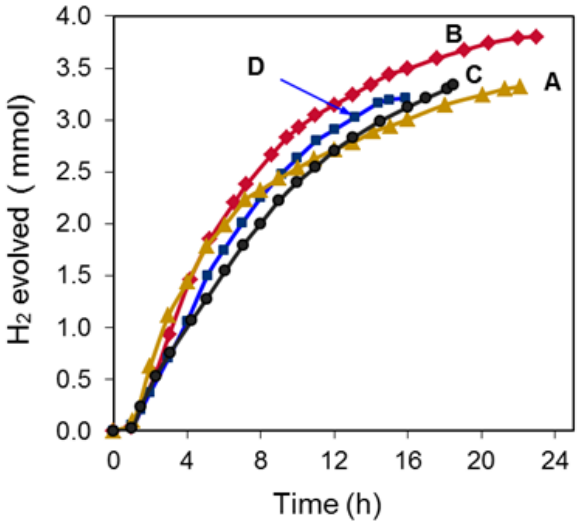


**Figure 3-3** Time course of hydrogen evolution using Ni(II)- mecaptoethylamine complexes, (A) $[NiL_2]$ = 0.8 mM, (B) $[NiL_2]$ = 1.6 mM, (C) $[NiL_2]$ = 2.4 mM, and (D) $[Ni(NiL_2)_2]^{2+}$ = 0.8 mM (100 mL solution, 15 vol% TEOA, [ErY] = 3.2 mM, pH = 8.5, light source: 300 W Xe lamp, $\lambda > 420$ nm).

conditions for $NiL_2$, the amount of hydrogen produced reached 3.8 mmol and the reaction ceased at above 20 h (Figure 3-3B). A slight decrease in the amount of hydrogen generated was resulted when the concentration of $NiL_2$ was lowered to 0.8 mM (Figure 3-3A) or increased to 2.4 mM (Figure 3-3C). Other conditions including the type of xanthene dyes, the concentration of reaction solution were also optimized. The optimum pH value was found as 8.5. In the current system, a basic condition was

necessary to keep the dyes in the deprotonated anion form which is dissolvable in water for efficient light absorption and electron transfer to the catalyst. In addition, it has been shown that protonated TEOA under acidic condition is a less effective donor[79].On the other hand, the activity of the water-soluble trinuclear complex is slightly lower. Under the optimized condition, 3.2 mmol of hydrogen was produced (Figure 3-3D). In all these cases, an induction period of about 1 h was found before substantial amounts of hydrogen evolved. A similar observation was reported by Eisenberg and co-workers on cobaloxime based catalyst[167]. And control experiments suggest that no hydrogen evolved in the absence of PS or catalyst.

Compared to inorganic semiconductor photocatalysts with a narrow light absorption range, the advantage of dye sensitized photocatalyst system lies on the extended visible light absorption to longer wavelengths. As displayed in Figure 3-4, when the cut-off filter of longer wavelengths up to 520 nm was used, the total amount of hydrogen producible for both systems did not change much, although the hydrogen production rate was lowered mainly due to the reduction in light intensity.

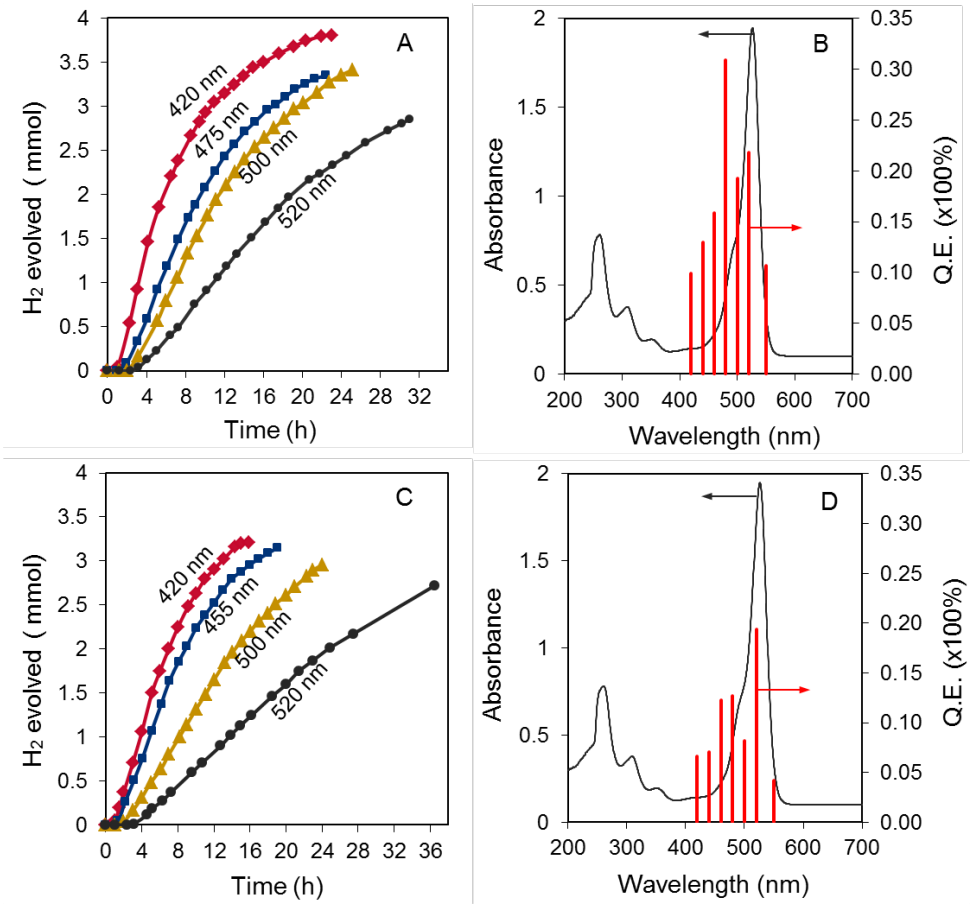


**Figure 3-4** Time course of hydrogen evolution using (A) $NiL_2$ (1.6 mM) and (C) $Ni(NiL_2)_2^{2+}$ (0.8mM) with a 300 W Xe lamp equipped with different long-pass cut-off filters, and the QEs under photons with different wavelengths over (B) $NiL_2$ and (D) $Ni(NiL_2)_2^{2+}$ complexes. Other reaction conditions were the same as those in Figure 3-3.

More remarkably, the quantum efficiency (QE) measured for the system containing $NiL_2$ complex is as high as 30.9% at 480 nm and still remains at 21.8% at 480 nm and still remains at 21.8% at 520 nm (Figure 3-4B). Such features are desirable toward more efficient utilization of visible light (400-700 nm). Compared to $NiL_2$ system, the trinuclear complex $Ni(NiL_2)_2^{2+}$ gave rise to lower QEs with the highest value of 19.3% obtained at 520 nm.

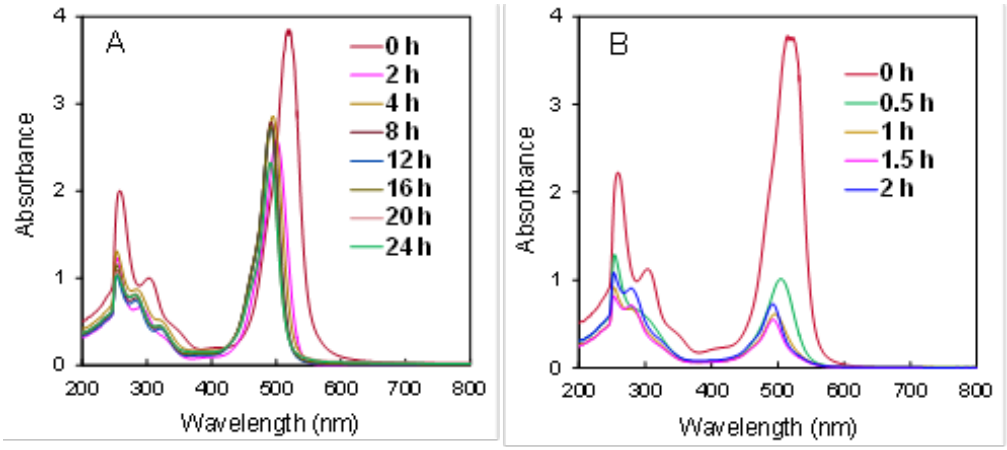


**Figure 3-5** UV-vis spectra of (A) the reaction mixture of $NiL_2$ system at different reaction time (the reaction mixture was filtered before analysis), and (B) the mixture without $NiL_2$ catalyst while keeping other conditions the same. All solutions were diluted 10 times before analysis. The reaction conditions were the same as those in Figure 3-3.

The stability of the PS was studied by monitoring the UV-vis absorption spectrum of the reaction mixture at different reaction time. Heavy halogen-substituted xanthene dyes are known to have high intersystem crossing yield favourable for the formation of long-lived $3\pi\pi^*$ triplet state which injects electron to the catalysts. Nevertheless, the halogen groups can be easily photobleached through reductive quenching[72]. The xanthene ring of ErY is substituted with two iodide atoms. Its halogen-free analogue is fluorescein (FL). The maximum absorption of ErY and FL in aqueous TEOA solution (pH = 8.5) is at around 520 nm and 488 nm, respectively. As shown in Figure 3-5, the PS in the reaction mixture in the presence of $NiL_2$ is much more stable (Figure 3-5A) compared to that without the catalyst but in the presence of TEOA electron donor (Figure 3-5B). At 2 h of photoreaction, the peak position was shifted to 500 nm due to the cleavage of one C-I bond. The peak intensity was also slightly lowered. At longer reaction time, the peak position progressively shifted to 488 nm, corresponding to the loss of the remaining iodide leading to FL. Compared to the previous studies on Ni-thiolate systems involving xanthene dyes[90,91], a better stability of PS in this system was found since there was no significant change in peak intensity

in the period of 2-24 h of reaction. Similar observations were made when trinuclear $Ni(NiL_2)_2^{2+}$ complex was used as the catalyst (Figure 3-6).

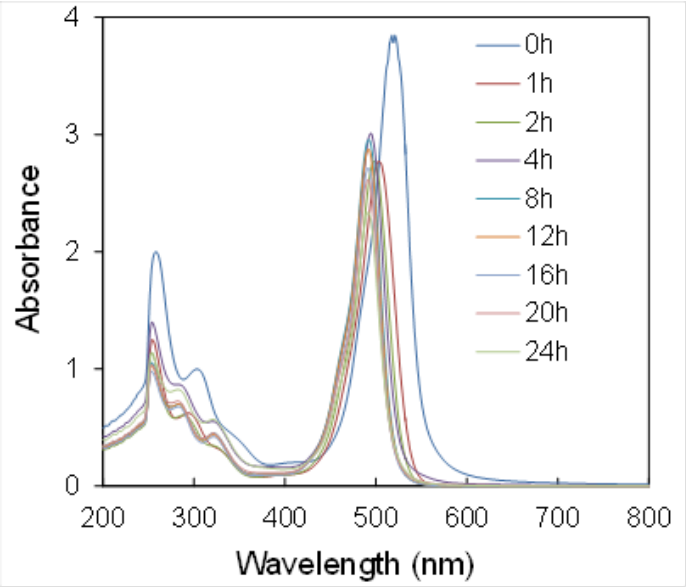


**Figure 3-6** UV-vis spectra of reaction mixture of $Ni(NiL_2)_2^{2+}$ system at different reaction time. All solutions were diluted 10 times before analysis. The reaction conditions were the same as those in Figure 3-4.

In contrast, photobleaching of ErY occurred rapidly in the absence of the catalyst. Figure 3-6B shows that the peak intensity was greatly reduced at 0.5 h of irradiation. Based on the above results, it can be concluded that the favourable electron transfer from the excited state of PS to the catalyst plays an imperative role in improving the stability of PS.

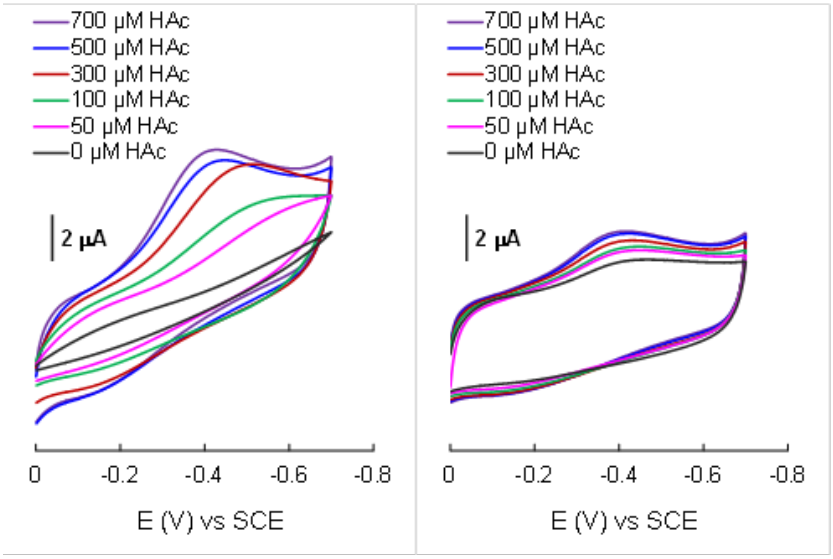


**Figure 3-7** Cyclic voltammograms of (A) $NiL_2$ (1.6 mM, 60 $^oC$) and (B) $Ni(NiL_2)_2^{2+}$ (0.8 mM) in water using a glassy carbon working electrode with a scan rate of 50 mV/s.

Electrocatalytic properties of the complexes were investigated in order to provide some insight to the reaction mechanism. The black cyclic voltammogram (CV) curve in Figure 3-7A for $NiL_2$ in the absence of acid exhibits no reduction waves. In the presence of dilute acetic acid (HAc), the colored curves show that there is an obvious increase in the current. At an HAc concentration of 0.1 mM, a reduction wave can be observed at around -0.5 V (green curve) for Ni(II/I). Hence, it is suggested that the protonated form of $NiL_2$ can accept electron. A similar observation was reported by Eisenberg and co-workers for $[Ni(pyS)_3]^-$ complex in which Ni(II) is in a mixed S and N donor environment[90]. Further increase of acid concentration led to better developed reduction waves. At higher acid concentration of 0.5-0.7 mM, the waves were shifted to more positive positions at about -0.4 V, indicating that protonation of the Ni(I) centre takes place at a rate faster than the overall catalytic rate[168]. Under this condition, the half wave potential of Ni(II/I) is determined by the protonation rate while the current is determined by the overall catalytic rate. The CV curves shown in Figure 3-7B present different behaviour of $Ni(NiL_2)_2^{2+}$ complex. A broad reduction wave around -0.4 V was observed in the absence of acid, consistent with accepting of

electron by the $NiS_4$ chromophore as shown in our earlier work[91]. However, the current did not increase significantly when the acid concentration was increased.

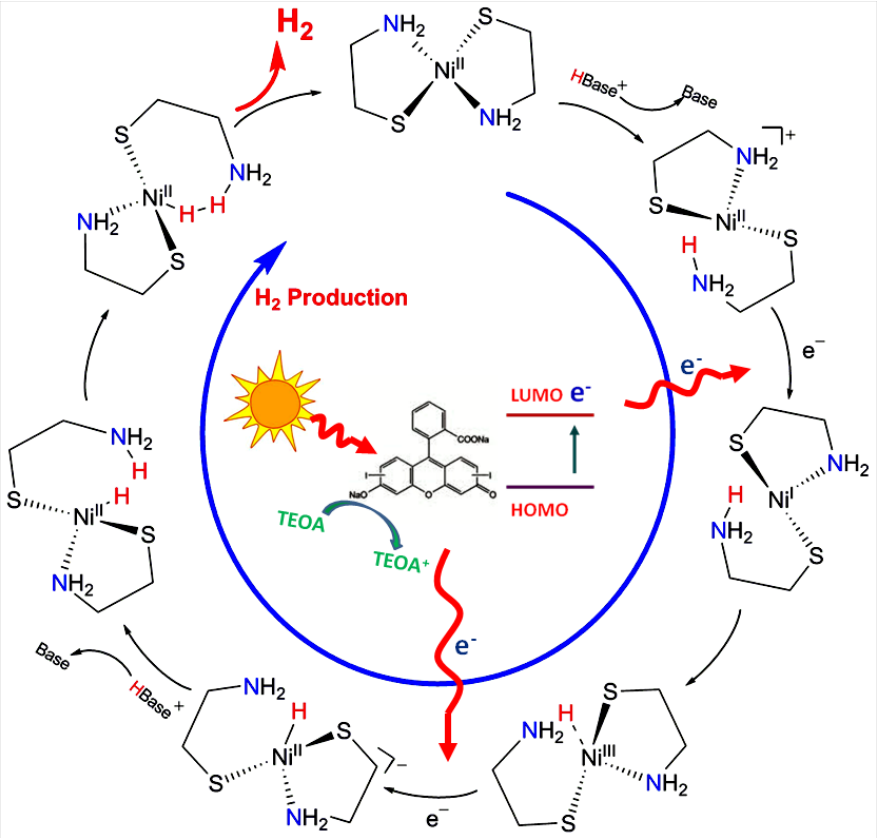


**Scheme 3-1** Proposed mechanism of photocatalytic hydrogen evolution over $NiL_2$ complex using ErY and TEOA as the PS and sacrificial electron donor, respectively.

In light of the results and phenomena obtained so far, a photocatalytic hydrogen evolution mechanism over $NiL_2$ complex is proposed in Scheme 1. The complex is first protonated by adopting a proton from water to the amine species which could cause the breaking of the N chelating to the Ni(II) centre. The resultant protonated complex then electrostaticly interact with depronated PS under basic conditions and further accepts an electron from the excited triplet state of the PS ($^{3*}$ErY) leading to reduction of Ni(II) to Ni(I) species. Both theoretical studies and experimental works have suggested that the base sites like N atoms near the metal centres could act as an intramolecular proton transfer relay for more efficient hydrogen processing[169-171]. In light with this, it is proposed that the proton from N atom is subsequently transferred to the Ni centre and becomes a hydride intermediate, in conjunction with the

acceptance of another electron from the excited PS. In the following step, the complex adopts another proton from water to the same N atom for charge neutralization. Finally, the proton ($H^+$) and hydride ($H^-$) attached to N and Ni atoms, respectively, form a hydrogen molecule as the expected product. After releasing of molecular hydrogen, the complex is restored for the next cycle of hydrogen evolution reaction. Simultaneously, the oxidized PS is reduced by TEOA electron donor. The oxidative quenching pathway was confirmed by the CV studies of the redox potentials of ErY and TEOA.

### 3.4 Conclusion

The present work has shown that the complexes formed between Ni(II) and β-mecaptoethylamine with a mixed S and N donor environment are active and inexpensive catalysts for photocatalytic hydrogen evolution by water splitting. An excellent quantum efficiency of 30.9% was obtained at 480 nm. A reaction mechanism involving intramolecular proton transfer from N atom to Ni centre was proposed. This work provides us with useful clues to further explore noble-metal free complexes with a relevant environment to natural enzymes toward development of earth-abundant photocatalyst systems for solar hydrogen production.

# CHAPTER 4 METAL-ORGANIC FRAMEWORK IMMOBLIZED COBALT OXIDE NANOPARTICELS FOR EFFICEINT PHOTOCATALYTIC WATER OXIDATION

## 4.1 Introduction

Artificial photosynthesis by splitting water into hydrogen and oxygen or converting $CO_2$ into hydrocarbons has been intensively studied towards sustainable development by renewable energy. The water oxidation half reaction is essential for solar fuel production since water is known to be the only cheap and abundant source to provide protons and electrons in a tetra scale. However, improving the efficiency of a catalyst for water oxidation is challenging because forming one oxygen molecule requires overcoming high activation energy to transfer four electrons[120,172]. Inspired by nature, where visible light absorption and the multi-electron catalytic process are conducted by separate components[173], a $Ru(bpy)_3^{2+}$–$Na_2S_2O_8$ system has been developed enabling us to simultaneously optimize visible light capture and multi-electron catalytic rate[118]. To date, colloidal iridium oxide is one of the most remarkable catalysts for water oxidation in such a system with a turnover frequency (TOF) of up to 40 $s^{-1}$ in aqueous solutions[174]. Even though, iridium as one of the most scarce elements on the earth may not be suitable for potential large scale applications.

As a result, extensive efforts have been paid to the first row transition metal catalysts for water oxidation with a particular emphasis on catalysts containing cobalt. Various forms of cobalt compounds ranging from heterogeneous cobalt oxides[175], and CoPi catalysts[114,176] to homogeneous polyoxometalates[158], and complexes[141,177] have shown comparable activities and advantages. Among these, cobalt oxides are of particular interest not only due to their excellent activity and long-term durability but also owing to their tunable sizes and morphologies in the form of nanocube[178], nanorod[179], spheres[180] or mesoporous structure[181], which strongly affect the catalytic activities. For instance, it was found that reducing the particle size of $Co_3O_4$ can efficiently improve the activity for water oxidation[121,123]. This enhancement lies in the

generation of more surface active sites and promotion of charge transfer[121]. To avoid the aggregation but simultaneously minimize the size of cobalt oxides, various supports have been employed including conjugated polymer, silica and aluminum oxide[121]. It was found that cobalt oxide catalysts loaded on these supports display significant enhancement in water oxidation activity compared with the unsupported cobalt oxide nanoparticles, which has inspired us to develop a suitable support to encapsulate cobalt oxides as water oxidation catalysts.

Metal-organic frameworks (MOFs) comprised of metal clusters and bridging organic ligands have emerged as a new class of functional materials for various applications owing to their tunable and uniform pore structure and design flexibility[182-184]. Recently MOFs have been extensively applied as support materials in heterogeneous catalysis. Among them, MIL-101, a highly porous and robust MOF, which possesses two hydrophilic zeotypic cavities with diameters of 29 Å and 34 Å, is a promising candidate for nanoparticle deposition. Henschel et al prepared a hydrogenation catalyst, Pd/MIL-101 by incipient wetness impregnation method to incorporate Pd nanoparticles into MIL-101[185]. Pan et al discovered that Pd@MIL-101 can significantly enhance the catalytic efficiency in one-step synthesis of methyl isobutyl ketones[186]. More recently, Jiang et al developed bimetallic ultrafine PdAg@MIL-101 as multifunctional catalysts for a one-pot cascade reaction[187]. Though various types of metal nanoparticles have been successfully deposited in the interior of MIL-101[188], development of oxide incorporated MOFs has met with limited success with only a few reports in the literature. Fischer and co-workers reported the syntheses of $TiO_2$ and ZnO nanoparticles embedded MOF-5 by gas infiltration of Ti or Zn precursors followed by slow hydrolysis or treatment with dilute $O_2$[189]. In another report, Balu et al prepared $Fe_2O_3$ deposited MIL-101 using a microwave assisted method[190].[191] In view of these, MIL-101 was chosen for deposition of cobalt oxide nanoparticles which are shown as efficient oxygen evolution catalysts. In this report, various concentrations of cobalt oxide nanoparticles are embedded in MIL-101 by a simple and facile method involving impregnation

followed by heat treatment method. The obtained materials have shown great enhancement for photocatalytic water oxidation reaction at optimized reaction conditions compared to bare $Co_3O_4$ and cobalt oxide supported on silica sphere.

## 4.2 Experimental

### 4.2.1 Material and reagents.

Chromium(III) nitrate nonahydrate (99%) was obtained from Acros. Ethanol absolute was purchased from Merck. Dimethylformamide (DMF, ≥ 99.8%), hexane (98.5%), 2-propanol and ammonia solution (25%) were obtained from Fisher. Nitric acid (67-69 wt%) was obtained from Sinopharm Chemical. Terephthalic acid (98+%), aqueous hydrofluoric acid (HF, 46 wt%) and sodium persulfate (98%) were obtained from Alfa Aesar. Ammonium fluoride ($NH_4F$, ≥ 98%), cobalt(II) nitrate tetrahydrate (≥ 98%), cobalt(II) acetate tetrahydrate (≥ 98%), Nafion solution (5%) and tris(2,2'-bipyridyl)dichlororuthenium(II) hexahydrate ($[Ru(bpy)_3]Cl_2 \cdot 6H_2O$, 99.95%) were obtained from Sigma-Aldrich. All chemicals were used without further purification.

### 4.2.2 Material preparation

**Preparation of MIL-101.** MIL-101 was prepared according to the literature method with slight modification[191,192]. Terephthalic acid (1.993 g, 12.0 mmol), $Cr(NO_3)_3 \cdot 9H_2O$ (4.802 g, 12.0 mmol), HF (0.6 mL) and deionized water (84 mL) were added to a 125 mL Teflon-lined autoclave and the mixture was heated at 220 °C for 8 h. After cooling to the room temperature, the resultant solid was isolated by filtration and washed with 150 mL of DMF to remove unreacted terephthalic acid. The green powder was then treated solvothermally with ethanol at 100 °C for 12 h twice. Ion exchange was carried out by dispersing the solid in 150 mL of $NH_4F$ aqueous solution (300 mM) with stirring for 10 h at 70 °C. The green product was collected by filtration and then washed with hot water at around 80 °C several times. The final green powder was dried in vacuum at 150 °C and stored in dry cabinet for further use.

**Loading of cobalt oxide on MIL-101.** A double solvent method was first used to promote the impregnation of $Co^{2+}$ cations into the cavity of MIL-101[187]. Typically, the as-prepared MIL-101 (150 mg, 0.13 mmol) was dispersed in 30 mL of anhydrous hexane by ultrasonication for 15 min followed by stirring vigorously for 20 min. Then, 200 μL of 0.6 M (or 0.2 M, 0.4 M and 0.8 M) cobalt nitrate aqueous solution was added slowly in 20 min using a syringe pump. The mixture was stirred for another 2 h. Then the settled solid was isolated by removing hexane. The obtained product was placed in air overnight and was then dried at 150 °C in air for 3 h. The dried sample named as $[Co(NO_3)_2]_a$/MIL-101 (a = 0.2, 0.4, 0.6 or 0.8) was calcined at 250 °C for 3 h in argon with a flow rate of 20 mL/min followed by heating at 150 °C in static air. The final sample obtained was denoted $Co_x$/MIL-101 (*x* is the weight percentage of cobalt determined by ICP).

**Loading of cobalt oxide on silica nanospheres.** Nonporous silica nanospheres with an average diameter of around 200 nm were prepared according to the literature method[193]. Cobalt oxide was loaded using the method described above except that MIL-101 was replaced by silica nanospheres and the concentration of cobalt nitrate aqueous solution was 0.6 M.

**Preparation of $Co_3O_4$.** $Co_3O_4$ nanoparticles were prepared using a solvothermal method. In a typical synthesis, 200 μL of 0.8 M cobalt acetate aqueous solution, 27 mL of ethanol, 0.675 mL of 25 wt% ammonia aqueous solution and 2 mL of deionized water were mixed in a 100 mL round bottom flask and then kept at 80 °C with stirring for 10 h. The mixture was transferred to a 48 mL Teflon-lined autoclave and heated at 150 °C for 3 h. The obtained product was separated by centrifugation, washed with ethanol and deionized water and dried at 50 °C in vacuum.

### 4.2.3 Photocatalytic activity measurement.

Visible light driven water oxidation reactions were conducted in a closed gas circulation and evacuation system fitted with a top window Pyrex cell. A circulating cooling water system was used to maintain the reactor at room temperature. In a typical reaction, 12.5 mg of the catalyst, 0.05 mmol of $[Ru(bpy)_3]Cl_2$ and 0.375 mmol

of $Na_2S_2O_8$ were added to 50 mL of 10 mM sodium borate buffer solution. The pH was adjusted to 9 by concentrated nitric acid. The light source was a 300 W Xenon lamp with a long-pass cut-off filter ($\lambda > 420$ nm). The evolved oxygen was detected by an online gas chromatography. The $O_2$ yield was calculated after 70 min irradiation according to the following equation. The turnover frequency (TOF) was calculated using the initial rates of $O_2$ evolution during the first 20 min.

$$O_2 \text{ yield} = \frac{\text{moles of evolved } O_2 \times 2}{\text{moles of } Na_2S_2O_8 \text{ added}} \times 100\%$$

$$\text{TOF} = \frac{\text{moles of evolved } O_2}{\text{moles of cobalt} \times \text{reaction time}}$$

**4.2.4 Electrochemistry.**

Electrochemical performance for water oxidation was carried out on a Metrohm Autolab electrochemical workstation with a conventional three-electrode system in 10 mM borate buffer at pH 9. A Pt plate and an Ag/AgCl (3M KCl) were used as the counter electrode and reference electrode, respectively. The working electrode was prepared as following. Firstly, 5 mg of the catalyst was suspended in a mixture of 10 μL of 5 wt% nafion ethanol solution, 250 μL of 2-propanol and 750 μL of deionized water by ultrasonication. Then, 10 μL of the suspension was dropped on the surface of 5 mm carbon glassy rotating disk electrode (RDE) and was placed in air to dry naturally. Prior to the measurement, the electrolyte was bubbled with oxygen until saturation. After that, the sample on the RDE was subjected to potential cycling in the range of 0.2 V to 1.4 V with a scan rate of 100 mV/s for 40 cycles. Cyclic voltammetry (CV) was then recorded at a scan rate of 20 mV/s. Linear sweep voltammetry (LSV) was obtained at a scan rate of 2 mV/s. Tafel plot was obtained using the data obtained from LSV with resistance correction. The electrochemical impedance spectroscopy (ESI) was recorded in the frequency range of 100 kHz to 100 mHz at the potential of 1.1 V. All tests were performed in $O_2$-saturated electrolyte with a rotating rate of 1600 rpm.

**4.2.5 Materials characterization.**

Powder X-ray diffraction (XRD) patterns were recorded on a X-ray diffractometer

(Bruker AXS D8, Cu Kα, λ = 1.5406 Å, 40 kV and 20 mA) in the range of 5°-65°. FT-IR spectra were obtained with a Perkin Elmer FT-IR Spectrum GX using KBr technique in the range of 1800–400cm$^{-1}$.The UV-visible absorption spectra were obtained on a UV-visible spectrophotometer (UV-2450, Shimadzu). An Agilent 7700x Inductively Coupled Plasma (ICP) was used to determine the cobalt contents. Brunauer-Emmett-Teller (BET) surface area was measured by $N_2$ adsorption and desorption at 77 K using a Quantachrome Autosorb-6 sorption system. All samples were degassed at 150 °C for 12 h in vacuum before analysis. Pore size distribution was obtained by Barrett-Joyner-Halenda (BJH) method using the adsorption curve of the isotherm. The total pore volume was estimated by the amount of nitrogen adsorbed at the relative pressure of 0.99. The structural and morphological investigation and elemental mapping were conducted with and transmission electron microscopy (TEM, JEOL, JEM-2100F), attached with energy-dispersive X-ray (EDX) spectroscopy. The X-ray photoelectron spectroscopy (XPS) analysis was carried out on an AXIS-HSi, Kratos Analytical and the binding energy was calibrated using the C 1s peak at 284.7 eV. The Raman spectra were measured on a Renishaw instrument, using a He/Ne laser with a wavelength of 785 nm. The Co K-edge X-ray absorption near edge structure (XANES) spectra were recorded at Singapore Synchrotron Light Source (SSLS) using a beam line with energy of 1.85 GeV. A Si(111) monochromator was used for varying the energy in the desired range. Calibration was performed with a Co foil using the first point of Co inflection.

### 4.3 Results and discussion

Cobalt oxide nanoparticles have been successfully loaded in the cages of MIL-101 by a facile double solvent impregnation and heat treatment method. The resultant $Co_x$/MIL-101 samples have been well characterized by various techniques. Firstly, the actual loading of cobalt (1.4-4.9 wt%) at various precursor concentrations determined by ICP method matches well with the theoretical loading (1.5-5.2 wt%) as shown in Table 4-1, indicating that the double solvent method using water and hexane is effective to impregnate cobalt salt into MIL-101. As shown in Figure 4-1a, the

experimental powder XRD pattern of MIL-101 was in good agreement with the simulated pattern, confirming the purity and good crystallinity of MIL-101. After loading cobalt oxide, it can be observed that the characteristic XRD peaks of MIL-101 (Figure 4-1a) in all the samples are retained, indicating that the crystal structure of MIL-101 is kept intact during the treatment. The lack of detectable signals of cobalt oxide phase should be due to their low contents as well as small particle sizes confined by the pores of MIL-101. The $N_2$ adsorption measurement of MIL-101 shows type I property with secondary uptakes at $P/P_0$ of around 0.1 and 0.2 (Figure 4-1b), suggesting the presence of two monodispersed windows of around 1.6 nm and 2.1 nm based on the pore size distribution profile. The BET surface area of MIL-101 was measured to be 4199 $m^2/g$, which is consistent with the literature reported value.[55] The single point pore volume was estimated to be 2.29 mL/g at a relative pressure of 0.99. After loading of cobalt oxide nanoparticles, the BET surface areas of all the samples are reduced and the extent of the reduction increases with the loading (Table 4-2). The surface area of $Co_{4.9}$/MIL-101 with the highest cobalt loading is reduced to 1459 $m^2/g$. The total pore volume correspondingly decreases from 2.39 to 0.827 mL/g with the increasing loading of cobalt oxides, indicating that cavities are partially blocked by the embedded nanoparticles. On the other hand, the pore size distribution remains the same. These results suggest that the nanoparticles are successfully embedded in the interior of MIL-101.

**Table 4-1** Percentages of cobalt loaded on MIL-101.

| Sample | Precursor concentration (mol/L) | Theoretical percentage (wt%) | Determined percentage (wt%) |
|---|---|---|---|
| $Co_{1.4}$/MIL-101 | 0.2 | 1.5 | 1.4 |
| $Co_{2.6}$/MIL-101 | 0.4 | 2.8 | 2.6 |
| $Co_{3.9}$/MIL-101 | 0.6 | 4.1 | 3.9 |
| $Co_{4.9}$/MIL-101 | 0.8 | 5.2 | 4.9 |

**Table 4-2** BET surface area and pore volume of $Co_x$/MIL-101 samples.

| Sample | BET surface area ($m^2/g$) | Pore volume ($cm^3/g$) |
|---|---|---|
| MIL-101 | 4199 | 2.39 |
| $Co_{1.4}$/MIL-101 | 3821 | 2.08 |
| $Co_{2.6}$/MIL-101 | 3105 | 1.63 |
| $Co_{3.9}$/MIL-101 | 2411 | 1.26 |
| $Co_{4.9}$/MIL-101 | 1459 | 0.83 |

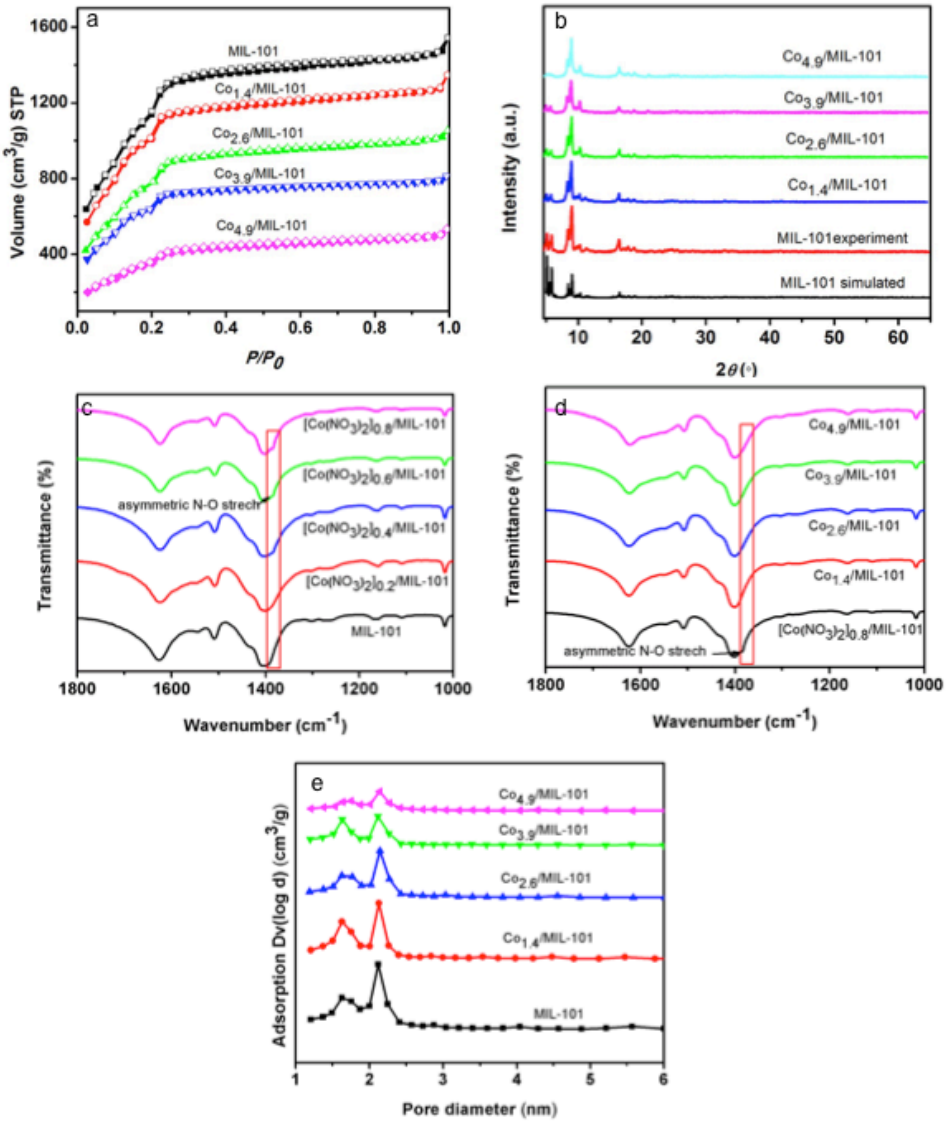


**Figure 4-1** (a) Powder XRD patterns of simulated MIL-101, as-prepared MIL-101, $Co_{1.4}$/MIL-101, $Co_{2.6}$/MIL-101, $Co_{3.9}$/MIL-101 (**1**) and $Co_{4.9}$/MIL-101, and (b) $N_2$ adsorption isotherm activated MIL-101, $Co_{1.4}$/MIL-101, $Co_{2.6}$/MIL-101, $Co_{3.9}$/MIL-101 and $Co_{4.9}$/MIL-101. FTIR spectra of (c) MIL-101,

$[Co(NO_3)_2]_a$/MIL-101 and (d) $[Co(NO_3)_2]_{0.8}$/MIL-101, $Co_x$/MIL-101. (e) $N_2$ adsorption isotherm of activated MIL-101, $Co_{1.4}$/MIL-101, $Co_{2.6}$/MIL-101, $Co_{3.9}$/MIL-101 (**1**) and $Co_{4.9}$/MIL-101.

XPS and XANES were then employed to determine the chemical and phase compositions of the embedded nanoparticles in the MOF taking the $Co_{3.9}$/MIL-101 (**1**) as the example. The high-resolution XPS spectrum of Co 2p is shown in Figure 4-2a. The two peaks at 779.4 eV and 781.5 eV can be assigned to Co $2p_{3/2}$ in $Co_3O_4$ and divalent $Co^{2+}$ in other species, respectively[194,195]. Though the peak for $Co_3O_4$ is dominant, the characteristic shake-up satellite also indicates the presence of Co(II) compounds. XANES was applied to further investigate the types cobalt species present in the sample. The Co K-edge XANES spectrum of **1** is shown in Figure 4-2b together with the relevant cobalt standards. A linear combination method was used to fit all possible compositions of cobalt species in **1** using the above standards. The best fitting result obtained for **1** is shown in Figure 4-2c. It was found that cobalt species in **1** are comprised of $Co_3O_4$, $Co(NO_3)_2$ and $Co(OH)_2$ with a molar ratio of 77:17:6, which is consistent with the finding from XPS. Raman spectrum of **1** was investigated to further confirm the composition. For comparison, the spectrum of bulk $Co_3O_4$ was also studied. As shown in Figure 4-2d, the three characteristic peaks at 868, 810 and 629 $cm^{-1}$ are ascribed to MIL-101. Four additional weak peaks at 681, 606, 479 and 457 $cm^{-1}$ are observed in the spectrum of **1**. Compared to the characteristic $A_{1g}$, $F_{2g}$, $F_{2g}$ and $E_g$ phonon modes of $Co_3O_4$ centered at 691, 619, 522 and 481 $cm^{-1}$, these four peaks are blue shifted and broadened. To the best of our knowledge, nanoparticles of smaller sizes and of better dispersion exhibit blue shift in Raman spectrum at high laser power due to thermal effect[196], which may well support the current observation made. The XANES fitting results, coupled with XPS and Raman results indicate that the majority of $Co(NO_3)_2$ impregnated in the mesopores of MIL-101 has been

converted to $Co_3O_4$ after heat treatment. As a relatively mild condition ($\leq 250\ ^oC$) was applied during heat treatment in order not to affect the structure of the MOF, it is not surprised that a certain percentage of $Co(NO_3)_2$ is still retained or partially converted to $Co(OH)_2$ by hydrolysis in the presence of moisture. Furthermore, compared with the FTIR spectra of $[Co(NO_3)_2]_a$/MIL-101 before heat treatment, the spectra of $Co_x$/MIL-101 samples do not display distinguishable absorption at 1385 $cm^{-1}$ associated with $\nu_3$ vibrational mode of $NO_3^-$ (Figure 4-1c&d), which further confirms the decomposition of the majority of $Co(NO_3)_2$ to form cobalt oxide[197].

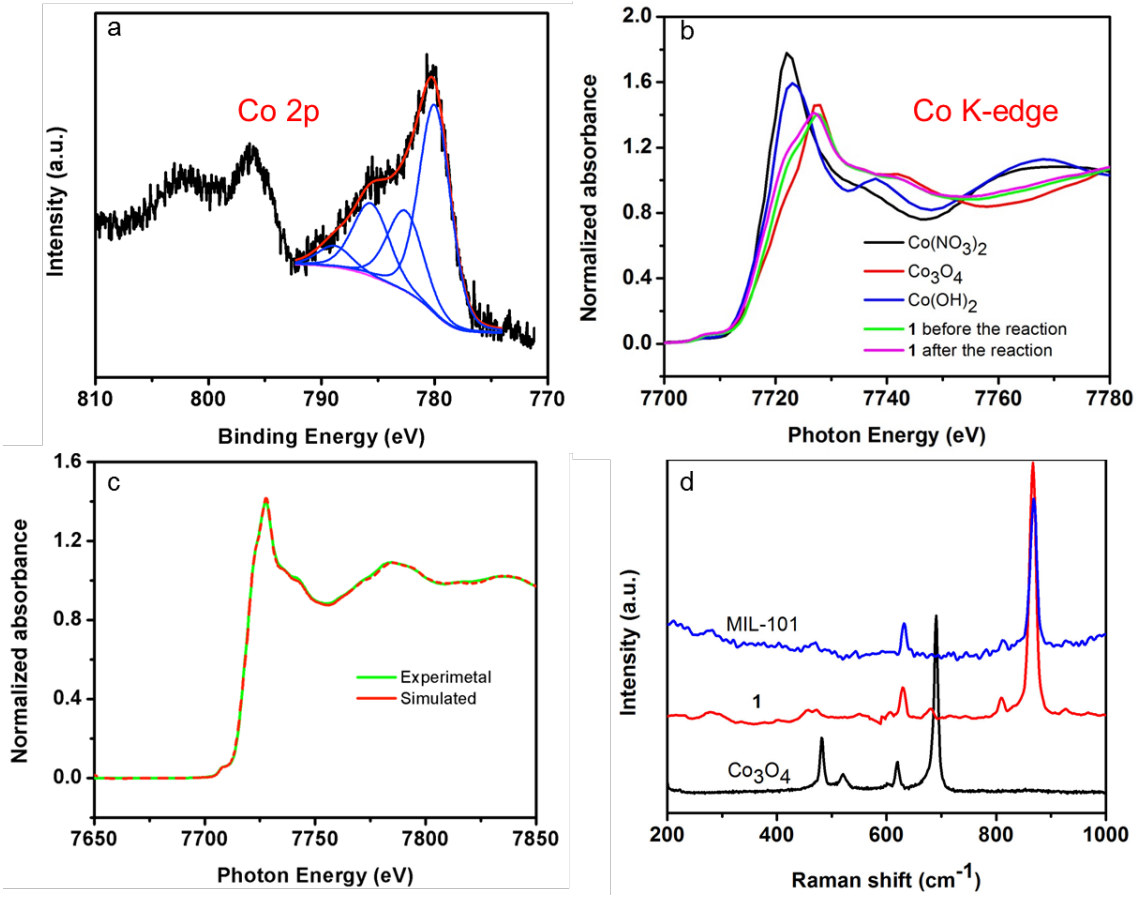


**Figure 4-2** (a) XPS spectrum of Co 2p of **1,** (b) XANES spectra of **1** ($Co_{3.9}$/MIL-101) before and after the photocatalytic reaction, $Co(OH)_2$, $Co_3O_4$ and $Co(NO_3)_2$, (c) the experimental and simulated XANES spectra of **1**, and (d) Raman spectra of bare MIL-101, **1** and $Co_3O_4$.

The location and distribution of cobalt oxide nanoparticles were examined by TEM, bright field TEM and elemental mapping analyses. Figure 4-3a shows the typical

octahedral morphology of MIL-101 with a smooth surface. After loading of cobalt oxide, it is seen that nanoparticles of are uniformly distributed in MIL-101 for **1**. No particles on the external surface of MIL-101 can be easily distinguished. The EDX result of **1** confirms the existence of cobalt in MIL-101 with a weight percentage of around 3.3% which is consistent with that determined by ICP. The good dispersion of cobalt oxide nanoparticles in MIL-101 is further evidenced from elemental mapping results. As shown in Figure 4-3e-f, together with chromium, the cobalt element is uniformly distributed in the area of the particle examined. The size and distribution of cobalt oxide nanoparticles in the other three samples are presented in Figure 4-3g-i. Nanoparticles with a narrow size distribution and good dispersion can be clearly observed in all the samples. As there is only a small atomic weight difference between Cr and Co, it is challenging to determine the size of cobalt oxide nanoparticles exactly. Based on the above XRD, $N_2$ adsorption, TEM and elemental mapping results, it can be concluded that cobalt oxide nanoparticles are successfully embedded in the cages of MIL-101. Hence the size of cobalt oxide nanoparticles should be around 2-3 nm as restricted by the cavity size of MIL-101. Such ultra small cobalt oxide nanoparticles are expected to display excellent activity for water oxidation.

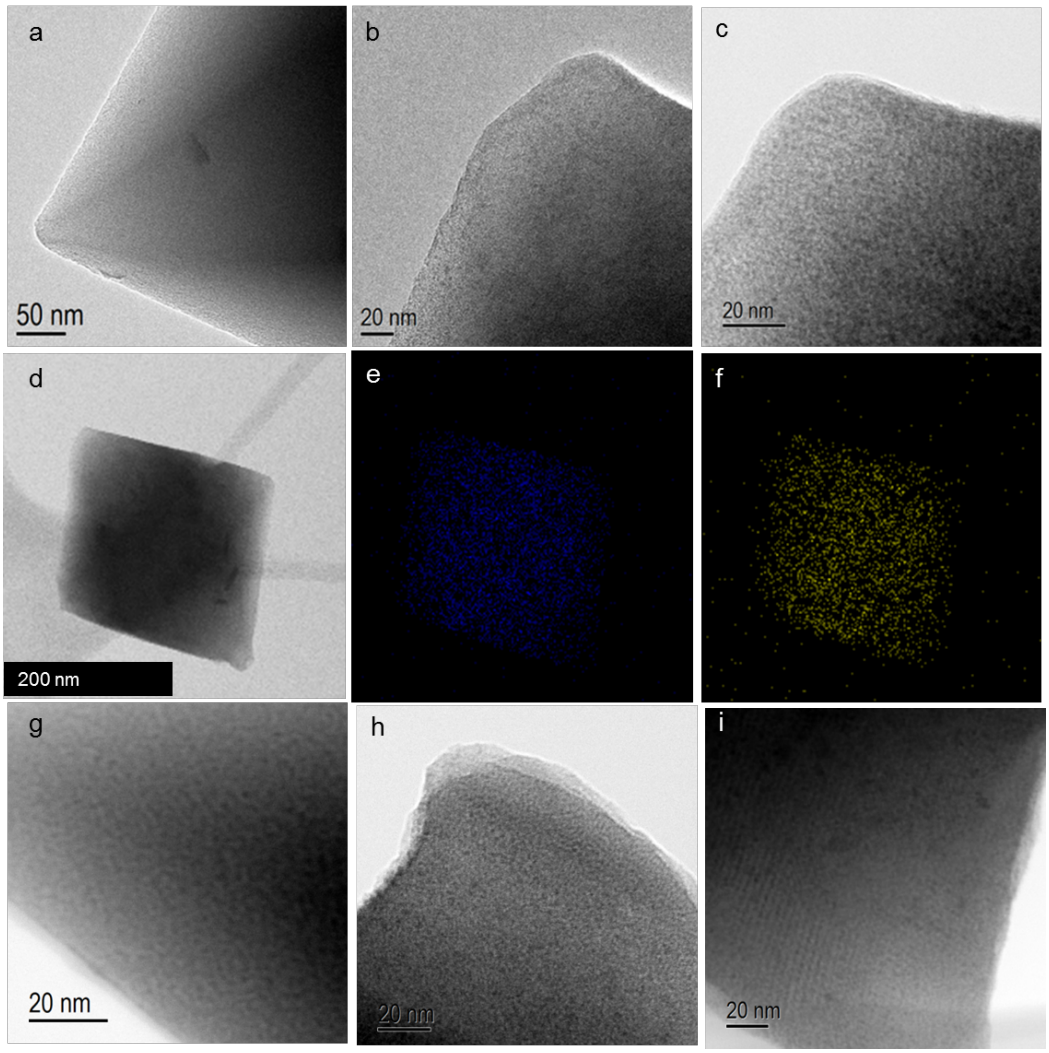


**Figure 4-3** TEM images of MIL-101 (a) and **1** ($Co_{3.9}$/MIL-101) (b, d), bright filed TEM image of **1** (c), $Co_{1.4}$/MIL-101 (g), $Co_{2.6}$/MIL-101 (h) and $Co_{4.9}$/MIL-101 (i) and EDX elemental mapping results of Cr (e) and Co (f).

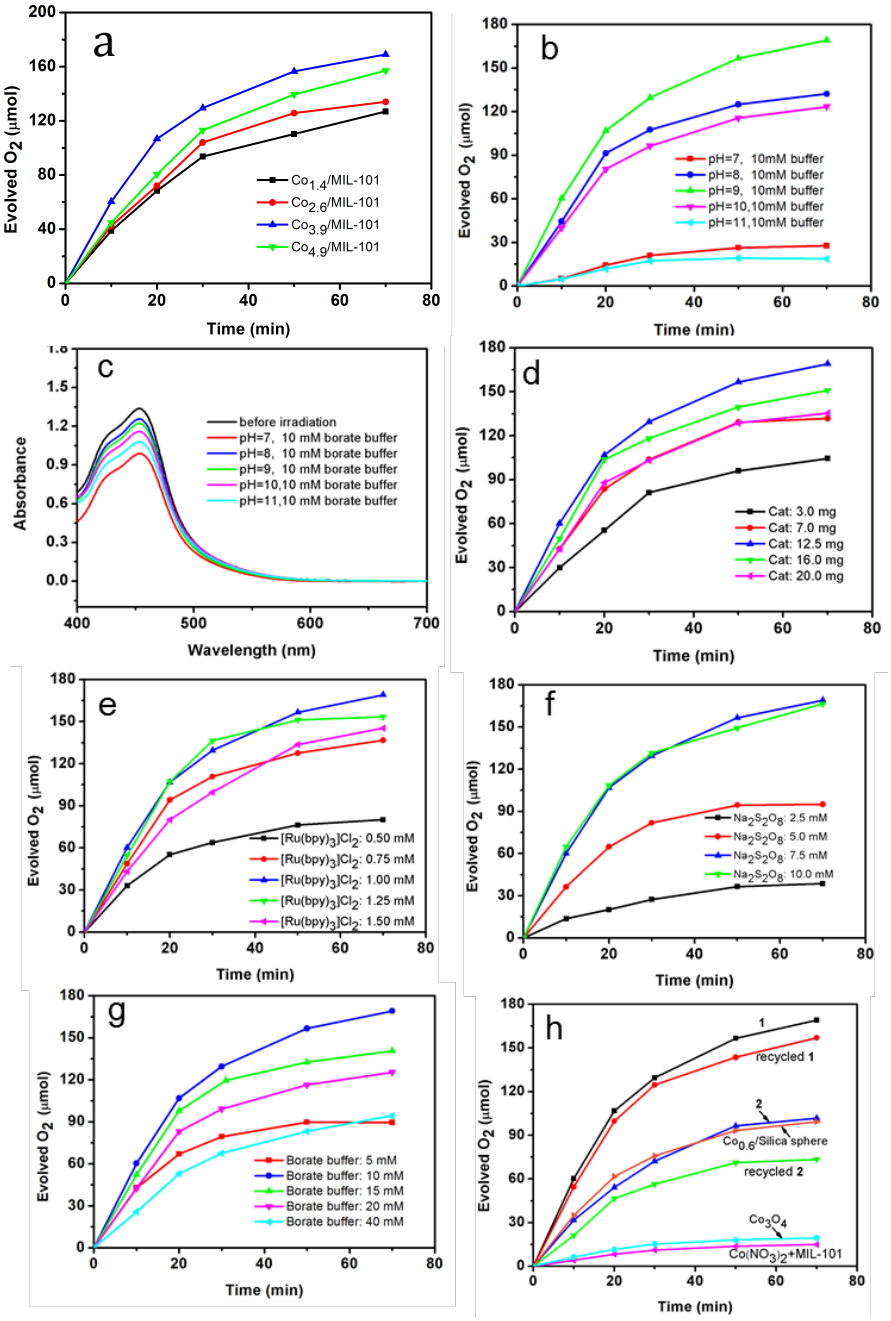


**Figure 4-4** (a) Time course of $O_2$ evolution over $Co_{1.4}$/MIL-101, $Co_{2.6}$/MIL-101, $Co_{3.9}$/MIL-101 and $Co_{4.9}$/MIL-101 as the catalysts. (b) Time course of $O_2$ evolution with different initial pH values. (c) UV-vis spectra of the supernatant solutions after reaction for 70 min at different pH. The solutions were diluted to one tenth for analysis. (d) Time course of $O_2$ evolution over different amount of **1** as the catalysts. (e) Time course of $O_2$ evolution at different concentration of $[Ru(bpy)_3]Cl_2$. (f) Time course of $O_2$ evolution at different concentration of $Na_2S_2O_8$. (g) Time course of $O_2$ evolution at different concentration of borate buffer. (h) Time course of $O_2$ evolution

over **1**, recycled **1**, **2** ($[Co(NO_3)_2]_{0.6}$/MIL-101), recycled **2**, $Co_3O_4$ (6 nm), $Co_{3.7}/SiO_2$ and the mixture of cobalt nitrate and MIL-101 with an equivalent amount of leached $Co^{2+}$ in **1**. Reaction condition: 12.5 mg of **1**, 7.5 mM of $Na_2S_2O_8$, 1.0 mM of $[Ru(bpy)_3]Cl_2$ in 50 mL of 10 mM borate buffer, 300 W Xenon lamp, $\lambda > 420$ nm.

The $Co_x$/MIL-101 samples were evaluated for photocatalytic water oxidation using the $[Ru(bpy)_3]^{2+}$–$Na_2S_2O_8$ system in borate buffer aqueous solutions driven by visible light ($\lambda > 420$ nm). As shown in Figure 4-4a and Table 4-3, under the same conditions, both the initial rate and final yield of oxygen evolution increase with the cobalt content till 3.9% (**1**) as the optimum loading. The reaction conditions including pH, and the concentrations of the catalyst, $[Ru(bpy)_3]Cl_2$ photosensitizer, $Na_2S_2O_8$ electron acceptor and buffer have been optimized (Figure 4-4d-g). It is known that in the $[Ru(bpy)_3]^{2+}$–$Na_2S_2O_8$ system, water oxidation is highly dependent on pH. As shown in Figure 4a, the highest $O_2$ evolving rate is obtained at pH 9. At either lower or higher pH values, the activity is dropped remarkably. It is understood that $[Ru(bpy)_3]^{3+}$ is the real oxidant thermodynamically favorable for oxidizing water to $O_2$ in such a system. The $[Ru(bpy)_3]^{3+}$ species is generated by oxidative quenching of the excited $[Ru(bpy)_3]^{2+}$* triplet state. At higher pH, the reduction of $[Ru(bpy)_3]^{3+}$ is accelerated, resulting in the enhancement of water oxidation rate. However, a spontaneous reduction of $[Ru(bpy)_3]^{3+}$ to $[Ru(bpy)_3]^{2+}$ at higher pH is accompanied with decomposition of the photosensitizer by oxidation of the bipyridine ligand[198]. It is evidenced from the UV-vis absorption spectra (Figure 4-4c) of the reaction supernatant solution that the characteristic metal-to-ligand charge transfer (MLCT) band of $[Ru(bpy)_3]^{2+}$ at 452 nm is decreased by 14% (pH 10) and 20% (pH 11), respectively. When pH was lower than 9, the low activity could be partially attributed to the low buffering capacity. For instance, the pH of the solution after the reaction was measured to be 2.2 with an initial pH of 7.

**Table 4-3** Summary of the photocatalytic oxygen evolution performances of catalysts investigated in this work.

| Sample | Reaction condition | Initial rate (μmol/min) | TOF($s^{-1}$ per Co atom)×$10^3$ | $O_2$ yield (%) | Reference |
|---|---|---|---|---|---|
| **$Co_{1.4}$/MIL-101** | a | 3.24 | 18.2 | 68 | This work |
| **$Co_{2.6}$/MIL-101** | a | 4.33 | 13.1 | 71 | This work |
| **1** | a | 6.05 | 12.2 | 88 | This work |
| **$Co_{4.9}$/MIL-101** | a | 4.05 | 6.5 | 82 | This work |
| **$Co_{3.7}/SiO_2$** | a | 3.48 | 7.4 | 53 | This work |
| **$Co_3O_4$ (6 nm)** | b | 0.64 | 1.3 | 12 | This work |
| **2** | a | 3.17 | 6.4 | 54 | This work |
| **$Co_3O_4$/KIT-6 (3.8%)** | c | - | 0.41 | 71 | 121 |
| **$Co_3O_4$/SBA-15 (4.0%)** | c | - | 0.34 | 63 | 121 |
| **$Co_3O_4/Al_2O_3$ (4.0%)** | c | - | 0.46 | 84 | 121 |
| **$Co_3O_4$ (6 nm)** | c | - | 0.25 | 47 | 121 |
| **$Co_3O_4$** | d | - | 0.24 | - | 123 |
| **$Co_3O_4$/SBA-15 (4.0%)** | e | - | 0.64 | - | 123 |

[a]12.5 mg of catalysts, 7.5 mM of $Na_2S_2O_8$, 1.0 mM of $[Ru(bpy)_3]Cl_2$ in 50 mL of 10.0 mM borate buffer, pH = 9, 300 W Xenon lamp, $\lambda > 420$ nm.

[b]0.66 mg of catalysts, 7.5 mM of $Na_2S_2O_8$, 1.0 mM of $[Ru(bpy)_3]Cl_2$ in 50 mL of 10.0 mM borate buffer, pH = 9, 300 W Xenon lamp, $\lambda > 420$ nm.

[c]75 mg catalyst, 1.67 mM $[Ru(bpy)_3]Cl_2$, 13.5 mM $Na_2S_2O_8$, 68.5 mM $Na_2SO_4$, $Na_2SiF^{6-}$, $NaHCO_3$ buffer, pH = 5.8, 300 W Xe lamp,$\lambda$>400 nm.

[d]10 mg catalyst, 1.5 mM $[Ru(bpy)_3]Cl_2$, 13.5 mM $Na_2S_2O_8$, 68.5 mM $Na_2SO_4$, $Na_2SiF_6$−$NaHCO_3$ buffer, pH = 5.8, 300 W Xe lamp, $\lambda$>400 nm.

[e]200 mg catalyst, 1.5 mM $[Ru(bpy)_3]Cl_2$, 13.5 mM $Na_2S_2O_8$, 68.5 mM $Na_2SO_4$,

$Na_2SiF_6$–$NaHCO_3$ buffer, pH = 5.8, 240 mW emission line (476nm) of an Ar ion laser.

Under the optimized conditions, the amount of oxygen evolved increases approximately linearly for the first 20 min before gradually leveling off for **1** (Figure 4-4h). The TOF of **1** based on the reaction rate in the first 20 min and the oxygen yield after 70 min were calculated to be $1.2\times10^{-2}$ $s^{-1}$ per cobalt atom and 88%, respectively. These values are remarkably higher than those of the control $Co_3O_4$ nanoparticles (6 nm) at $1.3\times10^{-3}$ $s^{-1}$ for TOF and 12% for oxygen yield (Table 4-3). At the lowest cobalt loading, a highest TOF of $1.8\times10^{-2}$ $s^{-1}$ can be obtained for sample $Co_{1.4}$/MIL-101 with a reasonably high yield of 68%. On the other hand, at the highest loading of 4.9%, a high yield of 82% is maintained although the TOF is decreased to $1.2\times10^{-2}$ $s^{-1}$ per cobalt atom.

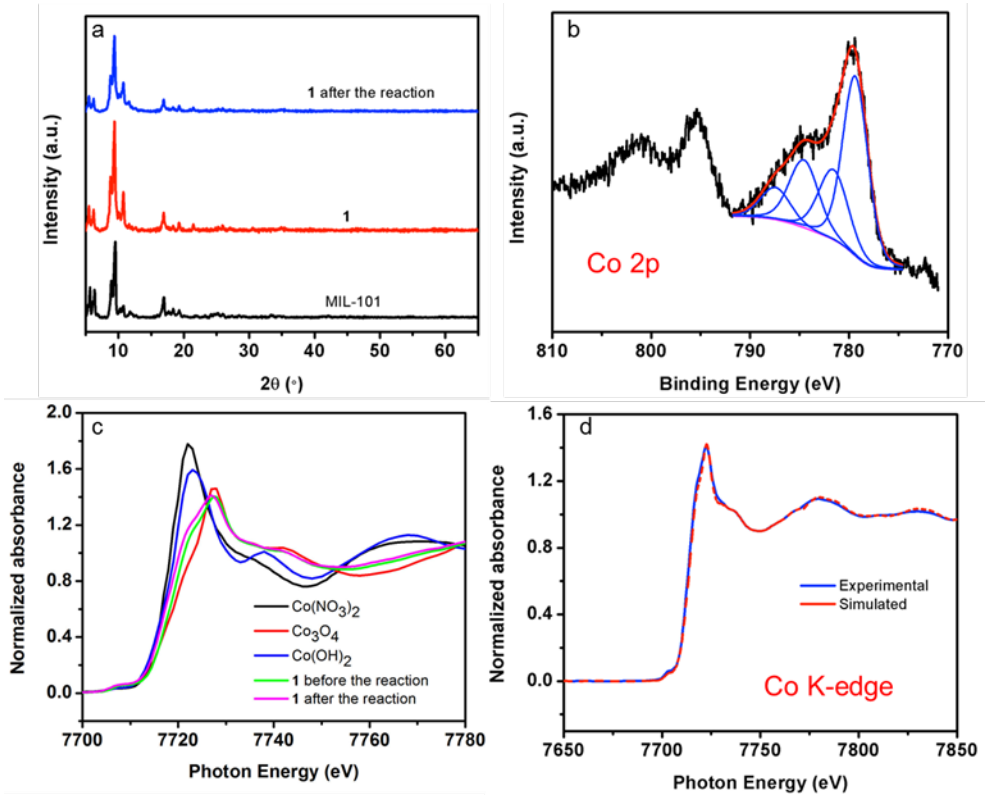


**Figure 4-5** (a) Powder XRD patterns of bare MIL-101, **1** and **1** after the photocatalytic reaction, (b) Co 2p XPS spectrum of **1** after the photocatalytic reaction, (c) XANES spectra **1** after the reaction and reference $Co(OH)_2$, $Co_3O_4$ and $Co(NO_3)_2$,

and (d) the experimental and simulated XANES spectra of **1** after photocatalytic reaction.

In order to probe the stability of **1**, after recovering the catalyst by centrifugation and washing, the catalyst was re-dispersed in a fresh reaction solution. Figure 4-4h shows that there is no significant drop in activity with 90% of the activity retained in the second run. Furthermore, the XRD pattern of the recovered **1** remains consistent with that of MIL-101 (Figure 4-5a), which indicates the framework of MIL-101 remains intact after the photoreaction. XANES and XPS spectra for the recovered **1** also signify that cobalt oxide remains embedded in the MOF (Figure 4-5b-d). On the other hand, when the sample $[Co(NO_3)_2]_{0.6}$/MIL-101 (**2**) before heat treatment was examined for photocatalytic water oxidation under the same condition, several different observations can be made. Firstly, the sample displays a much lower activity (oxygen yield: 54% and TOF: $6.4\times10^{-3}$ $s^{-1}$ per cobalt atom). In addition, it is less stable with its TOF dropped 33% in the second run. The supernatant solutions of **1** and **2** after the first photoreaction run were analyzed with ICP to detect the leached cobalt species. Only a trace amount of cobalt was detected for **1** which accounts for 5% of the cobalt loaded, while 40% percent of cobalt has been leached for **2**. To further exclude the activity of **1** from the leached cobalt cations, a mixture of an equivalent amount of leached $Co^{2+}$ in **1** and 12.5 mg of MIL-101 was used for photocatalytic water oxidation under the same condition (Figure 4-4h). It was found that only a very low $O_2$ yield of 8% can be obtained, confirming that the trace amount of the leached cobalt species should not be responsible for the high activity of **1**.

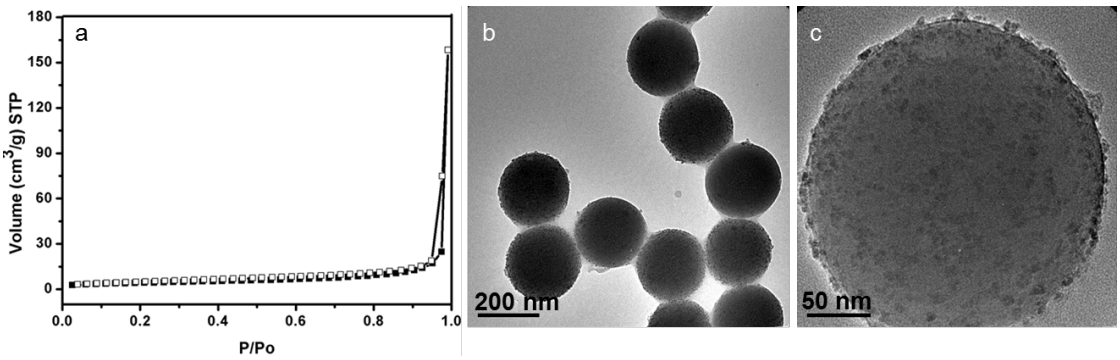


**Figure 4-6** (a) $N_2$ adsorption isotherm of $SiO_2$ nanosphere. The BET surface area of $SiO_2$ nanosphere was determined to be 14.2 $m^2/g$. (b,c) TEM images of $Co_{3.7}/SiO_2$.

To further explore the effect of the support on the activity, nonporous $SiO_2$ nanosphere (200 nm) was also investigated as the support. Cobalt oxide was loaded on silica nanospheres using the same method as that on MIL-101. The $N_2$ adsorption isotherm of $SiO_2$ shown in Figure 4-6a confirms a nonporous feature of the material and the surface area was determined to be 14.2 $m^2/g$. As shown in Figure 4-6b-c, cobalt oxide nanoparticles of 5-10 nm are dispersed on the surface of $SiO_2$ nanospheres and some aggregation can be observed. The actual loading of cobalt on $SiO_2$ nanospheres is 3.7 wt% as determined by ICP analysis. As shown in Figre 4-4h, $Co_{3.7}/SiO_2$ also displays a relatively high activity for water oxidation compared to the bare $Co_3O_4$ (6 nm). However, both the oxygen yield (53%) and TOF ($0.74\times10^{-2}$ $s^{-1}$) of $Co_{3.7}/SiO_2$ are significantly lower than those of **1** with a similar cobalt loading. The enhancement in activity should be largely due to the narrow size and good dispersion of cobalt oxide nanoparticles in the well-defined pore structure of the MOF. In addition, the activity of **1** is apparently higher than some reported values of $Co_3O_4$ based photocatalytic water oxidation systems (Table 4-3) due to the smaller particle sizes and more exposed surface active sites. However, a direct comparison of the activity data may not be very meaningful since different reaction conditions were adopted in different groups. On the basis of above observations, it can be concluded that the nanocluster of cobalt oxide embedded in MIL-101 affords an efficient and stable water oxidation under visible light in the $[Ru(bpy)_3]^{2+}$–$Na_2S_2O_8$ system.

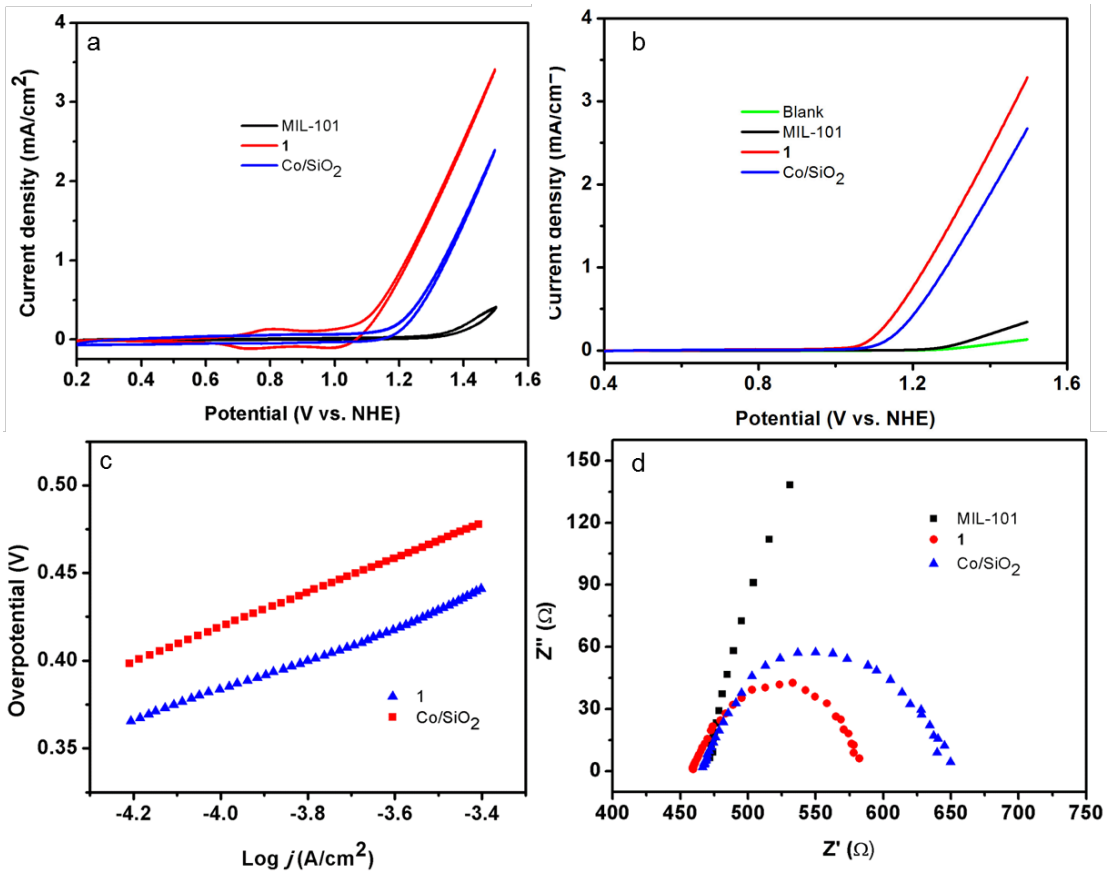


**Figure 4-7** (a) Cyclic voltammetry (CV) curves of MIL-101, **1** and $Co_{3.7}/SiO_2$ at a scan rate of 20 mV/s, (b) linear sweep voltammetry (LSV) curves of MIL-101, **1**, $Co_{3.7}/SiO_2$ and without catalyst at a scan rate of 2 mV/s, (c) Tafel plots of **1** and $Co_{3.7}/SiO_2$ obtained from LSV curves, and (d) Nyquist plots of MIL-101, **1** and $Co_{3.7}/SiO_2$. All tests were performed in $O_2$-saturated electrolyte (borate buffer, pH = 9) with a rotating rate of 1600 rpm.

The electrochemical catalytic water oxidation performance of 1 in 10 mM borate buffer (pH = 9) was also investigated. The CV curves of the 1st and 40th cycle at a scan rate of 100 mV/s in the range of 0.2 to 1.5 V vs. NHE are nearly the same indicating that 1 is stable in borate buffer solution. The CV curve of 1 at a scan rate of 20 mV/s is shown in Figure 4-7a. An oxidation wave associated with Co(II) to Co(III) transformation appears at $E_p$ of 0.81 V followed by the onset potential at 1.0 V[199]. The overpotential of 1 is estimated to be 473 mV at the current density of 1 mA/cm$^2$ from the LSV curve (Figure 4-7b). For comparison, $Co_{3.7}/SiO_2$ shows a similar LSV curve but with a lower current density and higher overpotential (519 mV). Furthermore, Tafel slope of 1 at pH 9 in borate buffer was calculated to be 90 mV, which is slightly

smaller than that of $Co_{3.7}/SiO_2$ (98 mV) (Figure 4-7c). Electrochemical impedance spectroscopy (EIS) was used to evaluate the kinetics of charge transfer. The Nyquist plots obtained in the frequency range of 100 kHz-100 mHz at the potential of 1.1 V for 1, $Co_{3.7}/SiO_2$ and bare MIL-101 are displayed in Figure 4-7d. Arcs in the Nyquist plot are related to charge transfer resistance ($R_{ct}$), which exists at all the interfaces of electrode and electrolyte[200]. Though the bare MIL-101 has a large charge transfer resistance with a fitted $R_{ct}$ value of 1283 Ω, the $R_{ct}$ value dramatically decreases to 68 Ω for 1 by loading of cobalt oxide nanoparticles. A larger $R_{ct}$ value of 102 Ω was measured for $Co_{3.7}/SiO_2$. Thus, it can be concluded that MIL-101 as a substrate not only confines the particle size of the catalyst but may also promote charge transfer through favorable interactions among the catalyst, framework and electrolyte, although the exact mechanism is to be further investigated. The electrochemical behavior of **1** under neutral pH was also studied in 100 mM phosphate buffer (pH=7). The CV curves of **1** before and after 40 continuous cycles remain the same demonstrating that 1 is also stable in the phosphate buffer under neutral pH (Fig.S20). Tafel slope under the neutral condition is estimated to be 102 mV per decade indicating that 1 is less efficient at the neutral pH compared with alkaline conditions. The overpotential at the current density of 1 $mA/cm^2$ determined according to the LSV curve is 490 mV. This value is much higher than that of iridium oxides[38] ($\eta$=250 mV) while is comparable to the literature reported value of $Co_3O_4$[39] ($\eta$=480 mV).

### 4.4 Conclusions

In conclusion, cobalt oxide nanoparticles have been successfully embedded into the zeotypic giant cavities of MIL-101 by a facile impregnation and heat treatment method. The incorporated nanoparticles of 2-3 nm display an excellent dispersion and narrowed size distribution. The apertures of the MOF, which is smaller than the size of cobalt oxide nanoparticles, prevent the nanoparticles form aggregation and leaching. This combination induces great enhancement in photocatalytic water oxidation activity with a high TOF of 0.012 $s^{-1}$ per cobalt atom, which is more than 9 fold compared with that of the unsupported $Co_3O_4$ nanoparticles. Moreover, MIL-101

also plays the role of promoting charge transfer as evidenced by the Nyquist plots. This study suggests that MIL-101 as a chemically stable MOF is a promising support for encapsulation of catalyst nanoparticles for photocatalytic applications.

# CHAPTER 5 POLYOXOMETALATES IMMOBLIZED ON MIL-101(Cr) AS EFFICENT CATALYST FOR WATER OXIDATION

## 5.1 Introduction

The water oxidation half reaction is essential in solar fuel production since water is known to be the only abundant source that can provide the protons and electrons at large scale[10,114]. However, the oxidation of water to form molecular oxygen is a complicated process because it is required to overcome high activation energy to remove four electrons and four protons from two water molecules[172]. For these reasons, improvement of the efficiency of water oxidation catalysts (WOCs) remains to be challenging despite the considerable achievements in recent years.

Interestingly, a series of homogeneous molecular WOCs comprised of earth abundant elements are found to be highly effective catalysts for water oxidation with a particular emphasis on polyoxometalates (POMs)[151-157,201]. The POMs serving as WOCs can undergo fast and reversible mulitelectron-transfer redox transformation without significant structural alteration. Their oxygen-enriched surfaces can provide robust all-inorganic systems to encapsulate and protect active WOCs. A recent remarkable discovery in this filed is the report of $[Co(H_2O)_2(PW_9O_{34})_2]^{10-}$ (CoPOM) by Hill and co-workers[158], which exhibits a high turnover frequency (TOF) of more than 5 $s^{-1}$ at pH 8 when using $Ru(bpy)_3^{3+}$ as the oxidant. A subsequent work by Lian and Hill also investigated the photocatalytic performance of CoPOM using the $Ru(bpy)_3^{2+}$ as the photosensitizer and $Na_2S_2O_8$ as the sacrificial reagent[147]. A turnover number of 220 was obtained, which is even superior than the precious metal based POM $[\{Ru_4O_4(OH)_2(H_2O)_4\}(\gamma\text{-}SiW_{10}O_{36})_2]^{10-}$.[156]

Despite the aforementioned advantages of CoPOM, its stability as well as the nature of the active species has become a bone of contention. Some derivatives from CoPOM were suspected to be the dominant WOCs under the reaction conditions

applied[202-204]. More recently, Hill and co-workers have confirmed that CoPOM is the dominant catalyst though some derivatives are generated. Since CoPOM as a homogeneous catalyst is difficult to be recycled, some efforts have been devoted to the development of POM immobilized solid catalysts. For example, Xie and co-workers recently reported the use of mesoporous carbon nitride ($C_3N_4$) to immobilize CoPOM for electrocatalytic water oxidation with a TOF of 0.3 $s^{-1}$. The mesoporous structure of $C_3N_4$ can not only enhance the catalytic activity of CoPOM, but also offer a method for the stacking of catalytic sites per projected geometrical area to fully utilize the solar flux[161]. It is worthwhile to investigate other materials to identify suitable supports so that the catalytic performances and stability of these polyoxometalate catalysts can be enhanced.

As a new class of hybrid porous materials, metal-organic frameworks (MOFs) are recognized as promising candidates for encapsulating functional species inside the cavities to facilitate the heterogeneous catalytic action. Despite the numerous MOF structures discovered, only a few have been reported with applications by incorporation of POMs[191,205-208]. MIL-101, a well-recognized robust MOF which possesses two hydrophilic zeotypic cavities with diameters of 29 Å and 34 Å, have been used to encapsulate POMs. The coordinatively unsaturated site of MIL-101 allows for binding of inorganic ligands in POM anions. The MIL-101 encapsulated POMs have been exploited for various reactions such as alkene oxidation[19], Knoevenagel condensation[19], esterification[20], Baeyer condensation[21], CO oxidation[22] and hydrogenation of toluene[23]. Herein, we immobilized CoPOM inside MIL-101 to realize photocatalytic and electrocatalytic water oxidation. Not only the catalyst can be recycled, the activity of CoPOM is enhanced due to the favorable interaction between CoPOM and the MIL-101 framework.

## 5.2 Experimental

### 5.2.1 Material and reagents

Sodium tungstate oxide dihydrate (≥ 99%), chromium(III) nitrate nonahydrate (≥ 99%) were purchased from Acros. Dimethylformamide (DMF, ≥ 99.8%) was obtained from Fisher. Terephthalic acid (≥ 98%), aqueous hydrofluoric acid (HF, 46 wt%), disodium hydrogenphosphate (≥ 99%), silver nitrate (≥ 99%) and sodium persulfate (98%) were obtained from Alfa Aesar. Ammonium fluoride (≥ 98%), cobalt(II) nitrate tetrahydrate (≥ 98%), tetra-n-heptylammonium bromide (≥ 99%) and tris(2,2'-bipyridyl)dichlororuthenium(II) hexahydrate ($[Ru(bpy)_3]Cl_2 \cdot 6H_2O$, 99.95%) were obtained from Sigma-Aldrich. All chemicals were used without further purification

### 5.2.2 Preparation of materials

**Preparation of MIL-101.** MIL-101 was prepared according to the literature method with slight modifications[191,192]. Terephthalic acid (1.993 g, 12.0 mmol), $Cr(NO_3)_3 \cdot 9H_2O$ (4.802 g, 12.0 mmol), HF (0.6 mL) and deionized water (84 mL) were added to a 125 mL Teflon-lined autoclave and the mixture was heated at 220 °C for 8 h. After cooling to the room temperature, the resultant solid was isolated by filtration and then washed in 150 mL of DMF to remove unreacted terephthalic acid. The green powder was then treated solvothermally with ethanol at 100 °C for 12 h twice. Ion exchange was carried out by dispersing the solid in 150 mL of $NH_4F$ aqueous solution (300 mM) with stirring for 10 h at 70 °C. The green product was collected by filtration and washed with hot water at around 80 °C several times. The final green powder was dried in vacuum at 150 °C and stored in dry condition for further use.

**Synthesis of $Na_{10}[Co_4(H_2O)_2(PW_9O_{34})_2]$ (CoPOM).** CoPOM was synthesized according to the literature method[158]. In a typical synthesis, $Na_2WO_4 \cdot 2H_2O$ (17.81 g, 54 mmol), $Na_2HPO_4 \cdot 7H_2O$ (1.61 g, 6 mmol) and $Co(NO_3)_2 \cdot 6H_2O$ (3.49 g, 12 mmol) were mixed in 50 mL of deionized water. The pH of the mixture was adjusted to 7.0 using hydrochloric acid solution. The resultant purple suspension was refluxed at 100 $^oC$ for 2 h. The solution was then saturated with NaCl and allowed to cool to room

temperature. The resulting purple crystals were collected, quickly washed with approximately 15 mL of deionized water and recrystallized from hot water.

**Immobilizing CoPOM on MIL-101.** CoPOM was immobilized on MIL-101 by an ion exchange method with $F^-$ anions in MIL-101 replaced by CoPOM anions. The exchange condition was optimized. In a typical reaction, 250 mg of MIL-101 was suspended in 50 mL of CoPOM (450 μM) aqueous solution by ultrasonication for 20 min. The mixture was then stirred at 100 °C for 12 h. After that, the solid was collected by centrifugation and washed with deionized water for several times until the UV signal belonging to CoPOM in the supernatant was not observed. The obtained solid was dried at 50 °C in vacuum.

**Stability study of CoPOM/MIL-101 and CoPOM.** The stability of CoPOM/MIL-101 and CoPOM were investigated using a two-step process to measure the concentration of cobalt in the solution after the photoreaction. The tetra-n-heptylammonium nitrate ($THpANO_3$) toluene solution was prepared by a reaction of tetra-n-heptylammonium bromide (THpABr) with $AgNO_3$. In a typical reaction, 20 mL of 0.025 M $AgNO_3$ aqueous solution was added to 40 mL of 0.0125 M THpABr toluene solution. The resulting mixture was shaken vigorously and AgBr was precipitated form the mixture. The upper organic layer was then isolated after the mixture was left to stand for some time. The $THpANO_3$ toluene solution with a concentration of 0.0125 M was used to extract CoPOM anions from the reaction solution, which was collected after the photoreaction and centrifuged to isolate the dispersed catalysts. The latter was kept for further analysis. Then 10 mL of the above prepared THpANO3 toluene solution was added to 10 mL of the supernatant of the reaction solution. The resulting mixture was shaken vigorously and then left to stand until the organic layer and aqueous layer were separated. The lower aqueous layer was collected for Inductively Coupled Plasma (ICP) analysis.

### 5.2.3 Photocatalytic activity measurement

Visible light driven water oxidation reactions were conducted in a closed gas circulation and evacuation system fitted with a top window Pyrex cell. A circulating cooling water system was used to maintain the reactor at room temperature. In a typical reaction, 12.5 mg of the catalyst, 0.05 mmol of $[Ru(bpy)_3]Cl_2$ and 0.375 mmol of $Na_2S_2O_8$ were added to 50 mL of 10 mM sodium borate buffer solution. The pH was adjusted to 9.0 by concentrated nitric acid. The light source used was a 300 W xenon lamp with a long-pass cut-off filter ($\lambda > 420$ nm). The evolved oxygen gas was detected by an online gas chromatography (Agilent 6890N). The $O_2$ yield was calculated after 70 min irradiation according to the following equations. The turnover frequency (TOF) was calculated using the initial rates of $O_2$ evolution during the first 10 min.

$$O_2 \text{ yield} = \frac{\text{moles of evolved } O_2 \times 2}{\text{moles of } Na_2S_2O_8 \text{ added}} \times 100\%$$

$$\text{TOF} = \frac{\text{moles of evolved } O_2}{\text{moles of cobalt} \times \text{reaction time}}$$

### 5.2.4 Electrochemistry

Electrochemical performance for water oxidation was carried out on a Metrohm Autolab electrochemical workstation with a conventional three-electrode system in 40 mM borate buffer (pH = 8) using Pt plate as the counter electrode and Ag/AgCl (3 M KCl) as the reference electrode. For the heterogeneous reaction, the working electrode was prepared as following. Firstly, 5 mg of catalyst was suspended in a mixture of 10 μL of 5 wt% nafion ethanol solution, 250 μL of 2- propanol and 750 μL of water by ultrasonication. Then, 10 μL of the suspension was dropped on the surface of 5 mm carbon glassy rotating disk electrode (RDE) and was placed in air for natural drying. For the homogeneous reaction, 0.13 μM of CoPOM was dissolved in 40 mM borate buffer. Prior to the measurement, the electrolyte was bubbled with oxygen until it was saturated with oxygen. After that, the sample on RDE was subjected to potential cycling in the range of 0.2 V to 1.6 V with a scan rate of 100 mV/s for 40 cycles.

Cyclic voltammetry (CV) was then recorded at a scan rate of 20 mV/s with a rotating rate of 1600 rpm. Linear sweep voltammetry (LSV) was obtained at the scan rate of 2 mV/s. Tafel plot was obtained from the LSV data with resistance correction. The electrolysis was conducted at the applied potential of 1.3 V vs. NHE. All tests were performed in $O_2$-saturated electrolyte with a rotating rate of 1600 rpm.

### 5.2.5 Materials characterization

Powder X-ray diffraction (XRD) patterns were recorded on an X-ray diffractometer (Bruker AXS D8, Cu Kα, λ = 1.5406 Å, 40 kV and 20 mA) in the range of 5°–65°. FT-IR spectra were obtained with a Perkin Elmer FT-IR Spectrum GX using KBr technique in the range of 1800–400 $cm^{-1}$. The UV-visible absorption spectra were obtained on an UV-visible spectrophotometer (UV-2450, Shimadzu). An Agilent 7700x Inductively Coupled Plasma (ICP) was used to determine the cobalt contents. BET surface area was measured by $N_2$ adsorption and desorption at -196 $^oC$ using a Quantachrome Autosorb-6 sorption system. All samples were degassed at 150 °C for 12 h in vacuum before analysis. Pore size distribution was obtained by Barrett-Joyner-Halenda (BJH) method using the adsorption curve of the isotherm. The total pore volume was estimated by the amount of nitrogen adsorbed at the relative pressure of 0.99. The structural and morphological investigation and elemental mapping were conducted with transmission electron microscopy (TEM, JEOL, JEM-2100F) and energy-dispersive X-ray (EDX) spectroscopy. The X-ray photoelectron spectroscopy (XPS) spectrum was collected using XPS (AXIS-HSi, Kratos Analytical) and the obtained binding energy was calibrated using the C 1s peak at 284.7 eV. The Raman spectra were measured by Raman spectroscopy (Renishaw), using a He/Ne laser with a wavelength of 785 nm. The Co K-edge X-ray absorption near edge structure (XANES) spectra was recorded at Singapore Synchrotron Light Source (SSLS) using a beam line with energy of 1.85 GeV. A Si(111) monochromator was used for varying the energy between the desired range. Calibration was performed with a Co foil using the first point of inflection Co.

## 5.3 Results and Discussion

The CoPOM/MIL-101 catalyst was assembled via electrostatic interaction between the two oppositely charged components. The first step involved the synthesis of MIL-101 and CoPOM separately according to the previous reported methods[158,191,192]. The trimetric chromium (III) octahedral clusters in MIL-101 possess terminal water molecules, which can be removed from the framework after vacuum treatment at 150 °C for 12 h. It thus provides the coordinatively unsaturated sites as Lewis acid sites in the structure usable for the subsequent immobilization of CoPOM anions. As shown in Figure 5-1a, the experimental powder XRD patterns of MIL-101 and CoPOM are in good agreement with their simulated patterns, confirming the purity and good crystallinity of both materials. Upon immobilizing of CoPOM on MIL-101, the main peaks of MIL-101 are retained except that the intensities of peaks in $2\theta$ range of 5-6$^{o}$ decrease (Figure 5-1b). The intense peaks of (511) and (531) lattice planes located at small angles in XRD pattern of MIL-101 demonstrate its porous struc- ture. Upon immobilizing of CoPOM on MIL-101, the main peaks related to crystal planes of MIL-101, (6 0 6) and (7 5 3), are retained while the intensities of the peaks at low angles decrease. These findings suggest the encapsulation of CoPOM in the cavities of MIL-101 and the intact of the ordered structure of MIL-101[209]. Diffraction peaks of crystalline CoPOM are not noticeable except for the two weak peaks in the range of 28-30$^{o}$ (Figure 5-1c), which suggests that there may exist short range order among the encapsulated CoPOM anions. The $N_2$ adsorption isotherm of MIL-101 (Figure 5-1d) shows type I property with secondary uptakes at $P/P_0$ of around 0.1 and 0.2, suggesting the presence of two monodispersed windows of around 16 Å and 21 Å based on the pore size distribution profile[192] (Figure 5-1e). Owing to the large dimension of CoPOM anion (11.5 Å × 12.8 Å × 17.2 Å), it can only be hosted in the large cages of MIL-101[204]. The loading of CoPOM was determined to be 0.13 μmol/mg by ICP technique, which gives an estimation of 0.07 CoPOM anions per chromium corresponding to seven CoPOM anions in each cage[191]. The total volume of seven CoPOM anions is around 15 nm$^3$, which is smaller than the volume

of the large cage of around 20 $nm^3$.[158] The loading percentage of CoPOM obtained in this work is higher than the typical loadings of POMs in MIL-101 reported by others[205,210,211]. The BET surface area and pore volume of the pristine MIL-101 are calculated to be 4055 $m^2/g$ and 2.11 mL/g, respectively. After incorporation of CoPOM the values drop to 1157 $m^2/g$ and 0.862 mL/g. On the other hand, the pore size distribution is the same (Figure 5-1e) suggesting the size of apertures in MIL-101 is maintained. These results indicate that the cavities are partially blocked by the immobilized CoPOM. The FTIR spectra of CoPOM, MIL-101 and CoPOM/MIL-101 are shown in Figure 5-1f. Apart from the peaks attributed to MIL-101, CoPOM/MIL-101 also exhibits a series of bands of CoPOM with P-O stretching (1031 $cm^{-1}$), terminal W-O stretching (937 $cm^{-1}$) and W-O-W bending (892 and 788 $cm^{-1}$)[158]. All the results confirm that CoPOM has been successfully immobilized in the cavities of MIL-101.

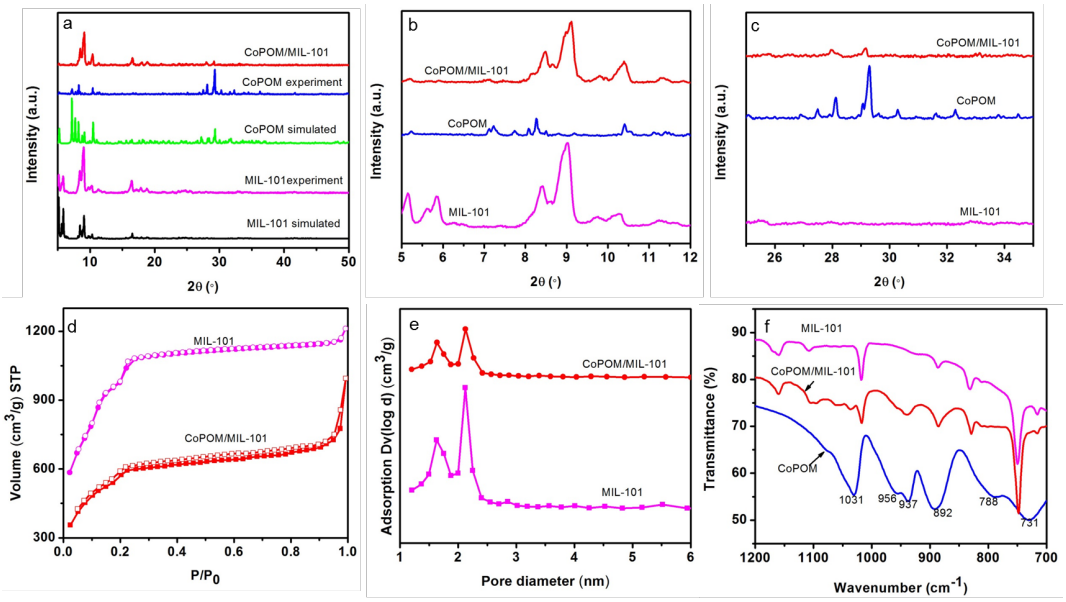


**Figure 5-1** (a) Powder XRD patterns of simulated MIL-101, as-prepared MIL-101, CoPOM, as-prepared CoPOM and CoPOM/MIL-101, Enlarged powder XRD patterns of MIL-101, CoPOM and CoPOM/MIL-101 in the range of (b) 5-12° and (c) 25-35°. (d) $N_2$ adsorption isotherm activated MIL-101, and CoPOM/MIL-101, (e)The BJH pore size distribution of MIL-101 and CoPOM/MIL-101 and (f) FTIR spectra of CoPOM, CoPOM/MIL-101 and MIL-101.

XPS and XANES spectroscopic techniques were applied to further confirm if the structure of CoPOM after being encapsulated in MIL-101 is retained. As shown in Figure 5-2a, compared with Co $2p_{3/2}$ peaks of CoPOM crystal at 781.1 eV, the corresponding peak assigned to that in CoPOM/MIL-101 is slightly shifted to a higher energy at 781.6 eV, which should be caused by the electrostatic interaction of CoPOM with MIL-101[161,212,213]. Moreover, there are strong satellite peaks, which is indicative of Co(II) species. It is in good agreement with the Co state in POM[158]. To further probe the structural information, the Co K-edge XANES of CoPOM/MIL-101 and CoPOM was investigated (Figure 5-2b). Several standards including $Co_3O_4$, $Co(OH)_2$ and $Co(NO_3)_2$ were also analyzed for comparison. It was found that the XANES spectrum of Co in CoPOM/MIL-101 is very different from those of the standards studied. Its oxidation state can be confirmed to be +2 by comparing the K-edge position of CoPOM/MIL-101 with the standards. The XANES spectrum of CoPOM/MIL-101 is matched well with that of the bare CoPOM except that its adsorption energy is slightly shifted to higher energy, which is consistent with the XPS result. Combining both the XPS and XANES analysis results, it can be concluded that CoPOM is immobilized in MIL-101 with its structure retained and there is guest-host interaction in the hybrid material.

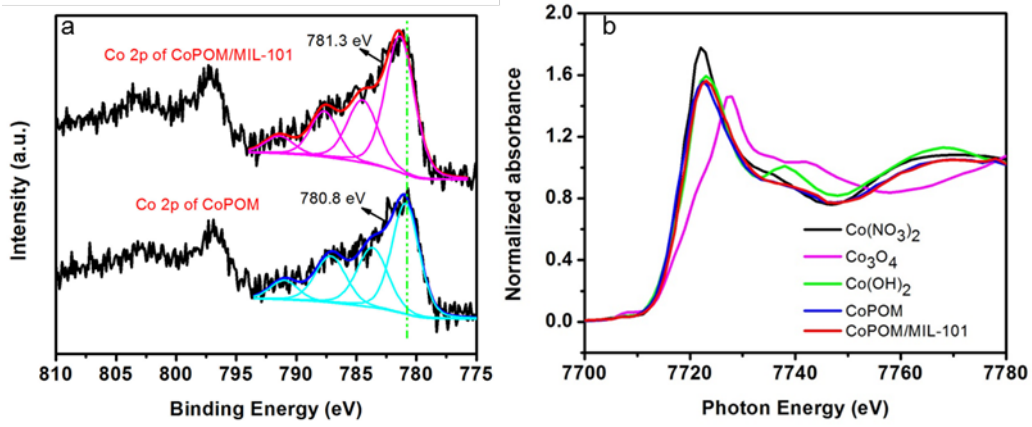


**Figure 5-2** (a) XPS spectra of Co 2p of CoPOM and CoPOM/MIL-101, (b) XANES

spectra of 1 ($Co_{3.9}$/MIL-101) before and after the photocatalytic reaction, $Co(OH)_2$, $Co_3O_4$ and $Co(NO_3)_2$, (c) the experimental and simulated XANES spectra of 1, and (d) Raman spectra of bare MIL-101, 1 and $Co_3O_4$.

TEM and EDX elemental mapping analyses were then applied to investigate the morphological properties and the spatial distribution of CoPOM in MIL-101. As shown in Figure 5-3, MIL-101 displays a typical octahedral shape with a smooth surface. After encapsulation of CoPOM, nanoparticles of around 3 nm with a good dispersion in the channel of MIL-101 are clearly observed (Figure 5-3b and 5-3c). These should be the clusters of encapsulated CoPOM anions. The EDX elemental mapping images of Cr, Co, P and W are shown in Figure 5-3e-h. The good dispersion of all the elements over a typical particle further confirms the uniform distribution of CoPOM in MIL-101. The atomic ratio determined by EDX is close to the elemental ratio in CoPOM molecule. The estimated CoPOM anions per chromium atom by the EDX is 0.08, which is close to the value determined by ICP. The TEM together with $N_2$ adsorption and EDX elemental mapping results suggest that the CoPOM anions are uniformly distributed in the cavities of MIL-101.

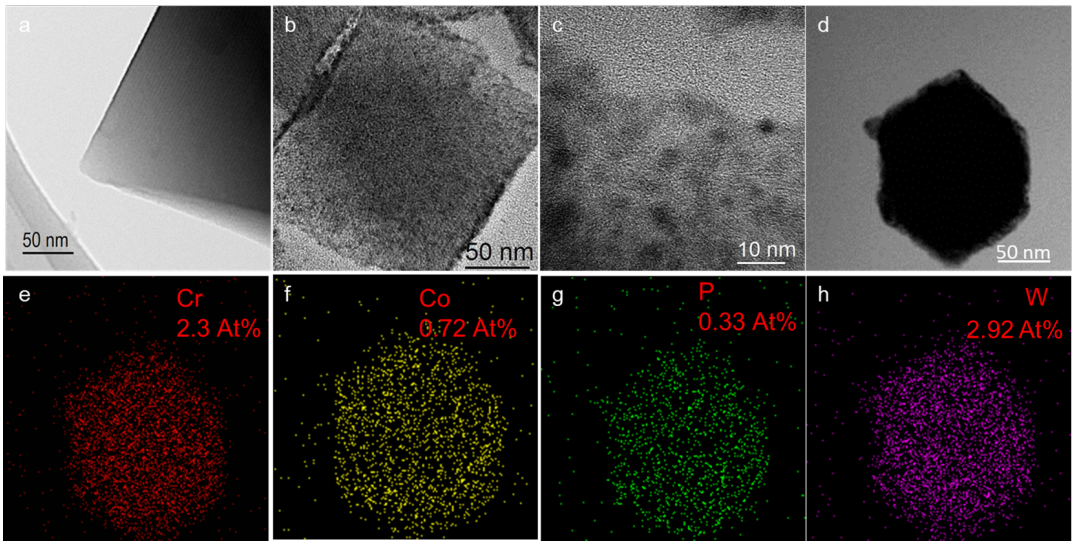


**Figure 5-3** TEM images of (a) MIL-101 and (b, c) CoPOM/MIL-101, (d) bright filed TEM image of CoPOM/MIL-101, and (e-h) EDX elemental mapping results of various elements.

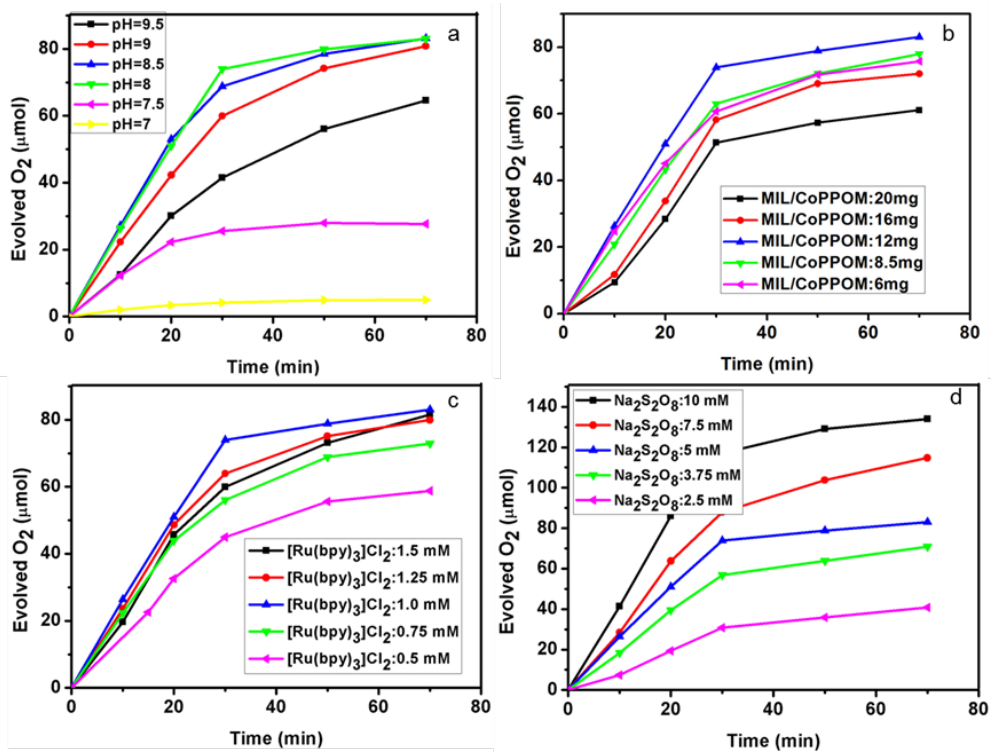


**Figure 5-4** (a)Time course of $O_2$ evolution over different pH, (b)Time course of $O_2$ evolution over different amount of CoPOM/MIL-101 as the catalysts, (c)Time course of $O_2$ evolution at different concentration of $[Ru(bpy)_3]Cl_2$, (d) Time course of $O_2$ evolution at different concentration of $Na_2S_2O_8$. Reaction condition: CoPOM,/MIL-101 $[Ru(bpy)_3]Cl_2$, and $Na_2S_2O_8$ in 50 mL of 40 mM borate buffer, 300 W Xenon lamp, $\lambda > 420$ nm.

The photocatalytic activity of CoPOM/MIL-101 was examined for water oxidation driven by visible light ($\lambda > 420$ nm) in 40 mM borate buffer using $Ru(bpy)_3^{2+}$ as the photosensitizer and $Na_2S_2O_8$ as the sacrificial reagent. The reaction conditions including pH and the concentrations of the catalyst, photosensitizer and sacrificial reagent were optimized (Figure 5-4). Under the optimized conditions, the amount of evolved $O_2$ is increased linearly for the first 30 min before leveling off (Figure 5-5a). The TOF of CoPOM/MIL-101 based on the reaction rate in the first 20 min and oxygen yield obtained after 70 min were calculated to be $7.1\times10^{-3}$ $s^{-1}$ per cobalt atom and 66%, respectively. These two values are higher than the TOF ($4.0\times10^{-3}$ $s^{-1}$ per

cobalt atom) and $O_2$ yield (49%) with an equivalent amount of free CoPOM under the same reaction conditions. Moreover, CoPOM/MIL-101 can be recovered from the solution easily after the reaction. The recovered CoPOM/MIL-101 was characterized by FTIR, XPS and XANES methods. The results indicate that CoPOM is preserved in MIL-101 with its structure intact (Figure 5-5b-d). The recovered CoPOM was then dispersed in fresh reaction solution and there is only a small drop in the activity (Figure 5-5a). Therefore, CoPOM encapsulated in MIL-101 is found more active for photocatalytic water oxidation compared with bare CoPOM. The enhancement is likely due to the interaction between CoPOM and MIL-101 as evidenced by the XPS and XANES results.

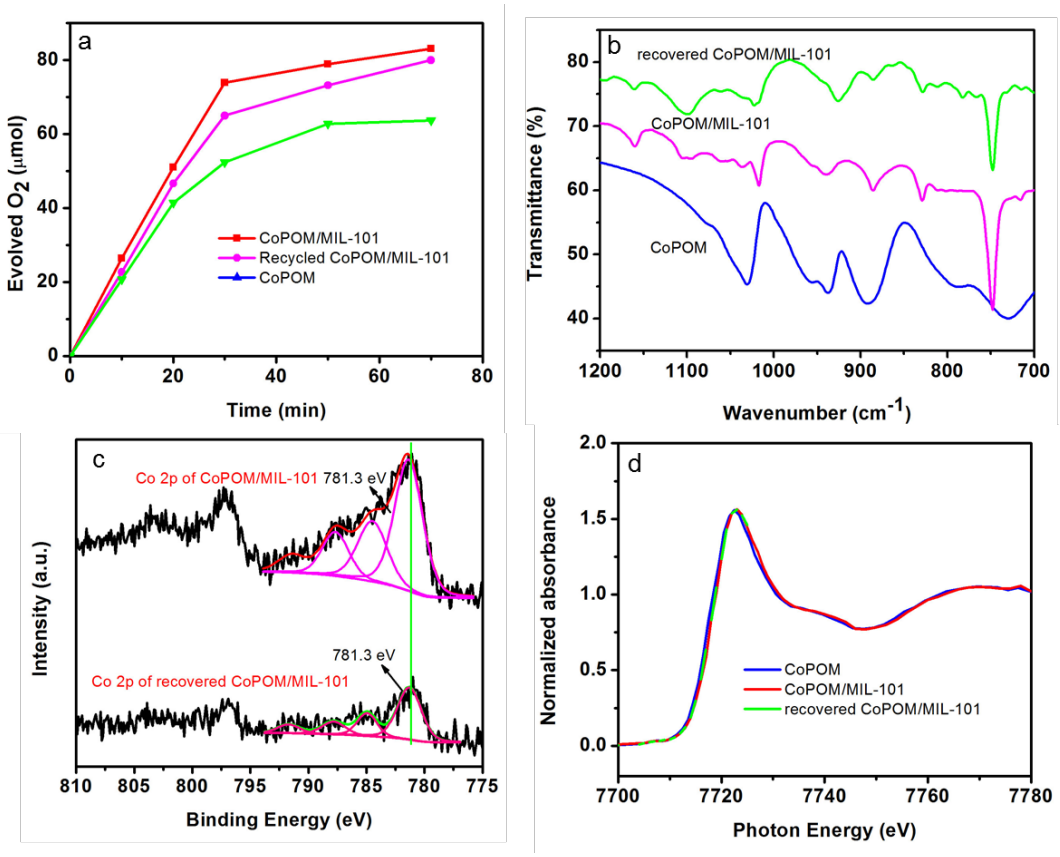


**Figure 5-5** (a) Time course of $O_2$ evolution over CoPOM/MIL-101, recycled CoPOM/MIL-101 and CoPOM. Reaction condition: 12.0 mg of catalysts, 5.0 mM of $Na_2S_2O_8$, 1.0 mM of $[Ru(bpy)_3]Cl_2$ in 50 mL of 40.0 mM borate buffer, pH = 8, 300 W Xenon lamp, $\lambda > 420$ nm. (b) FTIR spectra of CoPOM, CoPOM/MIL-101 and recovered CoPOM/MIL-101. (c) XPS of CoPOM/MIL-101 and recovered CoPOM/MIL-101. (d)XNAES of CoPOM, CoPOM/MIL-101 and recovered

CoPOM/MIL-101.

**Table 5-1** ICP determined cobalt concentration in solution after photocatalytic reaction before and after extraction using $THpA^+$.

| Aging time (h) | [Co] before extraction (μmol/L) | [Co] after extraction (μmol/L) |
|---|---|---|
| CoPOM/MIL-101 | 5.4 | 1.8 |
| CoPOM | - | 5.9 |

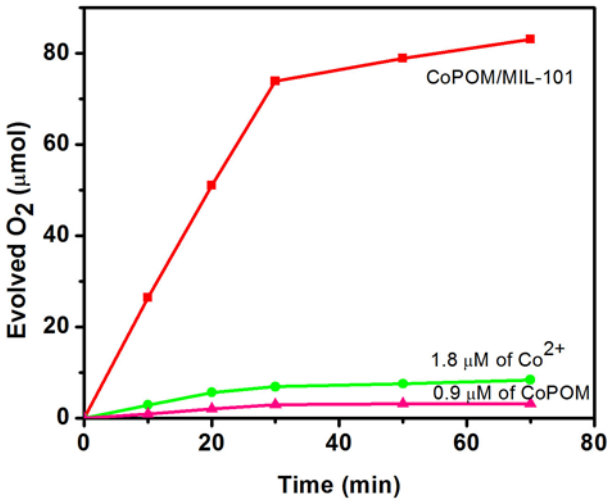


**Figure 5-6** Time course of $O_2$ evolution over CoPOM/MIL-101, the leached amounts of $Co^{2+}$ and CoPOM.

To further probe the stability of CoPOM/MIL-101 and CoPOM, a two-step process was applied to quantify the cobalt concentration in the solution after the reaction. Tetra-n-heptylammonium nitrate (THpANO3) toluene solution was used to extract CoPOM anions from the aqueous solution[214]. The concentration of cobalt in the aqueous solution before and after extraction was analyzed by ICP. The difference is attributed to the leached CoPOM from CoPOM/MIL-101. The concentration of cobalt in the aqueous solution after extraction is due to other dissolved cobalt species during the photocatalytic reaction. The results determined by ICP were shown in Table 5-1. It can be seen that the amount of soluble cobalt species produced during the

photocatalytic reaction is insignificant, which only accounts for 1.6% of total cobalt. This small amount of cobalt species should not be responsible for the high $O_2$ yield obtained based on the control experiment (Figure 5-6). As for CoPOM, the percentage that is leached to the reaction solution is about 2.8% of the total CoPOM in MIL-101. This amount of CoPOM is also not accountable for the overall high $O_2$ yield. The stability of free CoPOM was also examined by the same extraction method. A higher percentage of CoPOM (4.9%) was found to decompose to produce soluble cobalt species. Hence the immobilization of CoPOM in MIL-101 can improve its stability. Dynamic light scattering (DLS) was applied to investigate whether $CoO_x$ nanoparticles was produced during the reaction for both CoPOM/MIL-101 and CoPOM. No evidence of nanoparticles was shown for either CoPOM/MIL-101 or CoPOM. The above results suggest that CoPOM is stably immobilized on MIL-101 and the activity can be mostly recovered.

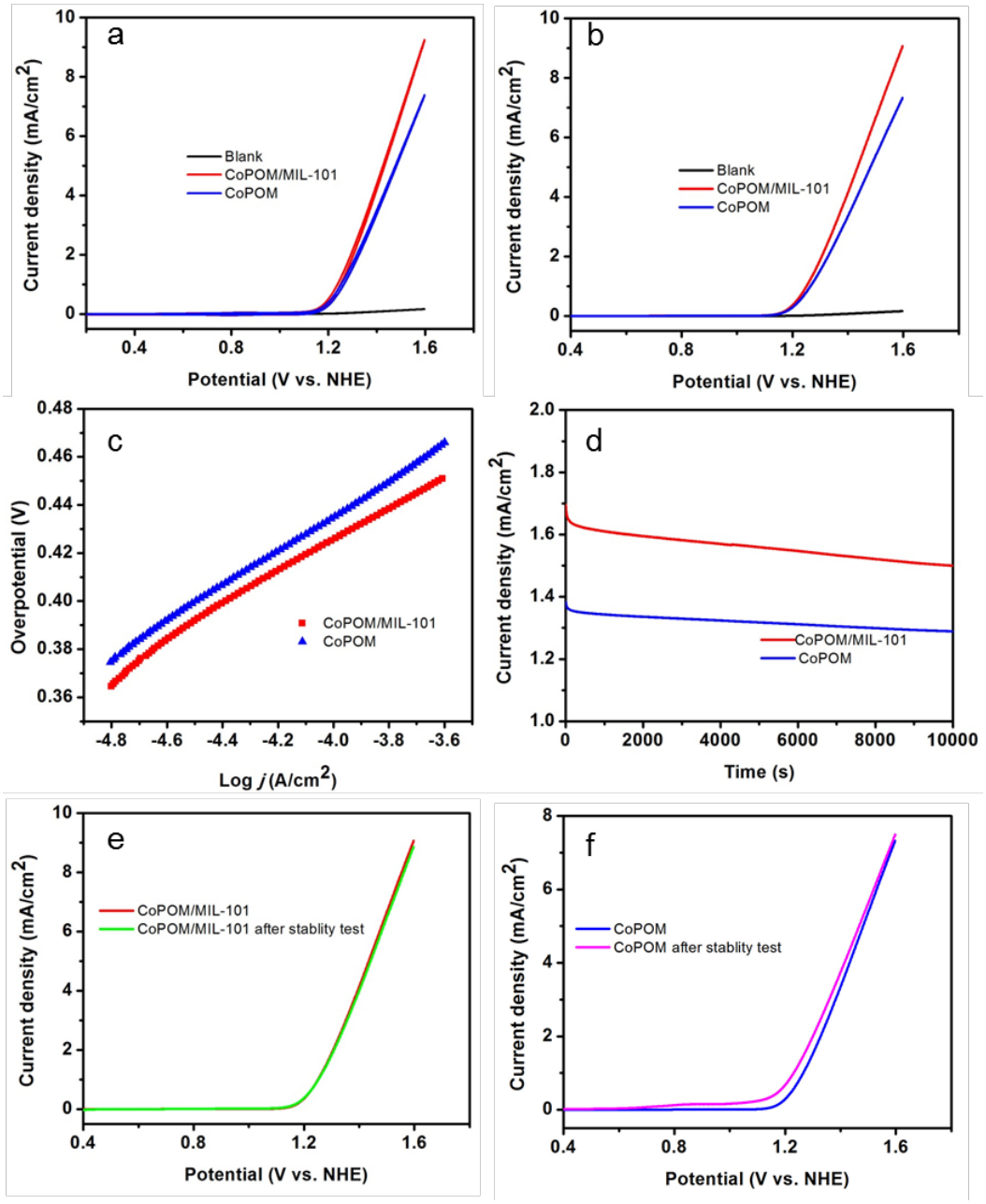


**Figure 5-7** (a) Cyclic voltammetry (CV) curves of CoPOM/MIL-101, CoPOM and without catalyst at a scan rate of 20 mV/s, (b) Linear sweep voltammetry (LSV) curves of CoPOM/MIL-101, CoPOM and without catalyst at a scan rate of 2 mV/s, (c) Tafel plots of CoPOM/MIL-101 and CoPOM obtained from LSV curves, and (d) i-t plots of CoPOM/MIL-101 and CoPOM. All tests were performed in $O_2$-saturated electrolyte (borate buffer, pH = 8) with a rotating rate of 1600 rpm. (e) Linear sweep voltammetry (LSV) curves of CoPOM/MIL-101 before and after stability test, (f) LSV curves of CoPOM before and after stability test at a scan rate of 2 mV/s.

To further assess the electrochemical catalytic water oxidation performance, CoPOM/MIL-101 was deposited on a 5 mm carbon glassy rotating disk electrode (RDE). The catalytic activity was studied in 40 mM of sodium borate buffer (pH = 8) in a standard three electrode system. Electrochemical behavior of the solution dissolved with an equivalent amount of CoPOM was also investigated for comparison. The CVs of CoPOM/MIL-101 and CoPOM at the scan rate of 20 mV/s are shown in Figure 5-7a. No redox waves are observed since the cobalt-based redox processes in CoPOM are voltammetrically silent in aqueous media[215]. The catalytic current due to water oxidation for CoPOM/MIL-101 occurs at ca. 1.1 V vs. NHE. The overpotential of CoPOM/MIL-101 was estimated to be 493 mV at the current density of 1 $mA/cm^2$ from LSV curve (Figure 5-7b). A similar LSV curve was obtained for CoPOM but with a lower current density and higher overpotential. Furthermore, Tafel slope for CoPOM/MIL-101 was calculated to be 69 mV/s, which is also smaller than 70 mV/s of CoPOM (Figure 5-7c). To further investigate the stability of CoPOM/MIL-101 and CoPOM in electrochemical catalytic progress, long-term electrolysis over 10000 s was carried out at the constant potential of 1.3 V vs. NHE. As shown in Figure 5-7d, the catalytic current of CoPOM/MIL-101 gradually became stable with bubbles generated on the surface of the working electrode. During the whole process, the current decreased slightly from 1.60 $mA/cm^2$ to 1.50 $mA/cm^2$, which should be caused by leakage of CoPOM. For comparison, catalytic current of CoPOM also dropped slightly drop from 1.34 $mA/cm^2$ to 1.29 $mA/cm^2$. The LSVs for both samples after the long-term electrolysis were also collected as shown in Figure 5-7e and 5-7f. It can be observed that a similar LSV curve was obtained for CoPOM/MIL-101 after the test. In contrast, a weak oxidation wave at around 0.9 V appears after the long-term electrolysis for CoPOM, indicating that $CoO_x$ derived from CoPOM could be generated on the surface of the working electrode[202]. Thus, it can be concluded that the mesoporous structure of MIL-101 not only can enhance the catalytic activity of CoPOM but also improve its stability.

## 5.4 Conclusion

In conclusion, CoPOM has been successfully immobilized in the cavities of MIL-101 by the impregnation method. The CoPOM anions are bounded to MIL-101 tightly to the coordinatively unsaturated sites of MIL-101 with an excellent dispersion. This modular construct with earth abundant materials exhibits good performances for both photocatalytic and electrochemical catalytic water oxidation. The combination also shows enhanced activity and stability compared with the soluble CoPOM. It is likely that the MIL-101 environment plays an important role for protecting the active CoPOM anions from decomposition. The immobilized catalyst can be recovered easily from the reaction solution for reuse without significant drop in the activity. The MIL-101 as a substrate can immobilize both heterogeneous and homogeneous catalysts and enhance their activity and stability for water oxidation. However the MIL-101 plays different role in this two reaction. It promotes the charge transfer between the catalyst and electrolyte when cobalt oxide was immobilized. On the other hand, no such phenomenon was observed when CoPOM was encapsulated though there is interaction between them. Thus, a ten times higher activity was obtained for the cobalt oxide system.

# CHAPTER 6 CONCLUSIONS AND OUTLOOK

## 6.1 Conclusions

The research work in this thesis is mainly focused on design of low cost, stable, efficient molecular and nanostructured catalysts toward dye sensitized solar fuel production. The main conclusions and findings are summarized as following:

(1) Dye sensitized nickel complexes with mixed donor for hydrogen production were developed. This work has shown that the complexes formed between Ni(II) and β-mecaptoethylamine with a mixed S and N donor environment are active and inexpensive catalysts for photocatalytic hydrogen evolution by water splitting. An excellent quantum efficiency of 30.9% was obtained at 480 nm. A reaction mechanism involving intramolecular proton transfer from N atom to Ni centre was proposed. This work provides us with useful clues to further explore noble-metal free complexes with a relevant environment to natural enzymes toward development of earth-abundant photocatalyst systems for solar hydrogen production.

(2) Cobalt oxide nanoparticles have been successfully embedded into the zeotypic giant cavities of MIL-101 by a facile impregnation and heat treatment method. The incorporated nanoparticles of 2-3 nm display an excellent dispersion and narrow size distribution. The apertures of the MOF, which are smaller than the size of cobalt oxide nanoparticles, prevent the nanoparticles from aggregation and leaching. This combination induces great enhancement in photocatalytic water oxidation activity with a high TOF of 0.012 $s^{-1}$ per cobalt atom, which is more than 9 fold compared with that of the unsupported $Co_3O_4$ nanoparticles. Moreover, MIL-101 also plays the role of promoting charge transfer as evidenced by the Nyquist plots. This study suggests that MIL-101 as a chemically stable MOF is a promising support for encapsulation of catalyst nanoparticles for photocatalytic applications.

(3) The polyoxometlates, CoPOM, was successfully immobilized in the cavities of MIL-101 by an impregnation method. The CoPOM anions are bounded to MIL-101 tightly by coordinating to the CUS of MIL-101 with excellent dispersion. This

modular construct with earth abundant materials shows high performance for both photocatalytic and electrochemical catalytic water oxidation. The combination also shows enhanced activity and stability compared with the free CoPOM. In addition, it is likely that the MIL-101 cavity plays an important role for protecting the active CoPOM anions from decomposition. Moreover, the highly porous structure offers an environment for the stacking of homogeneous catalytic anions in a single nanoparticle to achieve higher TOF. At last, the immobilized catalysts can be recovered from reaction solution, which is significant for the potential industrial application.

## 6.2 Outlook

Despite above mentioned achievements in dye sensitized molecular and nanostructured materials for water splitting; there is still critical challenge for researchers to design an efficient system for large scale practical application. Firstly, the efficiency for either half reaction is still too low to fully utilize the solar energy. Secondly, the mechanism of some intrinsic catalytic processes is not clear yet, which hinder us designing of more efficient catalyst. Thirdly, Dye and sacrificial reagents are still used in all the systems involving metal complexes as water splitting catalysts. The stability of the dye has to be dramatically improved in both strong reductive and oxidative conditions. Finally, as long as sacrificial reagents are used in photocatalytic water splitting system, it is impossible for us to say that we realize our objective of solar energy to chemical energy conversion. Coupling the water oxidation reaction with either water reduction reaction or $CO_2$ reduction reactions is the only approach to realize solar fuel production efficiently and environmental friendly.

(1) **Design novel metal complexes-based photocatalysts.** To date, although numbers of biomimetic metal complexes based on cobalt, iron, manganese and nickel have been explored for splitting water, there were no examples made of mixed metal centers so far as I know. It is known that hydrogenase and monooxygenase enzymes in nature contain more than one type of transition metal centers. For the monooxygenase enzymes, iron serves as the reaction center by activating oxygen

taking advantage of its redox capabilities, while other transition metals such as cobalt and manganese function as centers to bind oxygen. In light of this, it is curious that if mixed metal centers in synthetic metal complexes can act as differently in photocatalysis. Synergistic effect may also exist in these metal complexes. For example, if oxidative center and reductive center can designed in one complex, it could serve as an overall water splitting catalyst.

(2) **Build molecular device**. As indicated above, both the metal complexes and dyes are not very stable under the photocatalytic conditions. For example, Erythrosin Y used in our systems underwent photobleaching of both two iodide atoms in two hours upon irradiation. Reductive quenching took place since electron donor TEOA was present. However, Erythrosin Y was able to hold one iodide atom in the first two hours and loose the remaining iodide atom progressively in the next twenty-four hours if the catalyst was in the presence. This enhancement of stability can be attributed to the effective transfer of the electrons from the excited dye to our catalyst by oxidative quenching. It was seen that the stability of the photosensitized dye can be greatly enhanced by oxidative quenching. Building molecular device, which combines the photosensitizer and catalyst together, can dramatically promote oxidative quenching of photosensitizer by facilitating intramolecular electron transfer. Sun et al reported a porphyrin photosensitizer and a cobaloxime catalyst system by linking these two components. In this study, the fluorescence intensity was quenched only by 4% if the two components were physically mixed in the solution. A contrastive 64% quenching of the fluorescence intensity was observed when the two components were constructed as a molecular devices. The photocatalytic activity for hydrogen production also rose from 0 to 11 μmol in 5 hours. Hence, it is an effective approach to improve the electron transfer by building molecular devices.

(3) **Z-scheme water splitting**. Though both half reactions have been intensively studied, a system combining the both parts to construct an overall water splitting system is still rare. In 2009, Abe et al. reported the first example of Z-scheme water splitting involving dye sensitized systems. The mixture consisting of Pt-intercalated $H_2K_2Nb_6O_{17}$ sensitized by a coumarin dye for $H_2$ evolution, $IrO_2$–Pt co-loaded $WO_3$

for $O_2$ evolution, and an $I^{3-}/I^-$ redox couple succeeded splitting water into hydrogen and oxygen under visible light. However, it seems that so far this is the only example involving dye sensitized component because of the instability of dyes under powerful redox conditions. In Abe's case, the dye without thiophene rings also deactivated quickly under irradiation.

It has been thirty years since the discovery of Z-scheme water splitting. But compared with a unity of quantum yield green plants can achieve, an average quantum yield of 6% at 420-440 nm achieved is poor. Several obstacles await to be overcome. Though half reactions of water reduction have achieved quantum yield as high as 90% at the wavelength of 420nm, this half reaction is still the rate determining step for Z-scheme water splitting. Because when these water reduction photocatalysts are applied in Z-scheme systems, a pitiful average quantum yield was often obtained in the presence of redox mediators such as $Fe^{2+}/Fe^{3+}$ and $IO^{3-}/I^-$. Secondly, backward reactions are also a serious problem to hinder the promotion of the efficiency. It is that $Fe^{2+}$ or $I^-$ instead of water is oxidized at the WOC site. Thus enhancement of the selectivity of WOC is critical. Loading with suitable cocatalysts to promote forward reaction or directly remove the redox mediators are effective solutions. Kudo has reported Z-scheme systems without adding any mediators when Ru loaded Rh:$SrTiO_3$ and $BiVO_4$ are applied as WRC and WOC respectively. The range of the visible light that can be absorbed by the photocatalyst is another concern. If assuming a Z-scheme water splitting system attained with quantum yield of unity, the theoretical potential of photocatalysts with a 500 nm absorption edge has solar-energy-conversion efficiency of 7.9%, while photocatalysts with an absorption edge of 650 nm can obtain a conversion of 20.6%.

Building a mediator free Z-scheme water splitting is an appealing way to inhibit backward reaction. Direct transfer of electrons from WOC to WRC is possible, which has been proven by Kudo. To further promote the interparticle electron transfer, a more imitate contact between WRC and WOC with lower resistance is necessary. Gold and other conductive carbon and polymers connecting the WOC and WRC are promising approaches to facilitate this electron transfer. Dye sensitized systems may

also been employed for Z-scheme water splitting. Not only because of their wide range of visible light absorption, but also due to their ability to shuttle electrons. Very recently, Ishitani et al. reported such a Z-scheme system consisting of Ag-loaded TaON semiconductor and a Ru(II) dinuclear complex for $CO_2$ reduction.

(4) **Design of efficient catalysts for $CO_2$ reduction**. The research on photocatalytic $CO_2$ reduction toward solar fuel production is still at its early stage. Reduction of $CO_2$ is a tough task since high activation energy is required to activate $CO_2$ and the multiple reactions can occur as shown in equation 3-7. Though some efficiency for $CO_2$ reduction has been displayed by the conventional semiconductor-based photocatalysts, they exhibit limited photoresponse to visible light. It is promising to develop the dye sensitized $CO_2$ reduction system, in which the photosensitizer can be adjusted for better utilization of solar light and the catalyst can be modified for higher catalytic efficiency. Several systems involving ruthenium and rhenium complexes as photosensitizers have been studied for $CO_2$ reduction. Efficient catalysts are necessary to convert the photochemical one-electron transfer to multi-electron reduction of $CO_2$ in addition to the redox photosensitizer for photocatalytic fixation of $CO_2$. In future work, both the molecular and nanostructured catalysts will be investigated to develop efficient $CO_2$ reduction systems.

$$CO_2+2H^++2e^- \longrightarrow HCOOH \qquad E^o=-0.61V \text{ vs. NHE} \qquad (3)$$

$$CO_2+2H^++2e^- \longrightarrow CO+H_2O \qquad E^o=-0.53V \text{ vs. NHE} \qquad (4)$$

$$CO_2+4H^++4e^- \longrightarrow HCHO+H_2O \qquad E^o=-0.48V \text{ vs. NHE} \qquad (5)$$

$$CO_2+6H^++6e^- \longrightarrow CH_3OH+H_2O \qquad E^o=-0.38V \text{ vs. NHE} \qquad (6)$$

$$CO_2+8H^++8e^- \longrightarrow CH_4+H_2O \qquad E^o=-0.24V \text{ vs. NHE} \qquad (7)$$

# LIST OF PUBLICATIONS

(1) Han, J. Y.; Wang, D. P.; Du, Y. H.; Xi, S. B.; Chen, Z.; Yin, S. M.; Zhou, T. H. and Xu, R. Polyoxometalates immobilized on MIL-101(Cr) as an efficient catalyst for water oxidation. **2015**, in preparation.

(2) Han, J. Y.; Wang, D. P.; Du, Y. H.; Xi, S. B.; Chen, Z.; Yin, S. M.; Zhou, T. H. and Xu, R. Metal-Organic Framework immobilized cobalt oxide nanoparticles for efficient photocatalytic water oxidation. **2015**, in revision.

(3) Wu, Y. F.; Han J. Y.; Xue, P.; Xu, R. and Kang, Y. J. Nano Metal-Organic Framework (NMOF)-based strategies for multiplexed microRNA detection in solution and living cancer cells, *Nanoscale*, **2015**, *7*, 1753-1759. (co-first author)

(4) Han, J. Y.; Zhang, W.; Zhou, T. H.; Wang, X. and Xu R. Nickel-complexes with a mixed-donor ligand for photocatalytic hydrogen evolution from aqueous solutions under visible light, *RSC Advances*, **2012**, *2*, 8293-8296.

(5) Zhou, T. H.; Du, Y. H.; Borgna, A.; Hong, J. D.; Wang, Y. B.; Han, J. Y.; Zhang, W. and Xu, R. Post-synthesis modification of a metal-organic framework to construct a bifunctional photocatalyst for hydrogen production. *Energy & Enviromental Science*, **2013**, *6*, 3229-3234.

(6) Nie, L. N.; Xiong, W. W.; Li, P. Z.; Han, J. Y.; Zhang, G. D. Yin, S. M.; Zhao, Y. L.; Xu, R. and Zhang, Q. C. J*ournal of Solid State Chemistry*, **2014**, *220*, 118-123.

(7) Hong, J. D.; Yin, S. M.; Pan, Y. X.; Han, J. Y.; Zhou, T. H. and Xu, R. Porous carbon nitride nanosheets for enhanced photocatalytic activities. *Nanoscale*, **2014**, *6*, 14984-14990.

(8) Zhou, T. H.; Wang, D. P.; Simon, C. K. G.; Hong, J. D.; Han, J. Y.; Mao, J. G. and Xu, R. Bio-inspired organic cobalt(II) phosphonates toward water oxidation, *Energy & Enviromental Science*, **2015**, *8*, 526-534.

(9) Wu, R. B.; Wang, D. P.; Han, J. Y.; Liu, H.; Zhou, K.; Huang, Y. Z.; Xu, R. and Chen, Z. A general approach towards multi-faceted hollow oxide composites using zeolite imidazolate frameworks. *Nanoscale*, **2015**, *7*, 965-974.

(10) Nie, L. N.; Zhang, Y.; Ye, K. Q.; Han, J. Y.; Wang, Y.; Ganguly, R.; Li, Y. X.; Xu, R.; Yan, Q. Y and Zhang, Q. C. Crystalline Cu-Sn-S framework for high-performance lithium storage, *Journal of Material Chemistry A*, **2015**, accepted.

(11) Yin, S. M.; Han, J. Y.; Zhou, T. H. and Xu, R. Recent Progress in g-$C_3N_4$ based low cost photocatalytic system: activity enhancement and emerging applications, *Catalysis Science & Technology*, **2015**, accepted.

## REFERENCE

(1) Hammarström, L.; Hammes-Schiffer, S. *Acc. Chem. Res.* **2009**, *42*, 1859.

(2) Julia Ptasznik, S.; Communications development Incorporated, W., DC, Ed.; World Energy Council: New York, 2000.

(3) Norton, B. *Harnessing Solar Heat*; Springer, 2014; Vol. 18.

(4) Pearce, J. M. *Futures* **2002**, *34*, 663.

(5) Bazilian, M.; Onyeji, I.; Liebreich, M.; MacGill, I.; Chase, J.; Shah, J.; Gielen, D.; Arent, D.; Landfear, D.; Zhengrong, S. *Renew Energ* **2013**, *53*, 329.

(6) Styring, S. *Faraday Discuss.* **2012**, *155*, 357.

(7) Gust, D.; Moore, T. A.; Moore, A. L. *Acc. Chem. Res.* **2009**, *42*, 1890.

(8) Jones, L. W. *Toward a liquid hydrogen fuel economy*, University of Michigan Environmental Action for Survival Teach In. Ann Arbor, 1970.

(9) Fujishima, A.; Honda, K. *Nature* **1972**, *238*, 37.

(10) Kohl, S. W.; Weiner, L.; Schwartsburd, L.; Konstantinovski, L.; Shimon, L. J. W.; Ben-David, Y.; Iron, M. A.; Milstein, D. *Science* **2009**, *324*, 74.

(11) Britt, R. D. *In Oxygenic Photosynthesis:The Light Reactions*; Kluwer Academic Publishers: Dordrecht, The Netherlands, 1966.

(12) Kawai, T.; Sakata, T. *Nature* **1979**, *282*, 283.

(13) Kawai, T.; Sakata, T. *Nature* **1980**, *286*, 474.

(14) Kawai, T.; Sakata, T. *Chem. Lett.* **1981**, *10*, 81.

(15) Kawai, T.; Sakata, T. *J. Chem. Soc., Chem. Commun.* **1979**, 1047.

(16) Domen, K.; Naito, S.; Onishi, T.; Tamaru, K.; Soma, M. *J. Phys. Chem.* **1982**, *86*, 3657.

(17) Jeong, H.; Kim, T.; Kim, D.; Kim, K. *Int. J. Hydrogen. Energ.* **2006**, *31*, 1142.

(18) Takata, T.; Furumi, Y.; Shinohara, K.; Tanaka, A.; Hara, M.; Kondo, J. N.; Domen, K. *Chem. Mater.* **1997**, *9*, 1063.

(19) G. Kim, H.; W. Hwang, D.; Kim, J.; G. Kim, Y.; S. Lee, J. *Chem. Commun.* **1999**, 1077.

(20) Ogura, S.; Sato, K.; Inoue, Y. *Phys. Chem. Chem. Phys.* **2000**, *2*, 2449.

(21) Zou, J.-J.; Liu, C.-J.; Zhang, Y.-P. *Langmuir* **2006**, *22*, 2334.

(22) Kato, H.; Asakura, K.; Kudo, A. *J. Am. Chem. Soc.* **2003**, *125*, 3082.

(23) Kudo, A.; Hijii, S. *Chem. Lett.* **1999**, *28*, 1103.

(24) Sato, J.; Saito, N.; Nishiyama, H.; Inoue, Y. *J. Phys. Chem. B.* **2003**, *107*, 7965.

(25) Yanagida, T.; Sakata, Y.; Imamura, H. *Chem. Lett.* **2004**, *33*, 726.

(26) Sato, J.; Saito, N.; Nishiyama, H.; Inoue, Y. *J. Photochem. Photobiol. A: Chem.* **2002**, *148*, 85.

(27) Sato, J.; Kobayashi, H.; Ikarashi, K.; Saito, N.; Nishiyama, H.; Inoue, Y. *J. Phys. Chem. B.* **2004**, *108*, 4369.

(28) Chen, D.; Ye, J. *Chem. Mater.* **2007**, *19*, 4585.

(29) Krishna Reddy, J.; Suresh, G.; Hymavathi, C. H.; Durga Kumari, V.; Subrahmanyam, M. *Catal. Today* **2009**, *141*, 89.

(30) Borgarello, E.; Kiwi, J.; Graetzel, M.; Pelizzetti, E.; Visca, M. *J. Am. Chem. Soc.* **1982**, *104*, 2996.

(31) Chen, X.; Mao, S. S. *Chem. Rev.* **2007**, *107*, 2891.

(32) Leung, D. Y. C.; Fu, X.; Wang, C.; Ni, M.; Leung, M. K. H.; Wang, X.; Fu, X. *ChemSusChem* **2010**, *3*, 681.

(33) Kudo, A.; Sekizawa, M. *Chem. Commun.* **2000**, 1371.

(34) Zhang, J.; Wu, Y.; Xing, M.; Leghari, S. A. K.; Sajjad, S. *Energ. Environ. Sci.* **2010**, *3*, 715.

(35) Fan, X.; Chen, X.; Zhu, S.; Li, Z.; Yu, T.; Ye, J.; Zou, Z. *J. Mol. Catal. A: Chem.* **2008**, *284*, 155.

(36) Hwang, D. W.; Kim, H. G.; Lee, J. S.; Kim, J.; Li, W.; Oh, S. H. *J. Phys. Chem. B.* **2005**, *109*, 2093.

(37) Kato, H.; Kudo, A. *J. Phys. Chem. B.* **2002**, *106*, 5029.

(38) Liu, G.; Zhao, Y.; Sun, C.; Li, F.; Lu, G. Q.; Cheng, H.-M. *Angew. Chem. Int. Ed.* **2008**, *47*, 4516.

(39) Li, J.; Xu, J.; Dai, W.-L.; Li, H.; Fan, K. *Appl. Catal. B.: Environ.* **2008**, *82*,

233.

(40)Cong, Y.; Zhang, J.; Chen, F.; Anpo, M.; He, D. *J. Phys. Chem. C.* **2007**, *111*, 10618.

(41)Li, D.; Haneda, H.; Hishita, S.; Ohashi, N. *Chem. Mater.* **2005**, *17*, 2596.

(42)huo, Y.; jin, Y.; zhu, J.; li, H. *Appl. Catal. B.: Environ.* **2009**, *89*, 543.

(43)Yi, Z. G.; Ye, J. H. *Appl. Phys. Lett.* **2007**, *91*, 254108.

(44)Bao, N.; Shen, L.; Takata, T.; Domen, K. *Chem. Mater.* **2008**, *20*, 110.

(45)Zong, X.; Yan, H.; Wu, G.; Ma, G.; Wen, F.; Wang, L.; Li, C. *J. Am. Chem. Soc.* **2008**, *130*, 7176.

(46)Yan, H.; Yang, J.; Ma, G.; Wu, G.; Zong, X.; Lei, Z.; Shi, J.; Li, C. *J. Catal.* **2009**, *266*, 165.

(47)Zhang, W.; Wang, Y.; Wang, Z.; Zhong, Z.; Xu, R. *Chem. Commun.* **2010**, *46*, 7631.

(48)Kudo, A.; Tsuji, I.; Kato, H. *Chem. Commun.* **2002**, 1958.

(49)Tsuji, I.; Kato, H.; Kobayashi, H.; Kudo, A. *J. Am. Chem. Soc.* **2004**, *126*, 13406.

(50)Tsuji, I.; Kato, H.; Kobayashi, H.; Kudo, A. *J. Phys. Chem. B.* **2005**, *109*, 7323.

(51)Tsuji, I.; Kato, H.; Kudo, A. *Angew. Chem. Int. Ed.* **2005**, *44*, 3565.

(52)Tsuji, I.; Kato, H.; Kudo, A. *Chem. Mater.* **2006**, *18*, 1969.

(53)Kasahara, A.; Nukumizu, K.; Hitoki, G.; Takata, T.; Kondo, J. N.; Hara, M.; Kobayashi, H.; Domen, K. *J. Phys. Chem. A.* **2002**, *106*, 6750.

(54)Hara, M.; Hitoki, G.; Takata, T.; Kondo, J. N.; Kobayashi, H.; Domen, K. *Catal. Today* **2003**, *78*, 555.

(55)Hitoki, G.; Takata, T.; Kondo, J. N.; Hara, M.; Kobayashi, H.; Domen, K. *Chem. Commun.* **2002**, 1698.

(56)Maeda, K.; Takata, T.; Hara, M.; Saito, N.; Inoue, Y.; Kobayashi, H.; Domen, K. *J. Am. Chem. Soc.* **2005**, *127*, 8286.

(57)Maeda, K.; Teramura, K.; Lu, D.; Takata, T.; Saito, N.; Inoue, Y.; Domen, K. *Nature* **2006**, *440*, 295.

(58) Maeda, K.; Teramura, K.; Masuda, H.; Takata, T.; Saito, N.; Inoue, Y.; Domen, K. *J. Phys. Chem. B.* **2006**, *110*, 13107.

(59) Maeda, K.; Teramura, K.; Takata, T.; Hara, M.; Saito, N.; Toda, K.; Inoue, Y.; Kobayashi, H.; Domen, K. *J. Phys. Chem. B.* **2005**, *109*, 20504.

(60) Hirai, T.; Maeda, K.; Yoshida, M.; Kubota, J.; Ikeda, S.; Matsumura, M.; Domen, K. *J. Phys. Chem. C.* **2007**, *111*, 18853.

(61) Maeda, K.; Hashiguchi, H.; Masuda, H.; Abe, R.; Domen, K. *J. Phys. Chem. C.* **2008**, *112*, 3447.

(62) Yashima, M.; Yamada, H.; Maeda, K.; Domen, K. *Chem. Commun.* **2010**, *46*, 2379.

(63) Ohno, T.; Bai, L.; Hisatomi, T.; Maeda, K.; Domen, K. *J. Am. Chem. Soc.* **2012**, *134*, 8254.

(64) Lee, Y.; Terashima, H.; Shimodaira, Y.; Teramura, K.; Hara, M.; Kobayashi, H.; Domen, K.; Yashima, M. *J. Phys. Chem. C.* **2007**, *111*, 1042.

(65) Tessier, F.; Maillard, P.; Lee, Y.; Bleugat, C.; Domen, K. *J. Phys. Chem. C.* **2009**, *113*, 8526.

(66) Meyer, T. J. *Acc. Chem. Res.* **1989**, *22*, 163.

(67) Juris, A.; Balzani, V.; Barigelletti, F.; Campagna, S.; Belser, P.; von Zelewsky, A. *Coord. Chem. Rev.* **1988**, *84*, 85.

(68) Collin, J. P.; Guillerez, S.; Sauvage, J. P.; Barigelletti, F.; De Cola, L.; Flamigni, L.; Balzani, V. *Inorg. Chem.* **1991**, *30*, 4230.

(69) Cline, E. D.; Adamson, S. E.; Bernhard, S. *Inorg. Chem.* **2008**, *47*, 10378.

(70) Du, P.; Schneider, J.; Jarosz, P.; Zhang, J.; Brennessel, W. W.; Eisenberg, R. *J. Phys. Chem. B.* **2007**, *111*, 6887.

(71) Zhang, D.; Wu, L.-Z.; Zhou, L.; Han, X.; Yang, Q.-Z.; Zhang, L.-P.; Tung, C.-H. *J. Am. Chem. Soc.* **2004**, *126*, 3440.

(72) Shimidzu, T.; Iyoda, T.; Koide, Y. *J. Am. Chem. Soc.* **1985**, *107*, 35.

(73) Krishnan, C. V.; Sutin, N. *J. Am. Chem. Soc.* **1981**, *103*, 2141.

(74) Fisher, B. J.; Eisenberg, R. *J. Am. Chem. Soc.* **1980**, *102*, 7361.

(75) Lehn, J.-M.; Ziessel, R. *Proc. Natl. Acad. Sci.* **1982**, *79*, 701.

(76) J. Hawecker, J. M. L. a. R. Z. *Nouv J. Chim.* **1983**, *7*.

(77) Connolly, P.; Espenson, J. H. *Inorg. Chem.* **1986**, *25*, 2684.

(78) Zhang, P.; Wang, M.; Dong, J.; Li, X.; Wang, F.; Wu, L.; Sun, L. *J. Phys. Chem. C.* **2010**, *114*, 15868.

(79) Lazarides, T.; McCormick, T.; Du, P.; Luo, G.; Lindley, B.; Eisenberg, R. *J. Am. Chem. Soc.* **2009**, *131*, 9192.

(80) Fontecilla-Camps, J. C.; Volbeda, A.; Cavazza, C.; Nicolet, Y. *Chem. Rev.* **2007**, *107*, 4273.

(81) Li, Z.; Ohki, Y.; Tatsumi, K. *J. Am. Chem. Soc.* **2005**, *127*, 8950.

(82) Barton, B. E.; Whaley, C. M.; Rauchfuss, T. B.; Gray, D. L. *J. Am. Chem. Soc.* **2009**, *131*, 6942.

(83) Tard, C. d.; Pickett, C. J. *Chem. Rev. (Washington, DC, U. S.)* **2009**, *109*, 2245.

(84) Wilson, A. D.; Newell, R. H.; McNevin, M. J.; Muckerman, J. T.; Rakowski DuBois, M.; DuBois, D. L. *J. Am. Chem. Soc.* **2005**, *128*, 358.

(85) Kilgore, U. J.; Roberts, J. A. S.; Pool, D. H.; Appel, A. M.; Stewart, M. P.; DuBois, M. R.; Dougherty, W. G.; Kassel, W. S.; Bullock, R. M.; DuBois, D. L. *J. Am. Chem. Soc.* **2011**, *133*, 5861.

(86) Rakowski Dubois, M.; Dubois, D. L. *Acc. Chem. Res.* **2009**, *42*, 1974.

(87) McLaughlin, M. P.; McCormick, T. M.; Eisenberg, R.; Holland, P. L. *Chem. Commun. (Cambridge, U. K.)* **2011**, *47*, 7989.

(88) Na, Y.; Wang, M.; Pan, J.; Zhang, P.; Åkermark, B.; Sun, L. *Inorg. Chem.* **2008**, *47*, 2805.

(89) Gärtner, F.; Sundararaju, B.; Surkus, A.-E.; Boddien, A.; Loges, B.; Junge, H.; Dixneuf, P. H.; Beller, M. *Angew Chem, Int Ed* **2009**, *48*, 9962.

(90) Han, Z.; McNamara, W. R.; Eum, M.-S.; Holland, P. L.; Eisenberg, R. *Angew. Chem. Int. Ed.* **2012**, *51*, 1667.

(91) Zhang, W.; Hong, J.; Zheng, J.; Huang, Z.; Zhou, J.; Xu, R. *J. Am. Chem. Soc.* **2011**, *133*, 20680.

(92) Weinberg, D. R.; Gagliardi, C. J.; Hull, J. F.; Murphy, C. F.; Kent, C. A.;

Westlake, B. C.; Paul, A.; Ess, D. H.; McCafferty, D. G.; Meyer, T. J. *Chem. Rev.* **2012**, *112*, 4016.

(93) Gagliardi, C. J.; Vannucci, A. K.; Concepcion, J. J.; Chen, Z.; Meyer, T. J. *Energ. Environ. Sci.* **2012**, *5*, 7704.

(94) Inoue, H.; Shimada, T.; Kou, Y.; Nabetani, Y.; Masui, D.; Takagi, S.; Tachibana, H. *ChemSusChem* **2011**, *4*, 173.

(95) Kiwi, J.; Grätzel, M. *Angew. Chem, Int. Ed.* **1978**, *17*, 860.

(96) Beni, G.; Schiavone, L. M.; Shay, J. L.; Dautremont-Smith, W. C.; Schneider, B. S. *Nature* **1979**, *282*, 281.

(97) Kiwi, J.; Grätzel, M. *Angew. Chem, Int. Ed.* **1979**, *18*, 624.

(98) Kiwi, J.; Borgarello, E.; Pelizzetti, E.; Visca, M.; Grätzel, M. *Angew. Chem, Int. Ed.* **1980**, *19*, 646.

(99) Zhang, Y.; Judkins, E. C.; McMillin, D. R.; Mehta, D.; Ren, T. *ACS Catal.* **2013**, *3*, 2474.

(100) Frame, F. A.; Townsend, T. K.; Chamousis, R. L.; Sabio, E. M.; Dittrich, T.; Browning, N. D.; Osterloh, F. E. *J. Am. Chem. Soc.* **2011**, *133*, 7264.

(101) Brimblecombe, R.; Swiegers, G. F.; Dismukes, G. C.; Spiccia, L. *Angew. Chem. Int. Ed.* **2008**, *47*, 7335.

(102) Brimblecombe, R.; Koo, A.; Dismukes, G. C.; Swiegers, G. F.; Spiccia, L. *J. Am. Chem. Soc.* **2010**, *132*, 2892.

(103) Dismukes, G. C.; Brimblecombe, R.; Felton, G. A. N.; Pryadun, R. S.; Sheats, J. E.; Spiccia, L.; Swiegers, G. F. *Acc. Chem. Res.* **2009**, *42*, 1935.

(104) Chen, Z.; Jiao, Z.; Pan, D.; Li, Z.; Wu, M.; Shek, C.-H.; Wu, C. M. L.; Lai, J. K. L. *Chem. Rev.* **2012**, *112*, 3833.

(105) Park, J.; Kim, H.; Jin, K.; Lee, B. J.; Park, Y.-S.; Kim, H.; Park, I.; Yang, K. D.; Jeong, H.-Y.; Kim, J.; Hong, K. T.; Jang, H. W.; Kang, K.; Nam, K. T. *J. Am. Chem. Soc.* **2014**, *136*, 4201.

(106) Hill, J. P.; Palza, H.; Alam, S.; Ariga, K.; Schumacher, A. L.; D'Souza, F.; Anson, C. E.; Powell, A. K. *Inorg. Chem.* **2008**, *47*, 8306.

(107) Tanase, T.; Lippard, S. J. *Inorg. Chem.* **1995**, *34*, 4682.

(108) Post, J. E. *Proc. Natl. Acad. Sci.* **1999**, *96*, 3447.

(109) Robinson, D. M.; Go, Y. B.; Mui, M.; Gardner, G.; Zhang, Z.; Mastrogiovanni, D.; Garfunkel, E.; Li, J.; Greenblatt, M.; Dismukes, G. C. *J. Am. Chem. Soc.* **2013**, *135*, 3494.

(110) Najafpour, M. M.; Ehrenberg, T.; Wiechen, M.; Kurz, P. *Angew. Chem. Int. Ed.* **2010**, *49*, 2233.

(111) Birkner, N.; Navrotsky, A. *Proc. Natl. Acad. Sci.* **2014**, *111*, 6209.

(112) Yocum, C. F. *Coord. Chem. Rev.* **2008**, *252*, 296.

(113) Mukherjee, S.; Stull, J. A.; Yano, J.; Stamatatos, T. C.; Pringouri, K.; Stich, T. A.; Abboud, K. A.; Britt, R. D.; Yachandra, V. K.; Christou, G. *Proc. Natl. Acad. Sci.* **2012**, *109*, 2257.

(114) Kanan, M. W.; Nocera, D. G. *Science* **2008**, *321*, 1072.

(115) Kanan, M. W.; Yano, J.; Surendranath, Y.; Dincă, M.; Yachandra, V. K.; Nocera, D. G. *J. Am. Chem. Soc.* **2010**, *132*, 13692.

(116) Risch, M.; Khare, V.; Zaharieva, I.; Gerencser, L.; Chernev, P.; Dau, H. *J. Am. Chem. Soc.* **2009**, *131*, 6936.

(117) Surendranath, Y.; Lutterman, D. A.; Liu, Y.; Nocera, D. G. *J. Am. Chem. Soc.* **2012**, *134*, 6326.

(118) Harriman, A.; Pickering, I. J.; Thomas, J. M.; Christensen, P. A. *J. Chem. Soc., Faraday Trans.* **1988**, *84*, 2795.

(119) Singh, R. N.; Mishra, D.; Anindita; Sinha, A. S. K.; Singh, A. *Electrochem. Commun.* **2007**, *9*, 1369.

(120) Jiao, F.; Frei, H. *Angew. Chem. Int. Ed.* **2009**, *48*, 1841.

(121) Yusuf, S.; Jiao, F. *ACS Catal.* **2012**, *2*, 2753.

(122) Rosen, J.; Hutchings, G. S.; Jiao, F. *J. Am. Chem. Soc.* **2013**, *135*, 4516.

(123) Grzelczak, M.; Zhang, J.; Pfrommer, J.; Hartmann, J.; Driess, M.; Antonietti, M.; Wang, X. *ACS Catal.* **2013**, *3*, 383.

(124) Zhang, Y.; Rosen, J.; Hutchings, G. S.; Jiao, F. *Catal. Today* **2014**, *225*, 171.

(125) Wu, R.; Wang, D. P.; Han, J.; Liu, H.; Zhou, K.; Huang, Y.; Xu, R.; Wei,

J.; Chen, X.; Chen, Z. *Nanoscale* **2015**, *7*, 965.

(126) Gersten, S. W.; Samuels, G. J.; Meyer, T. J. *J. Am. Chem. Soc.* **1982**, *104*, 4029.

(127) Gilbert, J. A.; Eggleston, D. S.; Murphy, W. R.; Geselowitz, D. A.; Gersten, S. W.; Hodgson, D. J.; Meyer, T. J. *J. Am. Chem. Soc.* **1985**, *107*, 3855.

(128) Xu, Y.; Fischer, A.; Duan, L.; Tong, L.; Gabrielsson, E.; Åkermark, B.; Sun, L. *Angew. Chem. Int. Ed.* **2010**, *49*, 8934.

(129) Kärkäs, M. D.; Åkermark, T.; Johnston, E. V.; Karim, S. R.; Laine, T. M.; Lee, B.-L.; Åkermark, T.; Privalov, T.; Åkermark, B. *Angew. Chem. Int. Ed.* **2012**, *51*, 11589.

(130) Kärkäs, M. D.; Åkermark, T.; Chen, H.; Sun, J.; Åkermark, B. *Angew. Chem. Int. Ed.* **2013**, *52*, 4189.

(131) Volpe, A.; Sartorel, A.; Tubaro, C.; Meneghini, L.; Di Valentin, M.; Graiff, C.; Bonchio, M. *Eur. J. Inorg. Chem.* **2014**, *2014*, 665.

(132) Hintermair, U.; Sheehan, S. W.; Parent, A. R.; Ess, D. H.; Richens, D. T.; Vaccaro, P. H.; Brudvig, G. W.; Crabtree, R. H. *J. Am. Chem. Soc.* **2013**, *135*, 10837.

(133) Karlsson, E. A.; Lee, B.-L.; Åkermark, T.; Johnston, E. V.; Kärkäs, M. D.; Sun, J.; Hansson, Ö.; Bäckvall, J.-E.; Åkermark, B. *Angew. Chem. Int. Ed.* **2011**, *50*, 11715.

(134) Gopalaiah, K. *Chem. Rev.* **2013**, *113*, 3248.

(135) Bolm, C.; Legros, J.; Le Paih, J.; Zani, L. *Chem. Rev.* **2004**, *104*, 6217.

(136) Nam, W. *Acc. Chem. Res.* **2007**, *40*, 522.

(137) Ellis, W. C.; McDaniel, N. D.; Bernhard, S.; Collins, T. J. *J. Am. Chem. Soc.* **2010**, *132*, 10990.

(138) Chen, G.; Chen, L.; Ng, S.-M.; Man, W.-L.; Lau, T.-C. *Angew. Chem. Int. Ed.* **2013**, *52*, 1789.

(139) Harriman, A.; Porter, G.; Walters, P. *J. Chem. Soc., Faraday Trans.* **1981**, *77*, 2373.

(140) Leung, C.-F.; Ng, S.-M.; Ko, C.-C.; Man, W.-L.; Wu, J.; Chen, L.; Lau, T.-C. *Energ. Environ. Sci.* **2012**, *5*, 7903.

(141) Nakazono, T.; Parent, A. R.; Sakai, K. *Chem. Commun.* **2013**, *49*, 6325.

(142) Pizzolato, E.; Natali, M.; Posocco, B.; Montellano Lopez, A.; Bazzan, I.; Di Valentin, M.; Galloni, P.; Conte, V.; Bonchio, M.; Scandola, F.; Sartorel, A. *Chem. Commun.* **2013**, *49*, 9941.

(143) Fu, S.; Liu, Y.; Ding, Y.; Du, X.; Song, F.; Xiang, R.; Ma, B. *Chem. Commun.* **2014**, *50*, 2167.

(144) Geletii, Y. V.; Huang, Z.; Hou, Y.; Musaev, D. G.; Lian, T.; Hill, C. L. *J. Am. Chem. Soc.* **2009**, *131*, 7522.

(145) Besson, C.; Huang, Z.; Geletii, Y. V.; Lense, S.; Hardcastle, K. I.; Musaev, D. G.; Lian, T.; Proust, A.; Hill, C. L. *Chem. Commun.* **2010**, *46*, 2784.

(146) Puntoriero, F.; La Ganga, G.; Sartorel, A.; Carraro, M.; Scorrano, G.; Bonchio, M.; Campagna, S. *Chem. Commun.* **2010**, *46*, 4725.

(147) Huang, Z.; Luo, Z.; Geletii, Y. V.; Vickers, J. W.; Yin, Q.; Wu, D.; Hou, Y.; Ding, Y.; Song, J.; Musaev, D. G.; Hill, C. L.; Lian, T. *J. Am. Chem. Soc.* **2011**, *133*, 2068.

(148) Zhu, G.; Geletii, Y. V.; Kogerler, P.; Schilder, H.; Song, J.; Lense, S.; Zhao, C.; Hardcastle, K. I.; Musaev, D. G.; Hill, C. L. *Dalton. Trans.* **2012**, *41*, 2084.

(149) Zhu, G.; Glass, E. N.; Zhao, C.; Lv, H.; Vickers, J. W.; Geletii, Y. V.; Musaev, D. G.; Song, J.; Hill, C. L. *Dalton. Trans.* **2012**, *41*, 13043.

(150) Natali, M.; Orlandi, M.; Berardi, S.; Campagna, S.; Bonchio, M.; Sartorel, A.; Scandola, F. *Inorg. Chem.* **2012**, *51*, 7324.

(151) Car, P.-E.; Guttentag, M.; Baldridge, K. K.; Alberto, R.; Patzke, G. R. *Green. Chem.* **2012**, *14*, 1680.

(152) Tanaka, S.; Annaka, M.; Sakai, K. *Chem. Commun.* **2012**, *48*, 1653.

(153) Song, F.; Ding, Y.; Ma, B.; Wang, C.; Wang, Q.; Du, X.; Fu, S.; Song, J. *Energ. Environ. Sci.* **2013**, *6*, 1170.

(154) Lv, H.; Song, J.; Geletii, Y. V.; Vickers, J. W.; Sumliner, J. M.; Musaev, D. G.; Kögerler, P.; Zhuk, P. F.; Bacsa, J.; Zhu, G.; Hill, C. L. *J. Am. Chem. Soc.* **2014**, *136*, 9268.

(155) Han, X.-B.; Zhang, Z.-M.; Zhang, T.; Li, Y.-G.; Lin, W.; You, W.; Su,

Z.-M.; Wang, E.-B. *J. Am. Chem. Soc.* **2014**, *136*, 5359.

(156) Geletii, Y. V.; Botar, B.; Kögerler, P.; Hillesheim, D. A.; Musaev, D. G.; Hill, C. L. *Angew. Chem. Int. Ed.* **2008**, *47*, 3896.

(157) Sartorel, A.; Carraro, M.; Scorrano, G.; Zorzi, R. D.; Geremia, S.; McDaniel, N. D.; Bernhard, S.; Bonchio, M. *J. Am. Chem. Soc.* **2008**, *130*, 5006.

(158) Yin, Q.; Tan, J. M.; Besson, C.; Geletii, Y. V.; Musaev, D. G.; Kuznetsov, A. E.; Luo, Z.; Hardcastle, K. I.; Hill, C. L. *Science* **2010**, *328*, 342.

(159) Toma, F. M.; Sartorel, A.; Iurlo, M.; Carraro, M.; Parisse, P.; Maccato, C.; Rapino, S.; Gonzalez, B. R.; Amenitsch, H.; Da Ros, T.; Casalis, L.; Goldoni, A.; Marcaccio, M.; Scorrano, G.; Scoles, G.; Paolucci, F.; Prato, M.; Bonchio, M. *Nat Chem* **2010**, *2*, 826.

(160) Guo, S.-X.; Liu, Y.; Lee, C.-Y.; Bond, A. M.; Zhang, J.; Geletii, Y. V.; Hill, C. L. *Energ. Environ. Sci.* **2013**, *6*, 2654.

(161) Wu, J.; Liao, L.; Yan, W.; Xue, Y.; Sun, Y.; Yan, X.; Chen, Y.; Xie, Y. *ChemSusChem* **2012**, *5*, 1207.

(162) Han, J.; Zhang, W.; Zhou, T.; Wang, X.; Xu, R. *RSC Adv.* **2012**, *2*, 8293.

(163) Jicha, D. C.; Busch, D. H. *Inorg Chem* **1962**, *1*, 878.

(164) Suades, J.; Solans, X.; Font-Altaba, M. *Polyhedron* **1984**, *3*, 1227.

(165) Turner, M. A.; Driessen, W. L.; Reedijk, J. *Inorg Chem* **1990**, *29*, 3331.

(166) Arnold, A. P.; Bhula, R.; Chen, X.; Geue, R. J.; Jackson, W. G. *Inorg. Chem.* **1999**, *38*, 1966.

(167) Du, P.; Eisenberg, R. *Energ. Environ. Sci.* **2012**, *5*, 6012.

(168) Kilgore, U. J.; Stewart, M. P.; Helm, M. L.; Dougherty, W. G.; Kassel, W. S.; DuBois, M. R.; DuBois, D. L.; Bullock, R. M. *Inorg Chem* **2011**, *50*, 10908.

(169) Pandey, A. S.; Harris, T. V.; Giles, L. J.; Peters, J. W.; Szilagyi, R. K. *J. Am. Chem. Soc.* **2008**, *130*, 4533.

(170) Rakowski DuBois, M.; DuBois, D. L. *Chem. Soc. Rev.* **2009**, *38*, 62.

(171) Chiang, M.-H.; Liu, Y.-C.; Yang, S.-T.; Lee, G.-H. *Inorg. Chem.* **2009**, *48*, 7604.

(172) Hurst, J. K. *Science* **2010**, *328*, 315.

(173) Barber, J. *Chem. Soc. Rev.* **2009**, *38*, 185.

(174) Youngblood, W. J.; Lee, S.-H. A.; Maeda, K.; Mallouk, T. E. *Acc. Chem. Res.* **2009**, *42*, 1966.

(175) Jiao, F.; Frei, H. *Energ. Environ. Sci.* **2010**, *3*, 1018.

(176) Zhou, T.; Wang, D.; Chun-Kiat Goh, S.; Hong, J.; Han, J.; Mao, J.; Xu, R. *Energ. Environ. Sci.* **2015**, *8*, 526.

(177) Hong, D.; Jung, J.; Park, J.; Yamada, Y.; Suenobu, T.; Lee, Y.-M.; Nam, W.; Fukuzumi, S. *Energ. Environ. Sci.* **2012**, *5*, 7606.

(178) Xu, R.; Zeng, H. C. *Langmuir* **2004**, *20*, 9780.

(179) Xu, R.; Zeng, H. C. *J. Phys. Chem. B.* **2003**, *107*, 12643.

(180) Yuan, C.; Yang, L.; Hou, L.; Li, J.; Sun, Y.; Zhang, X.; Shen, L.; Lu, X.; Xiong, S.; Lou, X. W. *Adv Funct Mater* **2012**, *22*, 2560.

(181) Hu, H.; Guan, B.; Xia, B.; Lou, X. W. *J. Am. Chem. Soc.* **2015**, *137*, 5590.

(182) Harbuzaru, B. V.; Corma, A.; Rey, F.; Atienzar, P.; Jordá, J. L.; García, H.; Ananias, D.; Carlos, L. D.; Rocha, J. *Angew. Chem. Int. Ed.* **2008**, *47*, 1080.

(183) Horcajada, P.; Serre, C.; Maurin, G.; Ramsahye, N. A.; Balas, F.; Vallet-Regí, M.; Sebban, M.; Taulelle, F.; Férey, G. *J. Am. Chem. Soc.* **2008**, *130*, 6774.

(184) Zou, R.-Q.; Sakurai, H.; Xu, Q. *Angew. Chem. Int. Ed.* **2006**, *45*, 2542.

(185) Henschel, A.; Gedrich, K.; Kraehnert, R.; Kaskel, S. *Chem. Commun.* **2008**, 4192.

(186) Pan, Y.; Yuan, B.; Li, Y.; He, D. *Chem. Commun.* **2010**, *46*, 2280.

(187) Chen, Y.-Z.; Zhou, Y.-X.; Wang, H.; Lu, J.; Uchida, T.; Xu, Q.; Yu, S.-H.; Jiang, H.-L. *ACS Catal.* **2015**, *5*, 2062.

(188) Gu, X.; Lu, Z.-H.; Jiang, H.-L.; Akita, T.; Xu, Q. *J. Am. Chem. Soc.* **2011**, *133*, 11822.

(189) Müller, M.; Hermes, S.; Kähler, K.; van den Berg, M. W. E.; Muhler, M.; Fischer, R. A. *Chem. Mater.* **2008**, *20*, 4576.

(190) Balu, A. M.; Lin, C. S. K.; Liu, H.; Li, Y.; Vargas, C.; Luque, R. *Appl.*

*Catal. A: Gen.* **2013**, *455*, 261.

(191) Férey, G.; Mellot-Draznieks, C.; Serre, C.; Millange, F.; Dutour, J.; Surblé, S.; Margiolaki, I. *Science* **2005**, *309*, 2040.

(192) Hong, D.-Y.; Hwang, Y. K.; Serre, C.; Férey, G.; Chang, J.-S. *Adv Funct Mater* **2009**, *19*, 1537.

(193) Stöber, W.; Fink, A.; Bohn, E. *J Colloid Interf Sci* **1968**, *26*, 62.

(194) Riha, S. C.; Klahr, B. M.; Tyo, E. C.; Seifert, S.; Vajda, S.; Pellin, M. J.; Hamann, T. W.; Martinson, A. B. F. *ACS Nano* **2013**, *7*, 2396.

(195) Yang, J.; Walczak, K.; Anzenberg, E.; Toma, F. M.; Yuan, G.; Beeman, J.; Schwartzberg, A.; Lin, Y.; Hettick, M.; Javey, A.; Ager, J. W.; Yano, J.; Frei, H.; Sharp, I. D. *J. Am. Chem. Soc.* **2014**, *136*, 6191.

(196) Lorite, I.; Romero, J. J.; Fernández, J. F. *J Raman Spectrosc* **2012**, *43*, 1443.

(197) Fernandez, J. M.; Barriga, C.; Ulibarri, M.-A.; Labajos, F. M.; Rives, V. *J Mater Chem* **1994**, *4*, 1117.

(198) Creutz, C.; Sutin, N. *Proc. Natl. Acad. Sci.* **1975**, *72*, 2858.

(199) Gerken, J. B.; McAlpin, J. G.; Chen, J. Y. C.; Rigsby, M. L.; Casey, W. H.; Britt, R. D.; Stahl, S. S. *J. Am. Chem. Soc.* **2011**, *133*, 14431.

(200) Hong, S. J.; Lee, S.; Jang, J. S.; Lee, J. S. *Energ. Environ. Sci.* **2011**, *4*, 1781.

(201) Lv, H.; Geletii, Y. V.; Zhao, C.; Vickers, J. W.; Zhu, G.; Luo, Z.; Song, J.; Lian, T.; Musaev, D. G.; Hill, C. L. *Chem Soc Rev* **2012**, *41*, 7572.

(202) Stracke, J. J.; Finke, R. G. *J. Am. Chem. Soc.* **2011**, *133*, 14872.

(203) Natali, M.; Berardi, S.; Sartorel, A.; Bonchio, M.; Campagna, S.; Scandola, F. *Chem. Commun.* **2012**, *48*, 8808.

(204) Schiwon, R.; Klingan, K.; Dau, H.; Limberg, C. *Chem. Commun.* **2014**, *50*, 100.

(205) Maksimchuk, N. V.; Timofeeva, M. N.; Melgunov, M. S.; Shmakov, A. N.; Chesalov, Y. A.; Dybtsev, D. N.; Fedin, V. P.; Kholdeeva, O. A. *J. Catal.* **2008**, *257*, 315.

(206) Ramos-Fernandez, E. V.; Pieters, C.; van der Linden, B.; Juan-Alcañiz, J.; Serra-Crespo, P.; Verhoeven, M. W. G. M.; Niemantsverdriet, H.; Gascon, J.; Kapteijn, F. *J. Catal.* **2012**, *289*, 42.

(207) Maksimchuk, N. V.; Kovalenko, K. A.; Arzumanov, S. S.; Chesalov, Y. A.; Melgunov, M. S.; Stepanov, A. G.; Fedin, V. P.; Kholdeeva, O. A. *Inorg. Chem.* **2010**, *49*, 2920.

(208) Bromberg, L.; Diao, Y.; Wu, H.; Speakman, S. A.; Hatton, T. A. *Chem. Mater.* **2012**, *24*, 1664.

(209) Juan-Alcañiz, J.; Ramos-Fernandez, E. V.; Lafont, U.; Gascon, J.; Kapteijn, F. *J. Catal.* **2010**, *269*, 229.

(210) Hu, X.; Lu, Y.; Dai, F.; Liu, C.; Liu, Y. *Micropor Mesopor Mat* **2013**, *170*, 36.

(211) Zhang, Y.; Degirmenci, V.; Li, C.; Hensen, E. J. M. *ChemSusChem* **2011**, *4*, 59.

(212) Karvonen, L.; Valkeapää, M.; Liu, R.-S.; Chen, J.-M.; Yamauchi, H.; Karppinen, M. *Chem. Mater.* **2010**, *22*, 70.

(213) Dahéron, L.; Martinez, H.; Dedryvère, R.; Baraille, I.; Ménétrier, M.; Denage, C.; Delmas, C.; Gonbeau, D. *J. Phys. Chem. C.* **2009**, *113*, 5843.

(214) Katsoulis, D. E.; Pope, M. T. *J. Am. Chem. Soc.* **1984**, *106*, 2737.

(215) Balula, Maria S.; Gamelas, José A.; Carapuça, Helena M.; Cavaleiro, Ana M. V.; Schlindwein, W. *Eur. J. Inorg. Chem.* **2004**, *2004*, 619.